GLOBAL PLATE MOTION FRAMES: TOWARD A UNIFIED MODEL

Trond H. Torsvik,[1,2,3] R. Dietmar Müller,[4] Rob Van der Voo,[5] Bernhard Steinberger,[1] and Carmen Gaina[1]

Received 7 May 2007; revised 23 November 2007; accepted 12 February 2008; published 12 August 2008.

[1] Plate tectonics constitutes our primary framework for understanding how the Earth works over geological timescales. High-resolution mapping of relative plate motions based on marine geophysical data has followed the discovery of geomagnetic reversals, mid-ocean ridges, transform faults, and seafloor spreading, cementing the plate tectonic paradigm. However, so-called ''absolute plate motions,'' describing how the fragments of the outer shell of the Earth have moved relative to a reference system such as the Earth's mantle, are still poorly understood. Accurate absolute plate motion models are essential surface boundary conditions for mantle convection models as well as for understanding past ocean circulation and climate as continent-ocean distributions change with time. A fundamental problem with deciphering absolute plate motions is that the Earth's rotation axis and the averaged magnetic dipole axis are not necessarily fixed to the mantle reference system. Absolute plate motion models based on volcanic hot spot tracks are largely confined to the last 130 Ma and ideally would require knowledge about the motions within the convecting mantle. In contrast, models based on paleomagnetic data reflect plate motion relative to the magnetic dipole axis for most of Earth's history but cannot provide paleolongitudes because of the axial symmetry of the Earth's magnetic dipole field. We analyze four different reference frames (paleomagnetic, African fixed hot spot, African moving hot spot, and global moving hot spot), discuss their uncertainties, and develop a unifying approach for connecting a hot spot track system and a paleomagnetic absolute plate reference system into a ''hybrid'' model for the time period from the assembly of Pangea (~320 Ma) to the present. For the last 100 Ma we use a moving hot spot reference frame that takes mantle convection into account, and we connect this to a pre–100 Ma global paleomagnetic frame adjusted 5° in longitude to smooth the reference frame transition. Using plate driving force arguments and the mapping of reconstructed large igneous provinces to core–mantle boundary topography, we argue that continental paleolongitudes can be constrained with reasonable confidence.

Citation: Torsvik, T. H., R. D. Müller, R. Van der Voo, B. Steinberger, and C. Gaina (2008), Global plate motion frames: Toward a unified model, *Rev. Geophys.*, *46*, RG3004, doi:10.1029/2007RG000227.

1. INTRODUCTION

[2] Plates form the outer shell of the Earth, and their past movements may be traced using geological data. Plate tectonics is a paradigm that attempts to describe the complex dynamic evolution of the Earth in terms of rigid lithospheric plates. A simplified form of the theory invokes the Earth's heat engine to drive plate motions: mantle material heated by isotopic decay rises at spreading ridges where plates diverge and cool during seafloor spreading. The mantle is cooled by subduction of old, cold lithosphere and is then isotopically heated to rise once again ad infinitum. The theory of plate tectonics has proved successful both theoretically and practically, providing a scientific framework for diverse geological disciplines. It is now an important challenge to integrate plate tectonics into mantle dynamics in order to allow a full dynamic treatment of Earth motion and deformation on all scales. Much progress has been made in understanding the dynamics of mantle convection, plate tectonics, and plumes, but a fully integrated model incorporating both plate motions and mantle dynamics has yet to be realized. Even though links between mantle activity and plate tectonics are becoming more evident, notably through subsurface tomographic images and advancements in mineral physics, there is still no generally accepted mechanism that consistently explains plate tectonics in the framework of mantle convection.

[1]Center for Geodynamics, NGU, Trondheim, Norway.
[2]Also at Physics of Geological Processes, University of Oslo, Oslo, Norway.
[3]Also at School of Geosciences, University of the Witwatersrand, Johannesburg, South Africa.
[4]School of Geosciences, University of Sydney, Sydney, New South Wales, Australia.
[5]Department of Geological Sciences, University of Michigan, Ann Arbor, Michigan, USA.

8755-1209/08/2007RG000227
Paper number 2007RG000227

[3] The development of a unifying geodynamic model requires the establishment of a global plate motion model. However, the relative motion between tectonic plates must first be determined from fracture zones and ocean floor magnetic anomalies, the oldest of which are only Jurassic in age (~175 Ma) (section 2). Only then can plates be restored to their paleopositions on the globe using paleomagnetic data (section 3), "absolute" plate rotations from *hot spot tracks* (if one considers *hot spots* fixed), or, alternatively, using tracks of hot spots that move because of plume advection in the mantle (sections 4 and 5). (Italicized terms are defined in the glossary, after the main text.) However, the hot spot track method cannot be used prior to ~130 Ma, which is the age at the end of the oldest known track in the South Atlantic. That leaves *paleomagnetism*, with its known limitation that it cannot determine motions in longitude, as the only quantitative way of positioning objects on the globe during older times.

[4] Multiple paleomagnetic and hot spot–mantle reference frames have been published and compared over the past decades, but many were constructed without appropriate consideration of results based on different data sets and methods. In this paper we combine interdisciplinary know-how in developing paleomagnetic and hot spot reference frames, and most importantly, we compare reference frames (section 6) that are generated with the same timescales and *plate circuit* closure. Ultimately, we combine hot spot and paleomagnetic frames in order to develop a hybrid global reference frame for plate motions back to the time when *Pangea* assembled (section 7). We illustrate how this hybrid frame can be used to explore links between surface phenomena and deep mantle heterogeneities and briefly discuss the possible causes of kinks, cusps, and longer-duration small circle segments in the global *apparent polar wander* (APW) path for the Pangea supercontinent (section 8).

2. RELATIVE PLATE MOTIONS AND PLATE MOTION CHAINS

[5] The relative motions between tectonic plates can be determined from marine geophysical data by the matching of fracture zones and magnetic anomalies of the same age, corresponding to patterns of paleoridge and paleotransform segments at a given reconstruction time. Usually, the geophysical data quality varies substantially, and identification errors can occur; therefore, the quality of the computed rotations needs to be assessed against the quality of input data. Since *Bullard et al.* [1965] published the first set of computer-generated reconstructions and defined the uncertainties attached to the inferred rotations, several other methods have been proposed to account for uncertainties in plate rotations [*Hellinger*, 1981; *Stock and Molnar*, 1983]. Many of the rotations included in our study were calculated using *Hellinger*'s [1981] criteria for goodness of fit, associated with uncertainties based on the statistical approach developed by *Chang* [1988] (see Table 1 for references to quantitative reconstructions). This method requires that *isochrons* (i.e., magnetic and fracture zone data of the same age) are divided into great circle segments (Figure 1a). Even though fracture zones are expected to follow small circles in plate tectonic theory, *Hellinger* [1981] chose to fit both paleo-mid-ocean ridge and fracture zone segments to great circles because this greatly simplifies the least squares fitting routine. The length of fracture segments used in this approach is so short that the difference between a small circle versus a great circle segment is negligible in this context. The sum of squares of the weighted distances of fixed data points (from one plate) and rotated data points (from the other plate) to the great circle segments is minimized in order to derive the rotation parameters and their uncertainties [*Hellinger*, 1981]. The uncertainty in a rotation is described by a covariance matrix, which depends on plate boundary geometry, the number of data points, and data uncertainties [*Chang et al.*, 1992]. This method allows one to combine independently calculated rotations and their uncertainties and to compute the resulting rotation with an uncertainty region that reflects the errors in the input rotations.

[6] The *Hellinger* [1981] criteria for goodness of fit have been used mainly for deriving best fit rotations from conjugate magnetic anomalies and fracture zone data. For matching boundary between continental and oceanic crust segments a visual fit is usually preferred because the geometry of a *continent-ocean boundary* (COB) can be very sinuous and difficult to break into great circle segments, as required by *Hellinger*'s [1981] methodology. Therefore, predrift rotations mostly do not have uncertainties attached to them. However, plate circuits can be used to derive the amount of prebreakup displacement (and uncertainties). As an example we used the rotations between North America and Greenland and between North America and *Eurasia* to determine the relative motion and its uncertainties between Greenland and Eurasia before *breakup* (Figure 1b). According to our kinematic model the position of the COBs should be found within an area that is 45 to 77 km wide (from south to north); the uncertainty of reconstructed points is given by the *stage pole* uncertainty ellipse calculated for stage pole 31 to 25 (67 to 55 Ma). A rotated Eurasian COB at 55 and 57 Ma (white lines in Figure 1b) fits the end limits of the oldest uncertainty ellipse. Because the ellipse shows the uncertainty of the location of the Eurasian COB at 55.9 Ma, this might indicate that the time of breakup occurred between 55 and 57 Ma.

[7] Most Euler rotations include insignificant *predrift extension* prior to initiation of seafloor spreading; as a result the majority of Pangea reconstructions essentially use Jurassic Euler rotations with minor post-Permian intraplate deformation. The paleomagnetic coverage from two adjacent plates is usually not precise enough to determine this deformation, but in a few rare cases it has been possible to construct predrift relative motion models by fitting portions of APW paths (Figure 2). In this example, late *Paleozoic* APW segments from North America and Europe match each other well in the *Bullard et al.* [1965] reconstruction

TABLE 1. Euler Plate Rotations Used in This Paper

Age (Ma)	Latitude	Longitude	Angle (deg)	Reference[a]
		Europe Versus North America		
0	0	0	0	
10.95	66.44	132.98	−2.57	1 (Q)
20.13	68.91	132.51	−5.09	1 (Q)
33.058	68.22	131.53	−7.65	1 (Q)
47.906	65.38	138.44	−10.96	1 (Q)
53.347	63.07	144.26	−12.82	1 (Q)
55.904	56.17	145.06	−13.24	1 (Q)
68.737	54.45	147.06	−15.86	1 (Q)
79.075	63.4	147.75	−18.48	1 (Q)
83.5	66.54	148.91	−19.7	2
92	66.67	150.26	−20.37	2
105	66.85	152.34	−21.49	2
118	68.99	154.75	−23.05	2
145	68.99	154.75	−23.05	2
200	68.99	154.75	−23.64	3 (Q)
240	88	27	−38	4 (Q)
425	88	27	−38	4 (Q)
		Greenland Versus North America		
0	0	0	0	
33.058	0	0	0	5 (Q)
47.906	62.8	260.9	−2.8	5 (Q)
53.347	40.64	243.07	−3.615	5 (Q)
55.904	20.3	221.8	−3	5 (Q)
68.737	52.86	223.6	−6.28	5 (Q)
83.5	65.3	−122.45	−11	6
92	66.6	−119.48	−12.2	6
105	67.08	−118.96	−12.99	6
118	67.5	−118.48	−13.78	6
245	67.5	−118.48	−13.78	6
		North America Versus Northwest Africa		
0	0	0	0	
9.7	80.89	22.82	2.478	8 (Q)
19	80.89	23.28	5.244	8 (Q)
25.8	79.34	28.56	7.042	8 (Q)
33.1	75.99	5.98	9.767	8 (Q)
38.4	74.54	0.19	11.918	8 (Q)
42.5	74.38	−2.8	13.56	9
46.3	74.23	−5.01	15.106	8 (Q)
49	75.29	−4.26	15.95	9
52.4	77.34	−1.61	16.963	8 (Q)
55.9	80.64	6.57	17.895	8 (Q)
65.6	82.74	2.93	20.84	8 (Q)
71.1	81.35	−8.32	22.753	8 (Q)
73.6	81.11	−10.64	23.74	9
79.1	78.64	−18.16	26.99	9
83.5	76.81	−20.59	29.51	9
89.9	74.33	−22.65	33.86	10
94.1	72	−24.39	36.49	10
100	69.42	−23.52	40.46	10
106.9	68.08	−22.66	45.36	10
118.1	66.21	−21	53.19	10
119.7	66.09	−20.17	54.45	11
125.8	65.97	−19.43	56.63	11
133.1	66.14	−18.72	58.03	11
139.2	66.24	−18.33	59.71	11
148.5	66.24	−18.33	62.14	11
154.2	66.7	−15.85	64.9	11
170	67.02	−13.17	72.1	12
175	66.95	−12.02	75.55	12
215	67	348	79	13
320	67	348	79	13
		Northwest Africa Versus South Africa		
0	0	0	0	
83.5	0	0	0	14
120.4	16.5	6.7	−1.15	14
600	16.5	6.7	−1.15	14

TABLE 1. (continued)

Age (Ma)	Latitude	Longitude	Angle (deg)	Reference[a]
		Northeast Africa Versus South Africa		
0	0	0	0	
83.5	0	0	0	15
120.4	40.5	298.6	−0.7	15
600	40.4	298.6	−0.7	15
		South American Craton (SAC) Versus South Africa		
0	0	0	0	
2.7	62.2	−39.4	0.83	8
9.7	62.05	−40.59	3.18	8
19	58.77	−37.32	7.049	8
25.8	57.59	−36.27	9.962	8
33.1	56.17	−33.64	13.41	8
38.4	57.1	−33	15.912	8
46.3	56.95	−31.15	19.107	8
52.4	58.89	−31.18	21.38	8
55.9	61.35	−32.21	22.273	8
65.6	63.88	−33.61	24.755	8
71.6	63.41	−33.38	26.573	8
79.1	62.92	−34.36	30.992	8
83.5	61.88	−34.26	33.512	8
113	52.4	325	51.3	15
120.4	51.6	−35	52.92	14
126.7	50.4	−33.5	54.42	14
131.7	50	−32.5	55.08	14
320	50	−32.5	55.08	14
		Parana Versus South Africa (as SAC for ≤125.7)		
126.7	50.4	326.5	54.42	15
131.7	47.5	326.7	56	15
150	47.5	326.7	56.2	15
200	47.5	326.7	56.2	15
600	47.6	326.7	56.2	14
		Colorado Versus South Africa (as SAC for ≤125.7)		
126.7	50.4	326.5	54.42	15
131.7	47.5	326.7	57	15
150	47.5	326.7	57.3	15
200	47.5	326.7	58.2	15
600	47.5	326.7	58.2	15
		Madagascar Versus South Africa		
0	0	0	0	
120.4	90	0	0	
124.1	2.57	−63.33	1.5	20
126.7	2.57	−63.33	2.43	20
128.2	2.57	−63.33	3.17	20
130.2	2.57	−63.33	3.94	20
132.1	2.57	−63.33	4.68	20
145.1	−0.6	−61.8	8.9	20[b]
160.0	−14.8	−42.5	15.4	20[b]
600.0	−14.8	−42.5	15.4	20[b]
		India Versus Madagascar		
0	0	0	0	
9.9	23.8	33.1	−4.6	20[b]
20.2	29.6	23.9	−7.5	20[b]
83.5	22.8	19.1	−51.28	20
88	19.8	27.2	−59.16	20
120.4	24.02	32.04	−53.01	20
124	23.14	33.1	−54.51	20
132.1	18.45	31	−61.52	20
600	18.45	31	−61.52	20
		Australia Versus East Antarctica		
0	0	0	0	
2.6	−11.6	−139.7	1.65	25 (Q)
5.9	−11.59	−139.23	3.83	25 (Q)
11.1	−11.90	−142.06	6.79	25 (Q)
20.1	−13.39	−145.63	12.05	25 (Q)
26.0	−13.80	−146.44	15.92	25 (Q)

TABLE 1. (continued)

Age (Ma)	Latitude	Longitude	Angle (deg)	Reference[a]
28.5	−13.58	−146.02	17.32	25 (Q)
31.0	−13.40	−145.62	18.89	25 (Q)
33.5	−13.45	−145.62	20.49	25 (Q)
37.5	−14.65	−146.52	22.88	25 (Q)
53.3	12.65	32.76	−25.24	17
65.6	11.79	32.96	−26.05	17
73.6	11.27	33.08	−26.59	17
83.5	10.67	33.22	−27.22	17
96	8.14	33.34	−27.83	17
120.4	11.1	−137.17	29.65	3
320	11.1	−137.17	29.65	3
		East Antarctica Versus South Africa		
0	0	0	0	
9.9	8.2	−49.4	1.53	16 (Q)
20.2	10.7	−47.9	2.78	16 (Q)
33.2	12	−48.4	5.46	16 (Q)
40.1	13.6	−41.4	7.47	18 (Q)
51.7	8.5	−40.8	10.01	18 (Q)
63.1[c]	11.3	−49.6	11.1	18 (Q)
71.1	−1.2	−42.4	12.38	18 (Q)
75.5	−4	−40.9	14.03	18 (Q)
76.3	−4.6	−40.6	14.39	18 (Q)
83.5	−1.3	−34.7	17.78	18 (Q)
96	3.1	−38.5	26.5	18 (Q)
99	−2.5	−34.03	26.12	19
120.4	10.36	153.67	−41.56	20 (Q)
124.7	9.45	152.5	−42.91	20 (Q)
126.7	9.3	152	−43.71	20 (Q)
132.1	8.9	151.2	−46.29	20 (Q)
134	8.72	151.1	−47.27	20 (Q)
136.7	8.39	150.64	−48.16	20 (Q)
137.9	8.25	150.44	−48.55	20 (Q)
140.4	7.96	150.04	−49.38	20 (Q)
148.1	6.79	146.8	−51.55	20 (Q)
160	10.45	148.76	−58.19	20 (Q)
360	10.45	148.76	−58.19	20 (Q)
		West Antarctica Versus East Antarctica		
0	0	0	0	
26.55	−18.15	−17.85	0	21
33.55	−18.15	−17.85	0.7	22 (Q)
43.8	−18.15	−17.85	1.7	21
52.2	18.2	162.1	−1.7	3
61.1	47.225	146.194	−2.967	3
600	47.225	146.194	−2.967	3
		Lord Howe Rise Versus Australia		
0	0	0	0	
52.2	0	0	0	23 (Q)
53.3[c]	−14.19	130.41	−0.72	23 (Q)
55.8[c]	−15.93	133.47	−2.11	23 (Q)
57.9[c]	−16.93	136.23	−3.79	23 (Q)
61.2	−4.65	131.51	−4.43	23 (Q)
62.5[c]	−4.71	132.68	−5.17	23 (Q)
64[c]	−0.19	130.37	−5.46	23 (Q)
65.6	−3.99	131.8	−6.73	23 (Q)
67.7[c]	−9.04	134.46	−8.83	23 (Q)
71.1[c]	−14.72	139.04	−13.08	23 (Q)
73.6[c]	−9.53	137.2	−12.94	23 (Q)
79	0.37	133.82	−13	23 (Q)
83.5	2.70	−43.60	14.60	23 (Q)
86	4.06	−42.35	15.51	23 (Q)
90	3.27	−42.59	18.34	3
600	3.27	−42.59	18.34	3
		South Campbell Plateau Versus Lord Howe Rise		
46.3	−49.8	178.4	−49	24
83.5	−49.8	178.4	−49	24

TABLE 1. (continued)

Age (Ma)	Latitude	Longitude	Angle (deg)	Reference[a]
		Pacific Versus West Antarctica		
0	0	0	0	
0.78	64.25	−79.06	0.68	7 (Q)
2.58	67.03	−73.72	2.42	7 (Q)
5.89	67.91	−77.93	5.42	7 (Q)
8.86	69.68	−77.06	7.95	7 (Q)
10.9	70.86	−75.96	9.71	7 (Q)
12.29	71.75	−73.77	10.92	7 (Q)
17.47	73.68	−69.85	15.17	7 (Q)
20.1	74.15	−68.7	16.9	7 (Q)
24.06	74.72	−67.28	19.55	7 (Q)
28.28	74.55	−67.38	22.95	7 (Q)
33.54	74.38	−64.74	27.34	7 (Q)
42.54	74.9	−51.31	34.54	7 (Q)
47.91	74.52	−50.19	37.64	7 (Q)
53.35	73.62	−52.5	40.03	7 (Q)
61.1	71.38	−55.57	44.9	7 (Q)
67.7	68.94	−55.52	49.6	26
73.6	66.72	−55.04	53.74	27 (Q)
83.5	65.58	−52.38	63.07	27 (Q)

[a]References are 1, *Gaina et al.* [2002]; 2, *Srivastava and Roest* [1989]; 3, this study; 4, *Bullard et al.* [1965]; 5, C. Gaina et al. (manuscript in preparation, 2008); 6, *Roest and Srivastava* [1989]; 7, *Cande et al.* [1995]; 8, *Müller et al.* [1997]; 9, *Müller et al.* [1993]; 10, *Müller and Roest* [1992]; 11, *Roest et al.* [1992]; 12, *Klitgord and Schouten* [1986]; 13, *Torsvik et al.* [2002]; 14, *Nürnberg and Müller* [1991]; 15, *Torsvik et al.* [2004]; 16, *Royer and Chang* [1991]; 17, *Royer and Rollet* [1997]; 18, *Bernard et al.* [2005]; 19, *Marks and Tikku* [2001]; 20, R. D. Müller and C. Gaina (manuscript in preparation, 2008); 21, S. C. Cande (personal communication, 2002); 22, *Cande et al.* [2000]; 23, *Gaina et al.* [1998]; 24, *Sutherland* [1995]; 25, *Cande and Stock* [2004]; 26, J. M. Stock (unpublished data, 2002); and 27, *Larter et al.* [2002]. Q indicates qualitative reconstruction.
[b]Value is recalculated from other plate rotations and plate circuit closure.
[c]Value is not used in smoothed global moving hot spot frame.

for the interval from 310 to 240 Ma. However, no single fit accommodates the early *Mesozoic* APW segments for North America and Europe. The fit for 240–210 Ma in Figure 2b was obtained with a gradually changing set of reconstructions using interpolated *Euler poles* (Table 1). Employing published Jurassic stage poles [e.g., *Royer et al.*, 1992] for pre-Jurassic times results in APW paths that are markedly divergent (Figure 2a); this must clearly be in error given the fact that *Laurentia* had already collided with *Baltica-Avalonia* in the middle-to-late Silurian [*Torsvik et al.*, 1996] and remained attached to it during Pangea times.

[8] On the basis of the data listed in Table 1 we have calculated Euler rotations relative to a fixed southern Africa; interpolated rotations (5 Ma intervals) are listed in Table 2. As an example we include a reconstruction for 200 Ma that also shows our *plate motion chains* with respect to a fixed southern Africa (Figure 3a). We have also calculated relative velocities of a few selected plates in our analyses. As examples we show in Figure 3b calculated plate velocities between North America and NW Africa (histogram), Europe (squares), and Greenland (circles). Our model (Table 1) includes predrift extension of 1.75 cm/a between Europe and North America during most of the Triassic and the Early Jurassic. The bulk of predrift extension occurs in the Cretaceous (red squares in Figure 3b) followed by an increase in relative velocities (3.5 cm/a) between 50 and 60 Ma, which coincides with the initial opening (rift to drift) of the northeast Atlantic (~55 Ma). Note that North

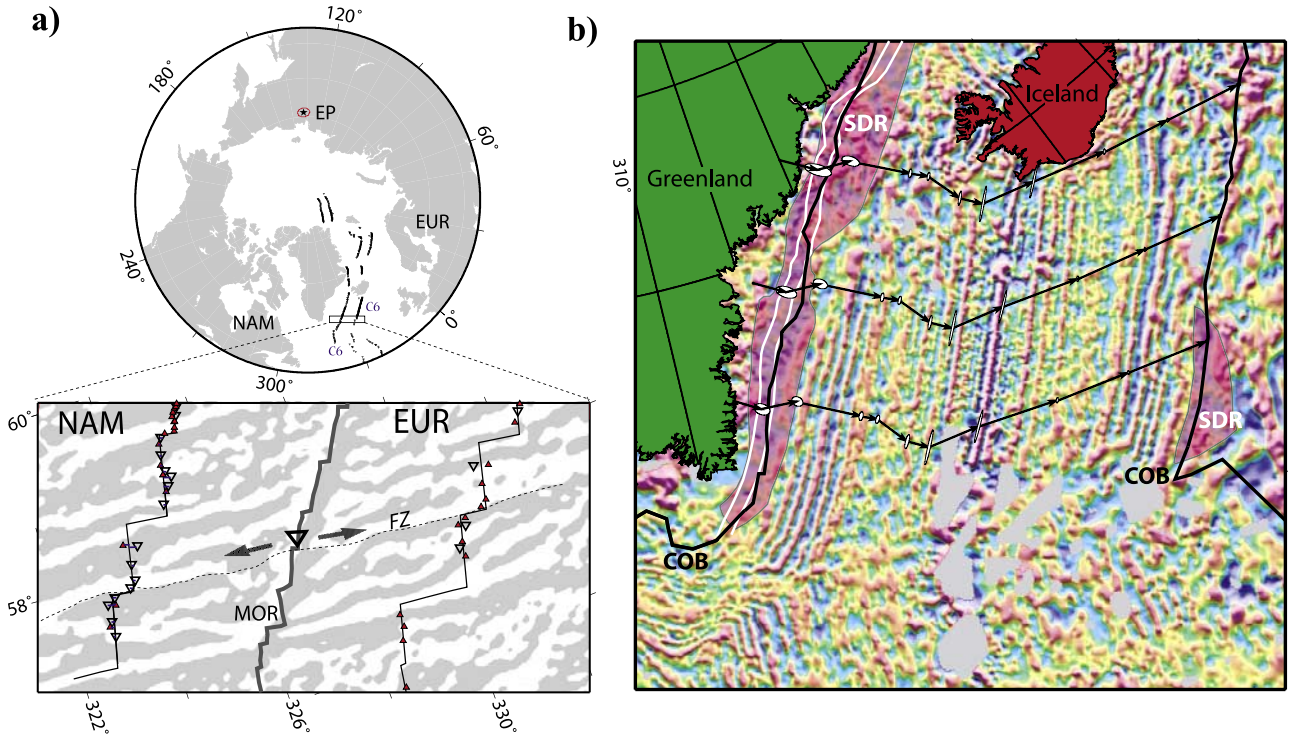

Figure 1. (a) Example of marine magnetic anomaly interpretations (700 data points of chron 6 at 20.1 Ma) and resulting Euler pole (EP) (black star) and uncertainty ellipse (red contour around EP) for relative motion between North America (NAM) and Eurasia (EUR) (note that the ellipse was enlarged 3 times in order to be visible on the map). Detailed image shows a subset of the chron 6 interpretation in the North Atlantic and illustrates *Hellinger*'s [1981] criterion of fit. Fixed data points are represented by inverted triangles; rotated data points are red triangles. The background shows the vertical gradients of free air gravity that allow identification of fracture zones (FZ) and offsets between spreading segments. Great circles were fitted for data points in each individual spreading segment. For a given rotation the measure of fit represents the sum of squares of the weighted distances (blue segments perpendicular to the great circle segment shown as an example on the NAM isochron). The thick, gray line shows the present-day mid-ocean ridge (MOR); the arrows indicate the direction of spreading on NAM and EUR plates. (b) Magnetic anomaly grid of the NE Atlantic [*Verhoef et al.*, 1996] south of Iceland. Vectors and their uncertainties show relative motion between Eurasia and Greenland for stage poles 67.7–55.9, 55.9–53.3, 53.3–49.7, 49.7–47.9, 47.9–43.7, 43.7–40.1, 40.1–33.1, 33.1–20.1, 20.1–10.9, and 10.9–0.0 Ma. The prebreakup motion has been calculated by combining North America–Greenland and North America–Eurasia rotations. The thick black lines are continent-ocean boundaries (COBs); the white lines indicate the reconstructed positions of the Eurasian margin relative to Greenland at 55 and 57 Ma. Note that these white lines outline an area that illustrates the uncertainties in the position of the breakup as suggested by the 95% confidence errors. Light red transparent areas show the mapped seaward dipping reflectors (SDR): Greenland margin, modified after *Hopper et al.* [2003], and Eurasian margin from L. Gernigon (personal communication, 2006).

America–NW Africa predrift extension from 220 to 180 Ma (orange part of the histogram, 0.7 cm/a) was recorded by the formation of complex rift systems (e.g., Newark, Connecticut, and Fundy basins) and was contemporaneous with the Central Atlantic Magmatic Province (~200 Ma) that affected vast areas in North America, NW Africa, SW Europe, and South America.

3. GLOBAL PALEOMAGNETIC FRAME

3.1. Plate of Choice Anchoring the Global Reference Framework

[9] Paleomagnetic reconstructions derived from paleopoles or APW path segments constrain the paleolatitude and the angular orientation of a continent, but its paleolongitude remains unconstrained. However, this degree of freedom can be minimized by selecting an appropriate reference plate; in other words, if one can determine which plate (or continent) has moved longitudinally the least since the time represented by a reconstruction, then that plate should be used as the reference plate [*Burke and Torsvik*, 2004]. Africa was surrounded on nearly all sides by mid-ocean ridges after the breakup of Pangea: hence, the *ridge push forces* should roughly cancel (see also section 9).

3.2. Paleomagnetic Data Selection

[10] Paleomagnetic data were compiled from original sources and graded according to Van der Voo's classifica-

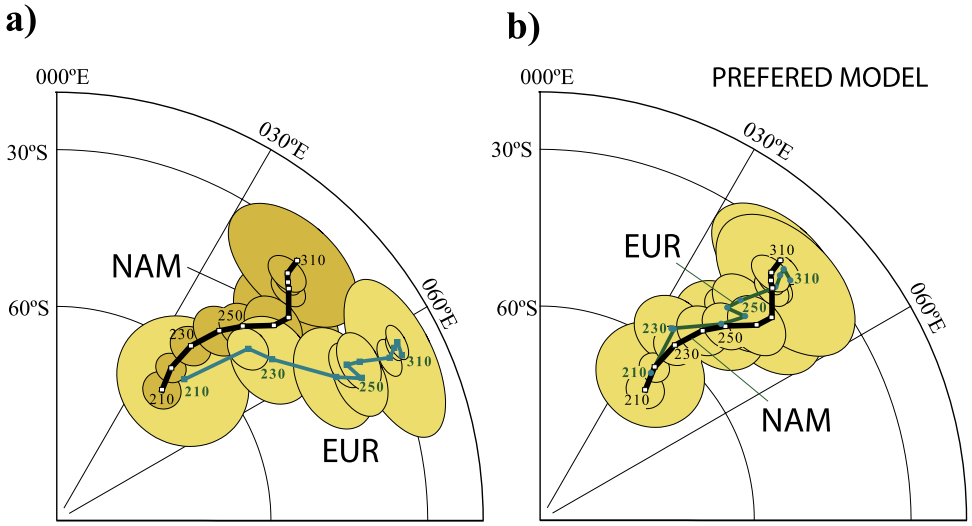

Figure 2. Comparison of NAM and EUR apparent polar wander paths (shown in South African coordinates) using different predrift fits for the North Atlantic. (a) "Traditional" mid-Jurassic Euler pole is used from *Royer et al.* [1992] (this 170 Ma stage pole is located at latitude 69.1°N, longitude 156.7°E, and angle −23.64°). (b) Minimization of the differences between the two paths by using a *Bullard et al.* [1965] fit from 310 to 240 Ma (latitude 88°N, longitude 27°E, and angle −38°) and then a gradual, interpolated change to a new fit at 200 Ma (see Table 1) (latitude 69°N, longitude 155.8°E, and angle −23.6°). A similar approach was devised by *Torsvik et al.* [2001b], but their Euler pole changeover was somewhat different.

tion system [*Van der Voo*, 1988, 1993]. In brief, this classification system includes seven reliability criteria: (1) well-determined age and the assumption that the magnetization age equals the actual rock age, (2) sufficient number of samples and adequate statistics, (3) proper demagnetization techniques and documentation, (4) field tests to constrain the age of the magnetization, (5) structural control and tectonic coherence with the involved craton or block, (6) presence of reversals, and (7) no resemblance to paleopoles of younger age. For example, a quality factor $Q \geq 3$ (7 is best) means that at least three of these quality criteria are satisfied. Some criteria are obviously more important than others when constructing APW paths, and no *paleomagnetic poles* that knowingly fail criterion 1 are included in our analysis.

[11] The data compilation for *Laurussia* (North America, Greenland, and stable Europe) and *Gondwana* follows *Van der Voo* [1993], *Torsvik et al.* [2001b], *Si and Van der Voo* [2001], *Torsvik and Van der Voo* [2002], and *Van der Voo and Torsvik* [2004] with the additional inclusion of a few new data entries and revised ages for certain poles (notably from Europe [*Van der Voo and Torsvik*, 2004]). Only poles with $Q \geq 3$ are included, and several paleopoles have been updated with new isotopic age information whenever available. We did not include late Paleozoic–early Mesozoic paleomagnetic data from *Siberia* because we are as yet uncertain whether Siberia was fully and tightly joined with Laurussia and the rest of Pangea at the dawn of the Mesozoic [*Torsvik and Andersen*, 2002; *Van der Voo and Torsvik*, 2004; *Cocks and Torsvik*, 2007]. Inclusion of Siberian Trap poles (~251 Ma) [*Bowring et al.*, 1998] based on the assumption of coherence between Siberia and the rest of Pangea, however, would not critically affect our global analysis.

[12] Our paleopole compilation is listed in Table 3. Each paleopole was rotated to southern African coordinates (Figure 3a), using the parameters of Tables 1 and 2 while interpolating to the same age as the paleopole. The global compilation, comprising 419 paleomagnetic poles with Late Carboniferous and younger ages, is shown as south poles in Figure 4. The scatter of poles can be considerable; note that the Late Permian–Early Triassic poles from Gondwana generally show more easterly pole longitudes than do poles rotated from Laurentia (Figure 4b). Possible explanations for this are discussed in section 3.4.

3.3. APW Paths

[13] APW paths are expected to average out random noise and to determine basic patterns of APW. The two most common methods for generating such paths are the running mean (moving window) and the spherical spline method. In the running mean method, paleomagnetic poles from a continent are assigned absolute ages, a time window is selected, and then all paleomagnetic poles with ages falling within the time window are averaged (Figure 5a). Using *Fisher* [1953] statistics, 95% confidence ellipses (known as A_{95}) can then be calculated for each mean pole.

[14] A spherical spline on the surface of a sphere can be fitted to paleomagnetic poles [*Jupp and Kent*, 1987] and weighted according to the precision of the paleopole entries. The precision of the path [*Silverman and Waters*, 1984] can be estimated when angular errors are used for weighting.

TABLE 2. Euler Plate Rotations in 5 Ma Intervals All Relative to a Fixed South Africa[a]

	EUR			GRE			NAM			NWAFR			NEAFR			SAC			PAR			COL			MAD			IND			AUS			EANT		
Age (Ma)	Lat	Long	Angle (deg)	Lat	Long	Angle (deg)	Lat	Long	Angle (deg)	Lat	Long	Angle (deg)	Lat	Long	Angle (deg)	Lat	Long	Angle (deg)	Lat	Long	Angle (deg)	Lat	Long	Angle (deg)	Lat	Long	Angle (deg)	Lat	Long	Angle (deg)	Lat	Long	Angle (deg)	Lat	Long	Angle (deg)
5	17.9	−27.1	0.6	80.9	22.8	1.3	80.9	22.8	1.3	90.0	0.0	0.0	90.0	0.0	0.0	62.1	−40.2	1.6	62.1	−40.2	1.6	62.1	−40.2	1.6	90.0	0.0	0.0	22.7	32.9	−2.3	9.7	54.3	−3.3	8.2	−49.4	0.8
10	18.4	−26.3	1.2	80.9	22.9	2.6	80.9	22.9	2.6	90.0	0.0	0.0	90.0	0.0	0.0	61.8	−40.3	3.3	61.8	−40.3	3.3	61.8	−40.3	3.3	90.0	0.0	0.0	23.8	33.1	−4.6	10.4	52.8	−6.2	8.2	−49.4	1.5
15	18.9	−24.6	1.8	80.9	23.2	4.1	80.9	23.2	4.1	90.0	0.0	0.0	90.0	0.0	0.0	59.6	−38.1	5.4	59.6	−38.1	5.4	59.6	−38.1	5.4	90.0	0.0	0.0	27.1	27.4	−6.0	11.5	49.8	−9.0	9.8	−48.4	2.1
20	17.2	−22.7	2.4	80.6	24.4	5.5	80.6	24.4	5.5	90.0	0.0	0.0	90.0	0.0	0.0	58.5	−37.1	7.5	58.5	−37.1	7.5	58.5	−37.1	7.5	90.0	0.0	0.0	29.6	23.9	−7.5	12.4	48.0	−11.8	10.7	−47.9	2.8
25	20.7	−19.0	3.0	79.5	28.1	6.8	79.5	28.1	6.8	90.0	0.0	0.0	90.0	0.0	0.0	57.7	−36.4	9.6	57.7	−36.4	9.6	57.7	−36.4	9.6	90.0	0.0	0.0	25.1	33.2	−10.3	12.9	48.3	−15.0	11.4	−48.2	3.8
30	24.9	−19.5	4.3	77.3	12.5	8.6	77.3	12.5	8.6	90.0	0.0	0.0	90.0	0.0	0.0	56.7	−34.5	11.9	56.7	−34.5	11.9	56.7	−34.5	11.9	90.0	0.0	0.0	22.5	38.5	−13.3	12.8	49.9	−18.1	11.8	−48.3	4.8
35	27.2	−19.3	5.8	74.8	7.2	10.2	75.4	3.5	10.5	90.0	0.0	0.0	90.0	0.0	0.0	56.5	−33.4	14.3	56.5	−33.4	14.3	56.5	−33.4	14.3	90.0	0.0	0.0	22.6	41.3	−15.9	13.5	50.8	−20.9	12.5	−46.1	6.0
40	28.7	−18.5	7.5	72.6	9.5	11.5	74.5	−1.1	12.6	90.0	0.0	0.0	90.0	0.0	0.0	57.1	−32.6	16.6	57.1	−32.6	16.6	57.1	−32.6	16.6	90.0	0.0	0.0	25.5	42.7	−17.4	14.1	52.7	−22.1	13.6	−41.5	7.4
45	30.3	−18.2	9.0	71.4	11.4	12.7	74.3	−4.3	14.6	90.0	0.0	0.0	90.0	0.0	0.0	57.0	−31.4	18.6	57.0	−31.4	18.6	57.0	−31.4	18.6	90.0	0.0	0.0	24.2	40.1	−19.7	14.4	54.7	−22.9	11.1	−41.1	8.5
50	30.8	−16.7	10.0	71.0	20.7	14.2	75.9	−3.5	16.2	90.0	0.0	0.0	90.0	0.0	0.0	58.2	−31.2	20.5	58.2	−31.2	20.5	58.2	−31.2	20.5	90.0	0.0	0.0	24.0	34.2	−23.5	14.7	56.5	−23.6	9.1	−40.9	9.6
55	32.7	−15.4	11.3	71.8	29.6	16.8	79.8	4.1	17.6	90.0	0.0	0.0	90.0	0.0	0.0	60.7	−31.9	22.0	60.7	−31.9	22.0	60.7	−31.9	22.0	90.0	0.0	0.0	22.1	29.2	−28.3	14.0	57.3	−24.7	9.4	−43.5	10.3
60	34.8	−15.7	12.6	71.9	30.5	17.5	81.6	5.1	19.1	90.0	0.0	0.0	90.0	0.0	0.0	62.5	−32.8	23.3	62.5	−32.8	23.3	62.5	−32.8	23.3	90.0	0.0	0.0	19.5	25.2	−34.4	12.9	57.9	−25.7	10.6	−47.4	10.8
65	36.0	−15.8	13.6	71.3	32.9	17.6	82.6	3.2	20.7	90.0	0.0	0.0	90.0	0.0	0.0	63.7	−33.5	24.6	63.7	−33.5	24.6	63.7	−33.5	24.6	90.0	0.0	0.0	19.0	21.9	−40.2	13.6	58.8	−26.3	8.1	−47.7	11.3
70	35.4	−16.1	14.9	69.8	29.0	17.9	81.6	−6.5	22.4	90.0	0.0	0.0	90.0	0.0	0.0	63.5	−33.4	26.1	63.5	−33.4	26.1	63.5	−33.4	26.1	90.0	0.0	0.0	20.5	18.9	−44.4	17.3	60.2	−26.3	0.4	−43.3	12.2
75	35.5	−15.7	15.5	69.0	26.6	18.5	80.4	−13.1	24.6	90.0	0.0	0.0	90.0	0.0	0.0	63.2	−33.9	28.6	63.2	−33.9	28.6	63.2	−33.9	28.6	90.0	0.0	0.0	21.8	18.2	−47.3	19.8	63.3	−26.7	3.7	138.9	−13.8
80	36.1	−15.2	16.9	67.6	21.0	19.8	78.2	−18.8	27.5	90.0	0.0	0.0	90.0	0.0	0.0	62.7	−34.3	31.5	62.7	−34.3	31.5	62.7	−34.3	31.5	90.0	0.0	0.0	22.3	18.2	−49.1	20.5	68.5	−26.6	2.7	142.7	−16.1
85	37.0	−14.2	18.8	66.3	16.4	21.5	76.2	−21.3	30.5	19.6	6.7	0.0	27.9	−61.4	0.0	61.2	−34.3	34.4	61.2	−34.3	34.4	61.2	−34.3	34.4	90.0	0.0	0.0	21.8	22.1	−53.8	19.8	74.6	−26.9	0.6	144.7	−18.8
90	39.6	−13.7	21.9	65.9	11.5	24.2	74.6	−23.0	33.8	16.6	6.7	−0.2	39.8	−61.4	−0.1	59.1	−34.5	37.3	59.1	−34.5	37.3	59.1	−34.5	37.3	90.0	0.0	0.0	20.0	27.5	−58.8	17.7	80.9	−28.9	1.4	−37.0	22.3
95	39.8	−13.7	25.2	64.2	5.5	26.9	72.0	−24.7	36.9	16.5	6.7	−0.4	40.8	−61.4	−0.2	57.2	−34.7	40.3	57.2	−34.7	40.3	57.2	−34.7	40.3	90.0	0.0	0.0	20.7	28.1	−57.8	15.9	86.2	−31.1	2.9	−38.3	25.8
100	40.2	−12.5	28.5	62.7	2.8	30.1	70.0	−24.0	40.2	16.5	6.7	−0.5	40.3	−61.4	−0.3	55.7	−34.8	43.3	55.7	−34.8	43.3	55.7	−34.8	43.3	90.0	0.0	0.0	21.3	28.8	−56.8	18.4	89.3	−30.7	3.1	146.5	−26.8
105	41.6	−11.2	31.7	62.4	1.6	33.3	69.1	−23.3	43.6	16.5	6.7	−0.7	40.6	−61.4	−0.4	54.3	−34.9	46.4	54.3	−34.9	46.4	54.3	−34.9	46.4	90.0	0.0	0.0	21.9	29.6	−55.9	17.9	95.6	−32.6	5.5	148.9	−30.3
110	42.6	−9.8	34.5	62.1	0.9	36.5	68.3	−22.6	47.0	16.5	6.7	−0.8	40.6	−61.4	−0.5	53.1	−35.0	49.5	53.1	−35.0	49.5	53.1	−35.0	49.5	90.0	0.0	0.0	22.6	30.3	−54.9	17.3	101.0	−34.8	7.4	150.7	−33.9
115	43.4	−8.5	37.3	61.8	0.5	39.7	67.6	−21.8	50.4	16.5	6.7	−1.0	40.5	−61.4	−0.6	52.2	−35.0	51.7	52.2	−35.0	51.7	52.2	−35.0	51.7	90.0	0.0	0.0	23.3	31.1	−54.0	16.8	105.6	−37.4	9.0	152.3	−37.6
120	44.5	−6.9	40.3	61.8	0.8	43.1	67.1	−20.4	53.9	16.5	6.7	−1.1	40.5	−61.4	−0.7	51.6	−35.0	52.8	51.6	−35.0	52.8	51.6	−35.0	52.8	90.0	0.0	0.0	24.0	32.0	−53.1	16.4	109.4	−40.3	10.3	153.6	−41.3
125	45.3	−6.3	42.0	61.9	1.0	44.9	67.0	−19.7	55.6	16.5	6.7	−1.2	40.5	−61.4	−0.7	50.7	−33.9	54.0	50.7	−33.9	54.0	50.7	−33.9	54.0	2.6	−63.3	1.8	23.4	34.8	−55.2	15.7	110.3	−42.3	9.4	152.4	−43.0
130	45.9	−5.7	43.0	62.2	1.3	46.0	67.0	−19.1	56.7	16.5	6.7	−1.2	40.5	−61.4	−0.7	50.1	−32.8	54.9	48.5	−33.4	55.4	48.5	−33.4	55.4	2.6	−63.3	3.9	21.2	36.2	−60.1	15.9	111.6	−44.4	9.1	151.5	−45.3
135	46.6	−5.3	44.0	62.4	1.6	47.1	67.1	−18.7	57.9	16.5	6.7	−1.2	40.5	−61.4	−0.7	50.0	−32.5	55.1	47.5	−33.3	56.0	47.5	−33.3	56.0	1.5	−57.6	5.7	21.2	36.2	−61.6	15.9	113.1	−46.6	8.6	150.9	−47.6
140	47.3	−4.9	45.2	62.7	1.6	48.4	67.2	−18.4	59.2	16.5	6.7	−1.2	40.5	−61.4	−0.7	50.0	−32.5	55.1	47.5	−33.3	56.1	47.5	−33.3	56.1	1.0	−55.9	7.2	21.9	37.5	−61.5	15.6	113.7	−48.3	8.0	150.1	−49.2
145	47.8	−4.8	46.4	62.9	1.3	49.7	67.1	−18.3	60.5	16.5	6.7	−1.2	40.5	−61.4	−0.7	50.0	−32.5	55.1	47.5	−33.3	56.1	47.5	−33.3	56.1	0.6	118.3	−8.9	22.6	39.0	−62.5	15.0	113.1	−50.5	7.3	148.1	−50.7
150	48.6	−4.0	47.9	63.2	1.8	51.4	67.3	−17.6	62.2	16.5	6.7	−1.2	40.5	−61.4	−0.7	50.0	−32.5	55.1	47.5	−33.3	56.2	47.5	−33.3	56.2	4.5	119.8	−10.9	24.1	40.4	−62.9	15.5	113.5	−52.5	7.4	147.1	−52.6
155	49.8	−2.2	50.0	63.7	3.6	53.8	67.6	−15.5	64.6	16.5	6.7	−1.2	40.5	−61.4	−0.7	50.0	−32.5	55.1	47.5	−33.3	56.2	47.5	−33.3	56.2	10.6	130.1	−13.0	26.9	41.2	−61.6	17.6	115.7	−54.3	9.0	148.0	−55.4
160	50.6	−1.2	52.1	64.1	4.2	56.0	67.6	−14.5	66.8	16.5	6.7	−1.2	40.5	−61.4	−0.7	50.0	−32.5	55.1	47.5	−33.3	56.2	47.5	−33.3	56.2	14.8	137.5	−15.4	29.8	42.1	−60.5	19.5	117.8	−56.2	10.5	148.8	−58.2
165	51.4	−0.3	54.2	64.4	4.8	58.3	67.7	−13.6	69.1	16.5	6.7	−1.2	40.5	−61.4	−0.7	50.0	−32.5	55.1	47.5	−33.3	56.2	47.5	−33.3	56.2	14.8	137.5	−15.4	29.8	42.1	−60.5	19.5	117.8	−56.2	10.5	148.8	−58.2
170	52.1	0.6	56.3	64.7	5.3	60.6	67.8	−12.8	71.4	16.5	6.7	−1.2	40.5	−61.4	−0.7	50.0	−32.5	55.1	47.5	−33.3	56.2	47.5	−33.3	56.2	14.8	137.5	−15.4	29.8	42.1	−60.5	19.5	117.8	−56.2	10.5	148.8	−58.2
175	52.9	1.9	59.6	64.8	6.0	64.1	67.7	−11.5	74.8	16.5	6.7	−1.2	40.5	−61.4	−0.7	50.0	−32.5	55.1	47.5	−33.3	56.2	47.5	−33.3	56.2	14.8	137.5	−15.4	29.8	42.1	−60.5	19.5	117.8	−56.2	10.5	148.8	−58.2
180	53.0	2.0	60.0	64.9	6.0	64.5	67.7	−11.5	75.3	16.5	6.7	−1.2	40.5	−61.4	−0.7	50.0	−32.5	55.1	47.5	−33.3	56.2	47.5	−33.3	56.2	14.8	137.5	−15.4	29.8	42.1	−60.5	19.5	117.8	−56.2	10.5	148.8	−58.2
185	53.0	2.0	60.4	64.9	5.9	64.9	67.7	−11.5	75.7	16.5	6.7	−1.2	40.5	−61.4	−0.7	50.0	−32.5	55.1	47.5	−33.3	56.2	47.5	−33.3	56.2	14.8	137.5	−15.4	29.8	42.1	−60.5	19.5	117.8	−56.2	10.5	148.8	−58.2
190	53.1	2.1	60.8	65.0	5.9	65.4	67.7	−11.5	76.1	16.5	6.7	−1.2	40.5	−61.4	−0.7	50.0	−32.5	55.1	47.5	−33.3	56.2	47.5	−33.3	56.2	14.8	137.5	−15.4	29.8	42.1	−60.5	19.5	117.8	−56.2	10.5	148.8	−58.2
195	53.2	2.2	61.1	65.0	5.8	65.8	67.7	−11.5	76.6	16.5	6.7	−1.2	40.5	−61.4	−0.7	50.0	−32.5	55.1	47.5	−33.3	56.2	47.5	−33.3	56.2	14.8	137.5	−15.4	29.8	42.1	−60.5	19.5	117.8	−56.2	10.5	148.8	−58.2
200	53.3	2.2	61.5	65.1	5.8	66.2	67.7	−11.5	77.0	16.5	6.7	−1.2	40.5	−61.4	−0.7	50.0	−32.5	55.1	47.5	−33.3	56.2	47.5	−33.3	56.2	14.8	137.5	−15.4	29.8	42.1	−60.5	19.5	117.8	−56.2	10.5	148.8	−58.2
205	53.2	2.6	59.7	65.1	5.7	66.7	67.7	−11.5	77.4	16.5	6.7	−1.2	40.5	−61.4	−0.7	50.0	−32.5	55.1	47.5	−33.3	56.2	47.5	−33.3	56.2	14.8	137.5	−15.4	29.8	42.1	−60.5	19.5	117.8	−56.2	10.5	148.8	−58.2
210	53.1	2.9	57.8	65.2	5.7	67.1	67.7	−11.5	77.9	16.5	6.7	−1.2	40.5	−61.4	−0.7	50.0	−32.5	55.1	47.5	−33.3	56.2	47.5	−33.3	56.2	14.8	137.5	−15.4	29.8	42.1	−60.5	19.5	117.8	−56.2	10.5	148.8	−58.2
215	53.1	3.3	55.9	65.2	5.6	67.5	67.7	−11.5	78.3	16.5	6.7	−1.2	40.5	−61.4	−0.7	50.0	−32.5	55.1	47.5	−33.3	56.2	47.5	−33.3	56.2	14.8	137.5	−15.4	29.8	42.1	−60.5	19.5	117.8	−56.2	10.5	148.8	−58.2
220	52.9	3.6	53.6	65.2	5.6	67.5	67.7	−11.5	78.3	16.5	6.7	−1.2	40.5	−61.4	−0.7	50.0	−32.5	55.1	47.5	−33.3	56.2	47.5	−33.3	56.2	14.8	137.5	−15.4	29.8	42.1	−60.5	19.5	117.8	−56.2	10.5	148.8	−58.2
225	52.7	4.0	51.4	65.2	5.6	67.5	67.7	−11.5	78.3	16.5	6.7	−1.2	40.5	−61.4	−0.7	50.0	−32.5	55.1	47.5	−33.3	56.2	47.5	−33.3	56.2	14.8	137.5	−15.4	29.8	42.1	−60.5	19.5	117.8	−56.2	10.5	148.8	−58.2
230	52.4	4.4	49.1	65.2	5.6	67.5	67.7	−11.5	78.3	16.5	6.7	−1.2	40.5	−61.4	−0.7	50.0	−32.5	55.1	47.5	−33.3	56.2	47.5	−33.3	56.2	14.8	137.5	−15.4	29.8	42.1	−60.5	19.5	117.8	−56.2	10.5	148.8	−58.2
235	52.2	4.8	46.8	65.2	5.6	67.5	67.7	−11.5	78.3	16.5	6.7	−1.2	40.5	−61.4	−0.7	50.0	−32.5	55.1	47.5	−33.3	56.2	47.5	−33.3	56.2	14.8	137.5	−15.4	29.8	42.1	−60.5	19.5	117.8	−56.2	10.5	148.8	−58.2

TABLE 2. (continued)

Age (Ma)	EUR			GRE			NAM			NWAFR			NEAFR			SAC			PAR			COL			MAD			IND			AUS			EANT		
	Lat	Long	Angle (deg)	Lat	Long	Angle (deg)	Lat	Long	Angle (deg)	Lat	Long	Angle (deg)	Lat	Long	Angle (deg)	Lat	Long	Angle (deg)	Lat	Long	Angle (deg)	Lat	Long	Angle (deg)	Lat	Long	Angle (deg)	Lat	Long	Angle (deg)	Lat	Long	Angle (deg)	Lat	Long	Angle (deg)
240	51.9	5.3	44.5	65.2	5.6	67.5	67.7	−11.5	78.3	16.5	6.7	−1.2	40.5	−61.4	−0.7	50.0	−32.5	55.1	47.5	−33.3	56.2	47.5	−33.3	56.2	14.8	137.5	−15.4	29.8	42.1	−60.5	19.5	117.8	−56.2	10.5	148.8	−58.2
245	51.9	5.3	44.5	65.2	5.6	67.5	67.7	−11.5	78.3	16.5	6.7	−1.2	40.4	−61.4	−0.7	50.0	−32.5	55.1	47.5	−33.3	56.2	47.5	−33.3	56.2	14.8	137.5	−15.4	29.8	42.1	−60.5	19.5	117.8	−56.2	10.5	148.8	−58.2
250	51.9	5.3	44.5	65.2	5.6	67.5	67.7	−11.5	78.3	16.5	6.7	−1.2	40.4	−61.4	−0.7	50.0	−32.5	55.1	47.5	−33.3	56.2	47.5	−33.3	56.2	14.8	137.5	−15.4	29.8	42.1	−60.5	19.5	117.8	−56.2	10.5	148.8	−58.2
255	51.9	5.3	44.5	65.2	5.6	67.5	67.7	−11.5	78.3	16.5	6.7	−1.2	40.4	−61.4	−0.7	50.0	−32.5	55.1	47.5	−33.3	56.2	47.5	−33.3	56.2	14.8	137.5	−15.4	29.8	42.1	−60.5	19.5	117.8	−56.2	10.5	148.8	−58.2
260	51.9	5.3	44.5	65.2	5.6	67.5	67.7	−11.5	78.3	16.5	6.7	−1.2	40.4	−61.4	−0.7	50.0	−32.5	55.1	47.5	−33.3	56.2	47.5	−33.3	56.2	14.8	137.5	−15.4	29.8	42.1	−60.5	19.5	117.8	−56.2	10.5	148.8	−58.2
265	51.9	5.3	44.5	65.2	5.6	67.5	67.7	−11.5	78.3	16.5	6.7	−1.2	40.4	−61.4	−0.7	50.0	−32.5	55.1	47.5	−33.3	56.2	47.5	−33.3	56.2	14.8	137.5	−15.4	29.8	42.1	−60.5	19.5	117.8	−56.2	10.5	148.8	−58.2
270	51.9	5.3	44.5	65.2	5.6	67.5	67.7	−11.5	78.3	16.5	6.7	−1.2	40.4	−61.4	−0.7	50.0	−32.5	55.1	47.5	−33.3	56.2	47.5	−33.3	56.2	14.8	137.5	−15.4	29.8	42.1	−60.5	19.5	117.8	−56.2	10.5	148.8	−58.2
275	51.9	5.3	44.5	65.2	5.6	67.5	67.7	−11.5	78.3	16.5	6.7	−1.2	40.4	−61.4	−0.7	50.0	−32.5	55.1	47.5	−33.3	56.2	47.5	−33.3	56.2	14.8	137.5	−15.4	29.8	42.1	−60.5	19.5	117.8	−56.2	10.5	148.8	−58.2
280	51.9	5.3	44.5	65.2	5.6	67.5	67.7	−11.5	78.3	16.5	6.7	−1.2	40.4	−61.4	−0.7	50.0	−32.5	55.1	47.5	−33.3	56.2	47.5	−33.3	56.2	14.8	137.5	−15.4	29.8	42.1	−60.5	19.5	117.8	−56.2	10.4	148.8	−58.2
285	51.9	5.3	44.5	65.2	5.6	67.5	67.7	−11.5	78.3	16.5	6.7	−1.2	40.4	−61.4	−0.7	50.0	−32.5	55.1	47.5	−33.3	56.2	47.5	−33.3	56.2	14.8	137.5	−15.4	29.8	42.1	−60.5	19.5	117.8	−56.2	10.5	148.8	−58.2
290	51.9	5.3	44.5	65.2	5.6	67.5	67.7	−11.5	78.3	16.5	6.7	−1.2	40.4	−61.4	−0.7	50.0	−32.5	55.1	47.5	−33.3	56.2	47.5	−33.3	56.2	14.8	137.5	−15.4	29.8	42.1	−60.5	19.5	117.8	−56.2	10.5	148.8	−58.2
295	51.9	5.3	44.5	65.2	5.6	67.5	67.7	−11.5	78.3	16.5	6.7	−1.2	40.4	−61.4	−0.7	50.0	−32.5	55.1	47.5	−33.3	56.2	47.5	−33.3	56.2	14.8	137.5	−15.4	29.8	42.1	−60.5	19.5	117.8	−56.2	10.5	148.8	−58.2
300	51.9	5.3	44.5	65.2	5.6	67.5	67.7	−11.5	78.3	16.5	6.7	−1.2	40.4	−61.4	−0.7	50.0	−32.5	55.1	47.5	−33.3	56.2	47.5	−33.3	56.2	14.8	137.5	−15.4	29.8	42.1	−60.5	19.5	117.8	−56.2	10.5	148.8	−58.2
305	51.9	5.3	44.5	65.2	5.6	67.5	67.7	−11.5	78.3	16.5	6.7	−1.2	40.4	−61.4	−0.7	50.0	−32.5	55.1	47.5	−33.3	56.2	47.5	−33.3	56.2	14.8	137.5	−15.4	29.8	42.1	−60.5	19.5	117.8	−56.2	10.4	148.8	−58.2
310	51.9	5.3	44.5	65.2	5.6	67.5	67.7	−11.5	78.3	16.5	6.7	−1.2	40.4	−61.4	−0.7	50.0	−32.5	55.1	47.5	−33.3	56.2	47.5	−33.3	56.2	14.8	137.5	−15.4	29.8	42.1	−60.5	19.5	117.8	−56.2	10.5	148.8	−58.2
315	51.9	5.3	44.5	65.2	5.6	67.5	67.7	−11.5	78.3	16.5	6.7	−1.2	40.4	−61.4	−0.7	50.0	−32.5	55.1	47.5	−33.3	56.2	47.5	−33.3	56.2	14.8	137.5	−15.4	29.8	42.1	−60.5	19.5	117.8	−56.2	10.5	148.8	−58.2
320	51.9	5.3	44.5	65.2	5.6	67.5	67.7	−11.5	78.3	16.5	6.7	−1.2	40.4	−61.4	−0.7	50.0	−32.5	55.1	47.5	−33.3	56.2	47.5	−33.3	56.2	14.8	137.5	−15.4	29.8	42.1	−60.5	19.5	117.8	−56.2	10.5	148.8	−58.2

[a]Only plates for which we use paleomagnetic data to generate the global APW path are listed. Abbreviations are as in Figure 3; Lat, latitude; Long, longitude.

However, the real uncertainty surrounding individual paleopole positions is a combination of angular errors, age uncertainties (set at zero for this paper), and uncertainties surrounding the geomagnetic field recording of complexities such as the averaging of secular variation. *Torsvik et al.* [1996], for example, developed a routine to give weight to the data according to their *Q factor* (section 3.2) so that the APW path is firmly anchored to the most reliable data.

[15] Our global APW path (in southern African coordinates, Figure 5a and Table 4) extends back to 320 Ma when the Pangea supercontinent was initially being assembled. A global APW path was first constructed using the running mean method since this is the simplest method and can easily be reproduced by others. We used a window length of 20 Ma and employed 10 Ma increments, causing only moderate smoothing. Increased window length leads to a higher degree of smoothing.

[16] We compare our path of Figure 5a to the APW paths of *Besse and Courtillot* [2002] and *Schettino and Scotese* [2005] and calculate the great circle distance (shortest distance on a sphere) between mean poles of the same age (Figure 5b). The mean great circle distance for the entire 200 Ma interval is 3.9° ± 3.3° with respect to *Besse and Courtillot* [2002], with a peak of 11.1° at 200 Ma (Figure 5b). The mean great circle distance is 4.2° ± 3.3° for our comparison with *Schettino and Scotese* [2005], with a peak of 12.8° at 150 Ma. Most of the differences are likely to be statistically insignificant, but the open loop between 110 and 170 Ma observed in our running mean APW path (Figure 5a) appears as a hairpin with a sharp cusp in the other two paths (Figures 5c and 5d). The reasons for this can be found in a combination of different data selection, degree of smoothing, and different Euler rotation parameters.

[17] With global data sets that have considerable spread and ''unclear'' age progressions, spherical splines (e.g., weighted purely by angular errors) produce sinuous APW paths unless they are severely smoothed. Conversely, a spherical spline weighted by the *Q* factor [*Torsvik et al.*, 1996] will produce APW paths that are anchored to the most reliable data, and this procedure ''reproduces'' the Late Jurassic–Early Cretaceous loop using moderate-to-high smoothing parameters (red line in Figure 5a). However, a shortcoming of this procedure is that the assignment of weights to *Q* factors does not produce output angular uncertainties along the path that have a physical meaning. We therefore opted to first calculate a running mean path (10 Ma window, with increments of 10 Ma, so that there is no window overlap in order to avoid presmoothing) and found that this leads to a better age progression. Only then we applied the spherical spline algorithm to this running mean path weighted by the mean angular errors (A_{95}). This results in angular output uncertainties that have physical meaning. The outcome of this procedure is shown in Figure 5c as the red path with yellow cones of confidence every 10 Ma. Using a moderate-to-high smoothing parameter, we generated a path similar to that of *Schettino and Scotese* [2005]. However, smoothing can lead to removal of real, short-duration features in the path. In order to explore

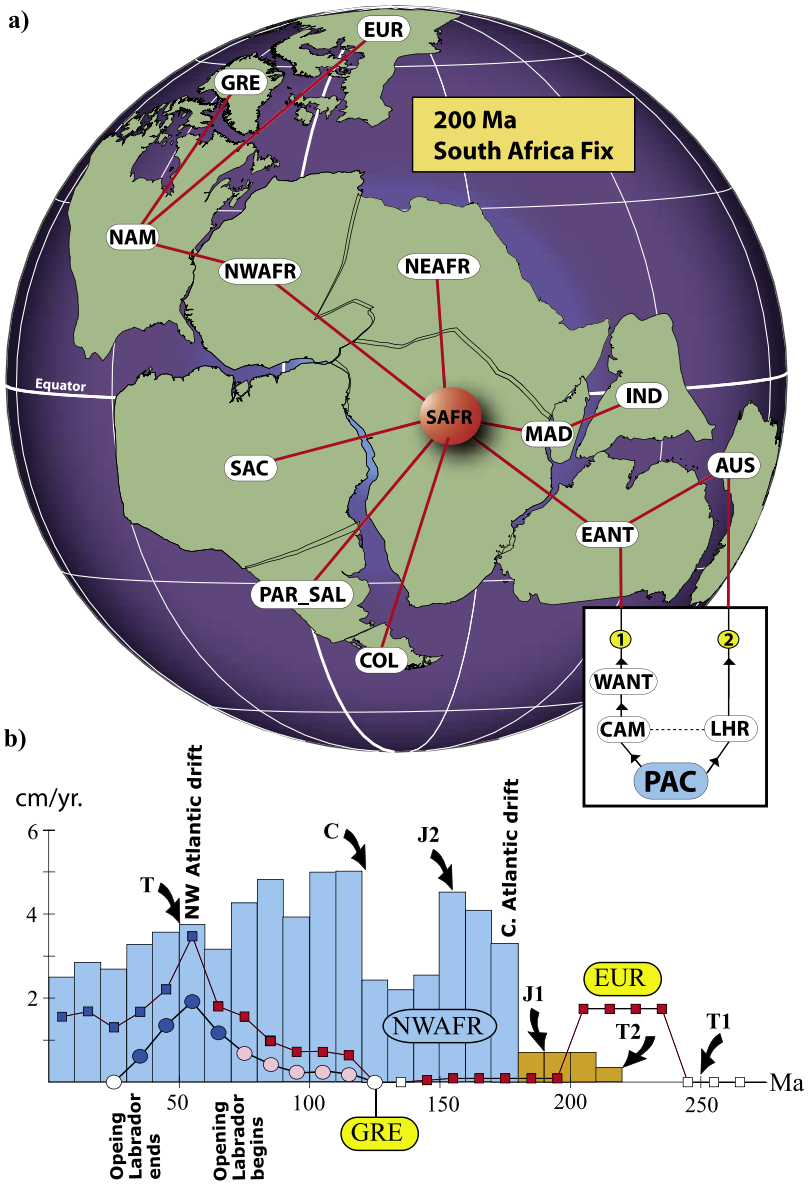

Figure 3. (a) Preferred relative reconstruction at 200 Ma (with southern Africa held fixed) showing the (continental) plates for which paleomagnetic data have been compiled (Table 3). The determinations of relative plate motions (section 2) incorporate a wide variety of data, with the southern African continental element serving as the reference continent relative to which the motion of all other plates are determined. In this paper, motion of the African plate is determined in global reference frames using paleomagnetic (section 3), fixed hot spot (section 4), and moving hot spot (section 5) reference frames. Plate chains linking the Pacific (PAC) and southern Africa (SAFR) follow two different models discussed in the text and illustrated in the inset. Abbreviations are EUR, stable Europe; GRE, Greenland (only Cretaceous-Tertiary poles have been included in the analysis); NAM, North America; NWAFR, northwest Africa; NEAFR, northeast Africa; SAC, main South American craton; PAR_SAL, Parana-Salado subplate; COL, Colorado subplate; IND, India; MAD, Madagascar; EANT, East Antarctica; AUS, Australia; LHR, Lord Howe Rise; WANT, West Antarctica; and CAM, southern Campbell Plateau. The intraplate deformation zones in South America and Africa are taken from *Torsvik et al.* [2004]. (b) Relative plate velocities of North America versus NWAFR (in histogram style), EUR (squares), and GRE (circles). These velocities are mean plate velocities calculated for elements in a 10° × 10° grid. The blue histogram and symbols are derived from seafloor spreading models. Black annotated arrows indicate major kinks or cusps in the global apparent polar wander path when viewed in North American coordinates (see Figure 8).

TABLE 3. Selected Paleomagnetic Poles

Q[a]	α_{95}[b]	Formation and Country	P_{lat}[c]	P_{lon}[c]	Age (Ma)	GPDB[d]
		North America				
6	4.9	Katherine Creek sediments	−78	304	1.5	3060
6	7	Banks Island deposits	−86	120	1.5	3206
3	9.7	Tschicoma Formation	−76	174	5.5	1275, SV
3	12.9	Hepburn's Mesa Formation	−81	225	15.5	2288, SV
4	6.7	Younger plutons	−87	189	22.5	1402, SV
3	8.4	Lake City caldera	−76	30	23	1300, SV
4	5.2	Latir volcanics	−81	331	23.5	1299, SV
4	6.8	Conejos and Hinsdale Formation	−80	343	26	3130, SV
4	5.4	Latir extrusives, sediments	−80	315	27	1299, SV
4	4.4	Mongollon-Datil volcanics	−82	323	30	1315, SV
3	5	Mongollon-Datil volcanics	−83	316	30	2631, SV
4	4.3	Mariscal Mountain gabbro	−80	5	37	2943, SV
3	2.4	Mistastin Lake impact	−86	298	40	562, T
5	7.7	East Fork Washakia Basin	−84	324	44	1632, T
4	10.1	Virginia intrusions	−86	64	44.5	1865
5	8	Absaroka flows	−83	334	46	1117, T
4	**9.6**	Rattlesnake Hills volcanics	−79	326	46	1712, T
6	5.6	Bitterroot Dome dike swarm	−72	342	47	2560, T
4	10.1	Monterey intrusives	−86	64	47	1865, T
6	4.9	Wasatch and Green River Formation	−78	308	51	3150, T
5	4	Robinson Anticline intrusives	−77	326	51	1348, T
6	2.6	Combined Eocene intrusives	−82	350	51	1270, T
5	14	Rhyolite intrusion and contact	−68	9	57	504, T
6	3	Nacimiento Formation	−76	328	61	1033, T
6	3.7	Combined Paleocene intrusives	−82	1	63	1270, T
4	1.1	Gringo Gulch volcanics	−77	21	63	1710, T
4	6.6	Edmonton Group, Alberta	−72	3	63	1914, T
5	3.9	Alkalic intrusives	−81	5.1	64	1711, T
5	5.8	Tombstone[e]	−70	37	71	2806, T
5	6.2	Roskruge volcanics[e]	−70	357	72	1240, T
6	4.6	Adel Mountain volcanics	−83	21	76	2370, T
6	6.2	Maudlow Formation welded tuffs	−70	28	80	2397, T
7	6.6	Elkhorn Mountains	−80	10	81	2382, T
5	4.4	Magnet Cove and other intrusives	−74	13	100	1322, T
5	8.3	Cuttingsville	−72	17	100	3087, T
5	4	Randall Mountain	−77	320	103	3087, T
5	4.4	Little Rattlesnake Complex	−72	3	111	3087, T
5	6.5	Pleasant Mountain	−77	5	112	3087, T
5	5.6	Burnt Meadow Mountains	−76	29	113	3087, T
5	3.6	Alfred Complex	−74	30	120	3036, T
5	5.3	Cape Neddick	−75	355	121	3036, T
6	2.4	Monteregian Hills intrusives	−72	11	122	1853, T
5	6.9	White Mountains igneous complex	−71	8	122	2644, T
5	4.6	Tatnic Complex	−66	28	122	3036, T
5	7.5	Lebanon diorite	−70	15	125	3036, T
5	3.6	Notre Dame Bay dikes	−67	32	128	1854, T
7	2.6	Kimberlite dikes	−58	23	144	2717, T
5	3.6	Upper Morrison Formation[e]	−64	346	147	787, T
6	4.1	Morrison Formation, Brushy Basin Member[e]	−64	341	148	2870, T
5	5.3	Lower Morrison Formation[e]	−57	328	149	787, T
6	7	Canelo Hills volcanics[e]	−59	319	151	1256, T
6	7.4	Summerville Formation[e]	−52	318	159	2419, T
5	4.3	Summerville Sandstone[e]	−64	301	159	1121, T
5	7.8	Corral Canyon rocks[e]	−59	305	172	1294, T
4	**1.4**	Newark volcanics II	−65	283	175	1702, T
3	1	Diabase dikes, Anitcosti, Quebec	−76	265	183	139, T
5	3.1	Combined dikes	−73	269	190	1932, T
6	3.3	Kayenta Formation[e]	−59	258	192	2380, T
3	7.2	Sil Nakya Formation[e]	−73	278	193	T
5	8.9	Piedmont dikes	−66	276	194	1796, T
4	**2.3**	Newark volcanics I	−63	263	195	1702, T
4	11.1	Connecticut Valley volcanics	−65	267	198	477, T
6	6	Moenave Formation[e]	−60	242	199	3058, T
5	7.9	Piedmont dikes	−62	235	199	1809, T
6	4.7	Passaic Formation, baked sediments	−60	249	200	2791, T
6	10.7	North Mountain Basalt	−67	249	200	1932, T
5	**4.0**	Hartford, Newark basalts and volcanics	−68	269	201	2278, T
5	6.2	Watchung basalts	−63	270	201	1339, T
5	6	Hettangian Newark red beds	−55	275	204	2312, T
5	2.4	Newark Martinsville core[f]	−59	278	206	2967, T
5	8	Chinle Group, Redonda Formation[f]	−59	257	209	2979, T

TABLE 3. (continued)

Q^a	$\alpha_{95}{}^b$	Formation and Country	$P_{lat}{}^c$	$P_{lon}{}^c$	Age (Ma)	GPDB[d]
4	9.8	Kayenta Formation[e]	−60	274	210	143, T
5	7	Kayenta Formation[e]	−62	266	210	153, T
6	2.5	Newark Weston core	−58	272	210	2967, T
5	3	Newark Basin both polar	−58	270	211	1339, T
6	4.2	Chinle Formation, Redonda Member	−58	259	212	152, T
7	5.6	Passaic Formation, C complex, Newark Group	−56	275	212	2312, T
6	2.8	Newark Somerset core	−57	277	213	2967, T
6	10.7	Chinle Formation[e]	−59	253	215	2800, T
6	3.1	Newark Rutgers core	−56	278	215	2967, T
6	3.4	Chinle Formation[e]	−58	256	218	2380, T
6	3.2	Newark Titusville cores	−56	280	218	2967, T
6	5	Newark Basin, Lower red beds	−54	282	219	2331, T
6	7.7	Dockum Group, Trujillo and Tecovas formations	−56	276	220	2944, T
6	5.1	Chinle, Sangre de Cristo[e]	−53	282	220	2979, T
6	2.5	Dan River-Danville Basin	−55	280	221	3171, T
4	3.9	Abbott pluton	−48	272	221	1831, T
6	5.6	Chinle Formation, Bull Canyon Member	−57	268	221	2380, T
5	2.6	Newark Nursery core[f]	−54	283	221	2967, T
6	2.6	Newark Princeton core[f]	−52	285	224	2967, T
6	3.2	Agamenticus pluton	−48	279	225	1831, T
7	5	Shinarump Member, Chinle Formation[e]	−60	279	226	2489, T
3	14	Popo Agie Formation, Chugwater	−56	276	230	1134, T
4	7	Manicouagan structure, Quebec	−60	271	230	434, T
3	10	Manicouagan structure, Quebec	−57	269	230	443, T
4	4.3	Ankareh Formation	−51	285	233	735, T
6	5	Upper Red Peak Formation	−49	285	235	1134, T
6	4.9	Moenkopi Formation, Anton Chico Member[e]	−45	301	238	2979, T
7	3.4	Moenkopi Formation[e]	−56	289	238	2489, T
5	4.9	Moenkopi Formation[e]	−56	279	240	571, T
6	4.5	Moenkopi Formation (upper)[e]	−56	285	241	2808, T
4	5.3	Moenkopi Formation[e]	−40	307	241	2632, T
5	7	Lower Red Peak Formation	−46	301	241	1134, T
5	2.5	Upper Moenkopi drill core[e]	−55	289	243	160, T
7	5	Moenkopi Formation (Gray Mountain)[e]	−55	286	243	1221, T
7	7.2	Lower Fundy Group, Nova Scotia	−45	277	243	2266, T
6	4	Chugwater Formation	−45	295	243	1266, T
6	3.3	Chugwater Formation	−47	294	243	1271, T
5	3.1	Upper Moenkopi Formation[e]	−53	291	243	159, T
4	12.8	Upper Maroon Formation[e]	−58	292	248	504, T
4	15	Ochoan red beds	−55	299	252	688, T
4	8	Bernal Formation[e]	−50	300	252	2489, T
3	5	Basic sill, Prince Edward Island	−52	293	252	431, T
6	5	Dewey Lake Formation	−51	306	254	2303, T
5	5	Guadalupian red beds	−51	305	260	688, T
7	3.6	Artinskian Pictou red beds	−42	306	264	2281, T
3	10	Toroweap Formation[e]	−52	305	275	688, T
5	16.3	Churchland pluton	−34	306	282	1264, T
4	5	Elephant Canyon Formation[e]	−42	302	283	671, T
4	2	Cutler Formation[e]	−41	302	283	671, T
4	13.1	Fountain and Lykins formations[e]	−45	306	283	504, T
4	2.8	Minturn and Maroon formations[e]	−40	301	283	1685, T
5	7.1	Cutler Formation, Lisbon Valley[e]	−41	308	283	1341, T
4	12.3	Cutler Formation[e]	−40	308	283	675, T
5	2	Ingelside Formation[e]	−43	308	283	1142, T
5	1.5	Upper Casper Formation	−51	303	283	1455, T
3	5	Leonardian subset	−52	299	283	688, T
5	2.1	Abo Formation[e]	−47	305	283	1311, T
4	6	Prince Edward Island red beds	−42	313	288	336, T
4	5.8	Prince Edward Island red beds	−41	306	288	276, T
5	2.1	Laborcita Formation	−42	312	290	1311, T
3	10	Piedmont mafic intrusions	−39	301	292	1527, T
5	3.4	Wescogame Formation (Supai)[e]	−44	305	296	1311, T
3	10	Hurley Creek Formation	−39	305	296	445, T
3	4	Tormentine Formation, Prince Edward Island	−41	312	296	336, T
4	**4.2**	Brush Creek Limestone	−36	304	296	1523, T
5	1.8	Lower Casper Formation	−46	309	297	1455, T
5	3.9	Dunkard Formation	−44	303	300	302, T
5	6	Riversdale Group	−36	302	310[f]	1110
6	7	Barachois Group	−34	323	320[f]	1534
7	4.6	Shepody Formation	−36	304	320	2484

TABLE 3. (continued)

Q^a	$\alpha_{95}{}^b$	Formation and Country	$P_{lat}{}^c$	$P_{lon}{}^c$	Age (Ma)	GPDB[d]
7	4	Maringouin Formation, Nova Scotia	−32	301	323[f]	2484
7	9	Deer Lake Formation, West Newfoundland	−22	302	330[f]	1482
6	8	Jeffreys Village Member, West Newfoundland	−27	311	333[f]	1534
		Europe				
4	3.6	West Eifel volcanics	−80.6	267.5	0.5	1513
4	4.4	East Eifel volcanics	−86.4	296.1	0.5	1505
3	12.9	Volcanics NW Germany	−84.3	357.7	8	56, SV
5	6.9	Velay Oriental volcanics	−84.1	251.2	11.5	3324
4	4.4	Volcanics Germany	−77.8	310.8	24	3282, SV
3	3.4	Hocheifel Tertiary volcanics	−80.8	2	34	1506, SV
5	1.5	Lundy Island dikes, Wales	−83	335	49.5	755, T
4	2	Sleat dikes, Scotland	−82	338	51	1174, T
5	10	Fishnish dikes, Scotland	−74	319	52	1040, T
7	2.7	Mull dikes, Scotland	−78	7	53.5	83, T
5	3.5	Vaternish dike swarm, Scotland	−76	340	55	85, T
5	1.2	Arran dikes, Scotland	−82	0	55	1041, T
5	2.7	Muck and Eigg igneous, Scotland	−74	351	58	1204, T
6	2.4	Rhum and Canna igneous, Scotland	−81	359	59	1169, T
4	2.7	Ardnamurchan Complex, Scotland	−77	355	59.5	1377, T
4	5	Antrim basalts, Ireland	−70	343	59.5	654, T
6	4.5	Faeroe flood volcanics	−71.4	334.7	59.5	3494
5	2.8	Mull lavas, Scotland	−72	348	59.5	1055, T
3	2.5	Skye Lavas, Scotland	−72	345	59.5	86, T
7	8	Aix-en-Provence sediments, France	−73	336	74	2393, T
5	3	Dagestan limestones, northern Caucasus	−74	341	86	3037, T
5	3	Dagestan limestones, northern Caucasus	−74	328	86	3037, T
4	5	Munsterland Turonian, Germany	−68	329	89.5	1507, T
5	4	Munster Basin Limestone, Germany	−76	1	93	1495, T
6	2.9	Berriasian limestones	−74	3	140	1397, T
5	6	Jura Blue Limestone, Switzerland	−78	328	156.5	1337, T
3	3.9	Oxfordian sediments	−70	327	157	616, T
5	7	Terres Noires, France	−78	310	158	3156, T
4	4	Subtatric nappe sediments	−72	312	159	1948, T
6	7.3	Limestones, Krakow-Czestochowa Upland	−72	330	159	1948, T
4	7	Krakow Upland sediments, Poland	−72	330	162.5	1948, T
7	6.3	Jurassic sediments	−63	300	168	1514, T
7	6	Alsace Bajocian sediments, France	−63	300	178	1514, T
6	6.8	Scania basalts, Sweden	−69	283	179	2720, T
6	12	Thouars and Airvault sections	−71	276	184	1427, T
4	3	Liassic sediments	−77	315	192	1467, T
4	7	Liassic volcanics, France	−65	324	198	481, T
5	7.5	Kerforne dikes, Brittany, France	−61	259	198	2743, T
7	3	Paris Basin sediments, France	−51	285	201	3029, T
6	9	Hettangian-Sinemurian Limestone France	−55	280	201	3141, T
6	8	Rhaetian sediments, Germany, France	−50	292	208	3141, VT
5	5.1	Merci mudstone, Somerset, United Kingdom	−50	308	215	3311, VT
5	4.6	Sunnhordland dikes, Norway	−50	305	221	VT
6	6	Gipskeuper sediments, Germany	−49	311	226	3141, VT
6	12	Musschelkalk carbonates, Poland	−53	303	234	3253, VT
6	3	Heming Limestone, Paris Basin, France	−54	321	234	2411, VT
5	15	Bunter and Musschelkalk, Germany	−49	326	239	158, VT
4	7	Kingscourt red beds, Ireland	−59	326	242	VT
6	5	Upper Buntsandstein, France	−43	326	243	1028, VT
5	5.9	Lunner dikes, Oslo, Norway	−53	344	243	3188, VT
6	3.8	Volpriehausen Formation, basal mid-Buntstein, Germany,	−49	348.2	246	S2004
7	3.3	Germanic Trias, Lower Buntstein, Germany	−50.6	345.6	249	S2003
6	5	Sudetes sediments, Poland	−50	343	251	3161, VT
6	4	Massif des Maures, France	−51	341	255	1408, VT
5	2.7	Dome de Barrot red beds, France	−46	327	255	652, VT
5	5	Esterel sediments, France	−47	331	261	165, VT
6	4	Brive Basin sediments, France	−49	343	261	3144, VT
5	4	Saxonian Red Sandstone, France	−51	324	264	2361, VT
3	4.6	Upper Lodeve Sandstone, France	−47	336	264	168, VT
5	6.1	Esterel extrusives, France	−51.5	322	264	165, VT
5	1.5	Lodeve Basin, France	−49	334	264	1813, VT
4	0	Permian red beds, Lodeve Basin, France	−53	331	264	1207, VT

TABLE 3. (continued)

Q^a	$\alpha_{95}{}^b$	Formation and Country	$P_{lat}{}^c$	$P_{lon}{}^c$	Age (Ma)	GPDB[d]
4	8.6	Bohuslan dikes combined, Sweden	−51	345	275	1155, VT
4	11	Scania melaphyre dikes, Sweden	−54	352	279	2222, VT
3	0	Brumunddal lavas, Norway	−47.8	317.7	279	169, VT
4	6.7	Moissey volcanics, Jura, France	−41	352	279	1205, VT
3	14	Mauchline lavas, Scotland	−47	337	280	3093, VT
5	10	Bohemian Massif igneous, Germany	−42	346	280	2356, VT
4	7	Bohemian quartz porphyry, Germany	−37	341	280	3145, VT
4	6.9	Sarna alkaline intrusion, Sweden	−38	346	281	1735, VT
4	13.4	Ringerike lavas, Norway	−44.6	337.4	281	VT
5	1	Oslo volcanics, Norway	−47	337	281	915, VT
5	4	Bohemian red beds, Czech Republic	−41	345	285	167, VT
5	6.3	Mount Hunneberg Sill, Sweden	−38	346	285	2211, VT
5	2	Lodeve Basin, France	−42	349	285	1813, VT
5	2	Krkonose Basin oil shales, Czech Republic	−40	346	285	2444, VT
5	3.2	Intrasudetic Basin volcanics, Poland	−43	352	285	3161, VT
3	7.7	Lower Lodeve Sandstone, France	−44	350	285	168, VT
4	6.8	Intrasudetic basin sediments, Poland	−37	340	285	3161, VT
4	8.1	North Sudetic basin volcanics, Poland	−42	354	285	3161, VT
4	17	Lodeve B Complex, France	−49	342	285	2454, VT
3	13.2	Lower Silesia, Poland	−40	352	285	465, VT
5	5.1	North Sudetic basin sediments, Poland	−44	4	285	3161, VT
4	7.9	Krakow volcanics, Poland	−43	345	285	275, VT
4	10	Exeter lavas, United Kingdom	−48	343	286	411, VT
5	4	Exeter lavas, United Kingdom	−50	330	286	165, VT
3	1	Black Forest rhyolites, Germany	−42	353	286	2941, VT
4	5.9	Black Forest volcanics, Germany	−49	356	286	170, VT
4	5.8	Thuringer forest sediments, Germany	−41.5	340	287	1792, VT
3	13	Nahe volcanics, Germany	−46	347	291	940, VT
3	15.9	Saar-Nahe volcanics, Germany	−41	349	291	712, VT
4	2.4	Stabben Sill, Norway	−32	354	291	1540, VT
6	13	Sudetic Mountain granitoids, Poland	−42	346	293	2446, VT
5	6.5	Scania dolerites, Sweden	−38	348	294	2222, VT
3	19	Lower Nideck volcanics, France	−42	348	294	174, VT
4	4	Nideck-Donon volcanics., France	−47	348	294	1010, VT
5	11	Scania dolerite dikes, Sweden	−37	354	294	2211, VT
4	4.8	Great Whin Sill, United Kingdom	−44	339	294	585, VT
5	6.3	Holy Island Sill and dike (Whin Sill)	−35.4	346.8	294	L2004
5	8.1	Alnwick Sill-High Green-Oswalds Chapel dike (Whin Sill)	−47.1	337.1	294	L2004
5	3.5	Hadrian's Wall-Pennines Sill and Hett dike (Whin Sill)	−32.9	347.1	294	L2004
4	7.1	Thuringer Forest volcanics, Germany	−37.1	350	295	1792, VT
4	13.6	Lower Silesia volcanics, Poland	−43	354	296	465, VT
5	1.3	Peterhead dike, Scotland	−41	342	297	1535, VT
4	2.9	Ny-Hellesund sills, Norway	−39	341	297	626, VT
3	7.1	Arendal diabase dikes, Norway	−42.5	339.6	297	175, VT
5	4	Mount Billingen Sill, Sweden	−31	354	299	2211, VT
3	3	Wackerfield dike, United Kingdom	−49	349	303	180, VT
5	9	Westphalian-Stephanien red beds, Czech Republic	−38	343	305	167, VT
5	5.2	Queensferry Sill, Scotland	−38.3	354	305	2447, VT
6	8.2	Derbyshire lavas, England	−14.3	335.9	335	2440
5	1.9	Magerøy dikes, Norway	−14.4	318.1	337	3527
		Greenland				
6	7.4	Talerua lavas	−76.3	21.5	39	S2005
6	6.2	West Greenland combined	−73.6	340.5	58	R2003
6	4.5	coast-parallel dike swarm combined	−73.4	358.2	135	T
		Northwest Africa				
4	6.7	Famara volcanics	−87.5	358.2	7.5	2938
3	5.2	Basalts Series II	−77.8	326.2	8	1493
4	4.1	Miocene volcanics	−81.9	294.4	13	25
3	2.3	Massif de Cavallo	−86.8	202.9	13	555
5	8	Basalt series I, Gran Canaria, Spain	−72	71.2	81	1493, TV
4	14	Intrusives, Beni Mellal, Morocco	−46	78	120	1859, TV
6	6.3	Upper Jurassic sediments, Tunisia	−65.2	20.3	152.5	1167, TV
3	19.2	Intrusive rocks, Nigeria	−62.5	61.6	160	1081, TV
4	11	Beni Mellal basalts, Morocco	−45	68	173.5	1859, TV
6	9	Beni Mellal volcanics, Morocco	−44	71	173.5	148, TV
5	7.4	Diabase dikes and sills, Liberia	−68.5	62.4	185.5	140, TV
4	4.1	Hank volcanics, North Mauritania	−69.4	52	187	3259, TV
4	6.1	Hodh volcanics, South Mauritania	−71.4	60.2	187	3260, TV
4	6.2	Freetown Complex, Sierra Leone	−82.9	32.7	193	3287, TV

TABLE 3. (continued)

Q^a	$\alpha_{95}{}^b$	Formation and Country	$P_{lat}{}^c$	$P_{lon}{}^c$	Age (Ma)	GPDB[d]
3	0	Moroccan intrusives, Morocco	−71	36	200[f]	148, TV
5	**18.5**	Central Atlantic Magmatic Province, Morocco	−73	61.3	200	K2004
3	12	Argana red beds, Morocco	−50.6	71.4	200[f]	1080, TV
6	2.6	Zarzaitine Formation, Algeria	−70.9	55.1	206.5	2932, TV
3	11.5	Upper Triassic sediments, southern Tunisia	−54.9	43.3	221.5	3020, TV
3	7.8	Djebel Tarhat red beds, Morocco	−24	63.8	273	1080, TV
5	4.7	Chougrane red beds, Morocco	−32.2	64.1	273	723, TV
5	6	Serie d'Abadla, Upper Unit, Morocco	−29	60	273	1459, TV
3	4.6	Taztot Trachyandesite, Morocco	−38.7	56.8	273	723, TV
5	3.6	Abadla Formation, Lower Unit, Algeria	−29.1	57.8	275	3275, TV
3	20.9	Volcanics, Mechra Abou-Chougrane, Morocco	−36	58	280.5	1859, TV
5	2.8	Upper El Adeb Larache Formation, Algeria	−38.5	57.5	286.5	2540, TV
4	4.1	Lower Tiguentourine Formation, Algeria	−33.8	61.4	290	2728, TV
5	3.5	Lower El Adeb Larache Formation, Algeria	−28.7	55.8	307	2540, TV
6	4.6	Illizi Basin, Algeria	−28.3	58.9	309	3484
4	4.1	Ain Ech Chebbi and Hassi Bachir formations, Algeria	−25.4	54.8	316	1629, TV
4	4.5	Oubarakat and El Adeb Larache formations, Algeria	−28.2	55.5	317	3481
7	5.3	Reggane Basin, Algeria	−26.6	44.7	320	3402, TV
		Northeast Africa				
5	4.1	Afar stratoid series, Ethiopia	−87.5	359.3	1	3336[g]
5	5.7	Stratoid basalts, Ethiopian Afar, Ethiopia	−87.2	37.1	2	3559[g]
5	4.1	Gamarri section lavas, Afar depression, Ethiopia,	−79.7	350.2	2.5	3234[g]
5	8.3	Volcanics, Jebel Soda, Libya	−78.4	16.1	11.5	50
5	11.2	Volcanics, Jebel Soda, Libya	−69	4	11.5	60
4	12.7	Ethiopian flood basalts, Abbay and Kessen gorges, Ethiopia	−83	13.3	26.5	3496
6	6	Qatrani Formation, Egypt	−79.6	332.2	29	3280
5	5.4	Ethiopian Traps, Ethiopia	−77.9	32.8	30	3209
4	8.4	Southern Plateau volcanics, Ethiopia	−75.1	350.3	34	2764
5	6.4	Iron ores combined, Baharia Oasis, Egypt	−83.5	318.6	37	1500
6	4.2	Mokattam Limestone, Egypt	−78.1	342.8	42.5	3280
3	5.8	Basalts, Wadi Abu Tereifiya, Egypt	−69.4	9.4	44.5	1141
5	8.5	Wadi Natash volcanics, Egypt	−69.3	78.1	93	1500, TV
3	18.1	Wadi Natash volcanics, Egypt	−75.7	48.3	94.5	3260, TV
4	5.5	Al Azizia Formation, NW Libya, Libya	−54.5	45.8	231	3408
5	3.8	Al Azizia Formation, NW Libya, Libya	−59.3	34.1	231	3408
4	6	Jebel Nehoud Ring Complex, Kordofan, Sudan	−40.8	71.3	280	3504
3	7.2	Abu Durba sediments, SW Sinai, Egypt	−25.6	64	306.5	2784, TV
		Australia				
4	4.4	Werriko Limestone, newer volcanics, Victoria	−83.2	103.6	3	1201
5	1.9	Hematized Hawkesbury Sandstone, New South Wales	−82.9	114.4	15.5	1646
		East Antarctica				
5	**6.3**	McMurdo volcanics combined	−87.3	137.3	2	1319
5	4.4	Lavas and dikes, Vestfjella	−51.4	203.4	164	1548, TV
4	3.4	Ferrar dolerites, northern Prince Albert Mountains	−47.8	225.5	176.5	2721, TV
3	3.3	Ferrar dolerite sill, Mount Cerberus, dry valleys	−57.8	224.3	176.5	1838, TV
5	2.4	Ferrar dolerites, Wright Valley	−45.3	208	176.5	1599, TV
5	10.2	Ferrar dolerite, McMurdo Sound	−50.5	211.4	176.5	1657, TV
4	6.9	Storm peak lavas, Queen Alexandra Range	−44.1	231.5	193	808, TV
5	3.8	Vestfjella lavas and dikes	−41.8	226.5	195	1154, TV
		Madagascar				
5	4.4	Antanimena and Mailaka volcanics	−74	43.7	86.5	3482
4	7.6	Volcanics, Massif d'Androy Andria	−64	63	87	547, TV
4	4.9	Volcanics, Antanimena Andria	−66.1	49.7	87	708, TV
4	4.4	Volcanics, southeast coast Andria	−65.8	35.6	87	708, TV
4	8.9	Volcanics, Mangoky-Anilahy Andria	−73.7	73.1	87	708, TV
5	4.3	Dolerites, east Madagascar	−65.5	38	87	TV
4	6.9	Volcanics, Mailaka Andria	−70.3	63.1	87	708, TV
5	2.4	Volcanics, southwest Madagascar	−76.8	68.2	87	3210, TV
5	10.7	d'Analava Complex	−66.7	43.5	91	M2006

TABLE 3. (continued)

Q^a	$\alpha_{95}{}^b$	Formation and Country	$P_{lat}{}^c$	$P_{lon}{}^c$	Age (Ma)	GPDB[d]
3	5.9	Isalo Group	−74	97.1	206.5	147, TV
3	7.6	Combined Sakamena	−76.7	110.8	250.5	TV
3	9.5	Combined Sakoa	−51.3	72.6	305	TV
		South America Craton				
5	10	Lipiyoc Formation, Puna, Argentina	−85.7	80.5	8.5	3027
5	10	El Loa Formation and associated ignimbrites, Chile	−85.4	303.8	8.5	3323
5	11.4	Remedios, Sao Jose formations, Fernando de Noronha, Brazil	−84.5	316	9.5	1404
5	5.9	Itatiaia and Passa Quatro complexes, SE Brazil	−79.5	0	72	3261, TV
5	4.2	Sao Sabastiao Island intrusions, SE Brazil	−79.4	331.9	80.5	3261, TV
6	2.6	Pocos de Caldas Alkaline Complex, SE Brazil	−83.2	320.1	83	3261, TV
3	4.8	Intrusives, Cabo de Santo Agostinho, Brazil	−87.6	315.1	92	1448, TV
4	2.8	East Maranhao intrusives, Maranhao Basin, Brazil	−83.6	81	118	1431, TV
6	2.6	Florianopolis dike swarm, Santa Catarina Island, Brazil	−89.1	3.3	123.5	3190, TV
6	2	Ponta Grossa dikes, Brazil	−82.4	30.3	131	2958, TV
4	14.1	Dikes, Rio Grande do Norte, NE Brazil	−80.6	275	146	1509, TV
3	9.3	West Maranhao basalts, Maranhao Basin, Brazil	−85.3	262.5	175	1431, TV
5	3.8	Anari and Tapirapua formations, western Brazil	−65.5	250.3	196.5	3316, TV
4	4.9	Bolivar dikes, Venezuela	−66.9	245.6	202.5	150, TV
4	10	Dolerite dikes, Suriname	−82	320	232	701, TV
6	6	Mitu Group red beds, Bagua Grande, Peru	−71.4	303.6	248.5	3524
3	11.2	Itarare Subgroup, Tubarao Group, Brazil	−57	357	306.5	798, TV
		Parana-Salado				
5	7.8	Andean foreland-basin sediments, Argentina	−82.4	221.8	11.5	3347
3	6	Rio de Los Molinos dikes 1, Cordoba, Argentina	−77	18	65.5	102, TV
4	8	Pirgua basalts and red beds, Argentina	−85	222	95.5	1131, TV
4	3.7	Serra Geral basalts, Brazil	−84.6	115.4	119	765, TV
3	10.4	Vulcanitas Cerro Colorado Formation, Cordoba, Argentina	−81	14	121	123, TV
5	5.9	El Salto-Almafuerte lavas, Cordoba, Argentina	−72	25	124	1087, TV
3	11	Rio de Los Molinos dikes 2, Cordoba, Argentina	−79	8	139.5	102, TV
4	7	Amana Formation, Paganzo Group, Argentina	−83	317	240	1132, TV
3	4	Mendoza lavas, south Nihuil, Argentina	−81	282	243	560, TV
3	14	Sierra de la Ventana red beds, Argentina	−78	219	250.5	560, TV
3	3.3	La Colina Formation, Paganzo Village, Argentina	−81	327	267.5	166, TV
3	3.1	La Colina Formation, Los Colorados 1, Argentina	−74	313	267.5	166, TV
4	4	Lowest middle Paganzo, Argentina	−66	326	273	283, TV
3	2.5	Middle Paganzo II, Los Colorados lower beds, Argentina	−59.5	357.5	273	620, TV
3	3	La Colina Formation, Paganzo Group, Argentina	−78	249	278	1132, TV
4	5.7	La Tabla Formation, Chile	−51	347	284	1420, TV
3	5	La Colina basalt, Argentina	−66	348	300	178, TV
6	9.6	Pular and Cas formations, Chile	−57	350	306.5	1420, TV
6	0	La Colina Formation, Argentina	−49	343	306.5	1144, TV
		Colorado				
6	4.3	Patagonian Plateau basalts, Chile, Argentina	−78.7	358.4	71.5	2374, TV
4	4.9	Chon Aike Formation, combined result, Argentina	−85	197	170	133, TV
5	8.7	Marifil Formation, Patagonia, Argentina	−83	138	177	3535
6	8.5	Tepuel Group, western Patagonia, Argentina	−31.7	316.1	318	2805, TV
		India-Pakistan				
4	5.4	Mount Pavagarh Traps, Gujrat, India	−39.2	105.6	64	94, TV
4	6.7	Deccan Traps, Mahabaleshwar, India	−40	96	65.5	107, TV
6	5.9	Deccan Traps, Nagpur to Bombay traverse, India	−38.4	102.4	65.5	393, TV
3	3.8	Deccan Traps, Western Ghats, India	−34.5	103.6	65.5	705, TV

TABLE 3. (continued)

Q^a	$\alpha_{95}{}^b$	Formation and Country	$P_{lat}{}^c$	$P_{lon}{}^c$	Age (Ma)	GPDB[d]
5	9.4	Deccan dike swarms, western India	−37.2	100.5	65.5	3094, TV
3	3.8	Deccan Traps, Jalna	−39	99	65.5	686, TV
4	10.1	Central Kerala dikes, India	−34.6	94	69	2754, TV
4	12	Central Kerala gabbro dike, India	−21.6	119.4	88	2754, TV
5	7.5	St. Mary Island rhyolites	−14.2	117.8	91.2	TV
3	4	Rajmahal Traps, West Bengal and Bihar, India	−3	118	116	633, TV
6	3.5	Rajmahal Traps, Bihar, India	−7	117	116	678, TV
6	8.3	Rajmahal Traps, West Bengal, India	−9.3	124.8	116	2977, TV
4	5.5	Rajmahal Traps, North Rajmahal Hills, India	−6.5	120.2	116	T2001
3	7	Sylhet Traps, Khasi Hills, India	−16	121	116.5	985, TV
5	2.4	Rajmahal Traps, Bihar, India	−9.4	116.6	117	3095, TV
5	4.6	Pachmarhi beds, central India	−10.1	130.1	206.5	593, TV
4	4.6	Mangli beds, central India	7.3	124.3	243	593, TV
5	6	Panchet clays, Karanpura coalfields, India	7.5	120.5	248.5	162, TV
6	4.3	Wargal and Chhidru formations, Salt Range, Pakistan	2.2	125.8	250.5	2467
6	6.5	Kamthi red beds, Wardha Valley, central India	4	129	250.5	163, TV
3	1.8	Kamthi beds, Tadoba, India	4.1	102.8	250.5	593, TV
3	12.1	Alozai Formation, Baluchistan, Pakistan	18.1	111	289.5	1236
		South Africa				
5	3.8	Ngorora Formation, Kenya	−85.7	75.8	11.5	3111
4	8.8	East African volcanics, Kenya and Tanzania	−86.5	6.6	12	774
3	10	Volcanics, Kenya	−80.1	214.2	13.5	1517
5	3.1	Turkana lavas, Kenya	−84.6	343.3	17	774
5	**5.2**	Cretaceous kimberlites 1, South Africa, Lesotho	−64.1	46.1	90.5	2293, TV
4	3	Lupata series volcanics, Mozambique	−61.8	79.5	111	992, TV
3	9.3	Mlanje Massif Syenite, Malawi	−60	82	124.5	401, TV
6	**9.7**	Cretaceous kimberlites 2, South Africa	−47.6	89.9	129	2293, TV
5	3.1	Kaoko lavas, Namibia	−48.3	86.6	132	126, TV
3	15.8	Hoachanas lavas, Namibia	−61.9	71.9	171	126, TV
5	3.2	Stormberg lavas (Lesotho basalts), South Africa, Lesotho	−71.6	93.5	180	3090, TV
4	11	Stormberg lavas, Sani Pass and Maseru, Lesotho	−70.5	88.7	180	984, TV
4	13.3	Batoka basalts, Zimbabwe	−64	80.6	180[f]	J2001
3	7	Karroo lavas, central Africa, Zimbabwe, Mozambique,	−57	84	180[f]	635, TV
5	9.5	Karroo dolerites combined, South Africa, Zimbabwe	−65.4	75.1	180[f]	317, TV
5	8.7	Marangudzi Ring Complex, Zimbabwe	−70.7	106.7	186	470, TV
3	4.6	Red Sandstone Formation, Zambia	−68	50.5	221.5	323, TV
3	6	Cassanje series, Angola	−54	80	248.5	1960, TV
4	5.3	Permian red beds, Tanzania	−26.9	85.1	254	2736, TV
3	12	K3 beds, Songwe-Ketewaka coalfields, Tanzania	−27.6	89.8	257	324, TV
3	5	K3 beds, Galula coalfield, Tanzania	−46	40	257	324, TV
6	5.6	K1 Dwyka varves, Zimbabwe, Zambia, Tanzania	−26.5	26.5	281.5	435, TV
6	12	Dwyka Group combined	−25	67	315	3489

[a] Q is the *Van der Voo* [1993] classification factor (7 is best score).
[b] Here α_{95} = 95% confidence circle (*A*95 indicated in bold).
[c] P_{lat} and P_{lon} are paleomagnetic pole latitude and longitude, respectively.
[d] Abbreviations are GPDB, Global Paleomagnetic Data Base Reference Number (REFNO of *McElhinny and Lock* [1996]).; T, listed by *Torsvik et al.* [2001]; SV, listed by *Si and Van der Voo* [2001]; TV, listed by *Torsvik and Van der Voo* [2002] (some ages adjusted here); and VT, listed by *Van der Voo and Torsvik* [2004] (major changes in age in this paper); L2004, *Liss et al.* [2004]; S2004, *Szurlies* [2004]; S2003, *Szurlies et al.* [2003]; S2005, *Schmidt et al.* [2005]; M2006, *Meert and Tamrat* [2006]; T2001, *Tarduno et al.* [2001]; R2003, *Riisager et al.* [2003]; K2004, *Knight et al.* [2004]; and J2001, *Jones et al.* [2001].
[e] Value is corrected for counterclockwise rotation of 5.4° [*Bryan and Gordon*, 1990].
[f] Revised age is given (note that many pole ages have been revised in earlier publications as listed above).
[g] Small-scale rotation is possible.

this issue we attempted to "reproduce" the more smoothed *Schettino and Scotese* [2005] APW path simply by increasing the window length with the running mean method. We found that our APW path can mimic their path if we use a window length of at least 50 Ma (red line with blue cones of confidence ovals in Figure 5d).

[18] We calculated the APW for 10 Ma bins since the Carboniferous from the running mean path of Figure 5a. This magnitude of APW is shown in Figure 5e as the maroon histogram pattern, whereas the APW calculated from the smoothed spherical spline path of Figure 5c is shown as the black transparent histogram pattern in Figure 5e. The latter removes practically all temporal variation in APW, and notably, it eliminates the 110–100 Ma peak (~13 cm/a), which is so visible in the running mean-based path. A detailed examination of paleopoles between 90 and

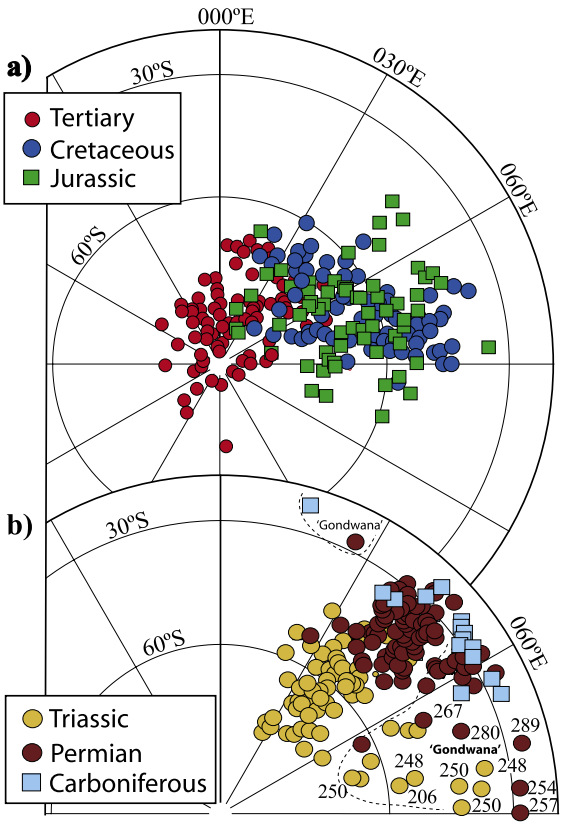

Figure 4. The 419 paleomagnetic results selected for the analysis of this paper (Table 3) and plotted as south poles in South African coordinates, using the rotation parameters listed in Tables 1 and 2. (a) Poles <200 Ma and (b) poles >200 Ma and <320 Ma. Note that many "Gondwana" south poles in Figure 4b plot at significantly more easterly longitudes for Late Permian and Triassic times. The numbers next to these Gondwana poles are their ages (Ma).

120 Ma (as used to calculate the running mean path and shown in Figure 6a) clearly illustrates that this peak is real (even when smoothed because of the 10 Ma moving window overlap) because there is indeed a "systematic" progression of the Cretaceous poles for this interval. Hence the spherical spline path has smoothed away this important short-time APW feature.

3.4. Plate Motion Chains and the Pangea Enigma

[19] Different Euler rotations for *relative plate motions* can produce significant differences between global APW paths. Most of our Euler rotations (Tables 1 and 2) differ from those of *Besse and Courtillot* [2002], where finite (Euler) rotations were largely recomputed from the *Müller et al.* [1993] model described in section 4. Conversely, many Euler rotations of *Schettino and Scotese* [2005] were calculated by inversion of the digital ocean seafloor grid of *Müller et al.* [1997]. Different choices will naturally affect the resultant global APW path. Moreover, we have extended our APW path back to 320 Ma, which introduces some additional enigmas.

[20] Paleomagnetic poles are calculated under the routine assumption that the time-averaged geomagnetic field is that of a *geocentric axial dipole*. However, *Van der Voo and Torsvik* [2001] have suggested that nondipole field contributions may have persisted through significant periods of Earth history. Most Earth scientists agree that before the onset of breakup, the Jurassic "Pangea A" reconstruction is the correct one, in which NW Africa is located adjacent to the Atlantic margin of North America (Figure 3a). For Permian times, however, the paleomagnetic poles do not agree with the Pangea A fit of Figure 3a, as can be seen by examining the discrepancy between the poles from Gondwana and those for Laurussia in Figures 4b and 6b. To reconcile the paleomagnetic misfit, one has the option of (1) modifying the Pangea A reconstruction or (2) dismissing much of the database as contaminated by later magnetic overprints or (3) arguing that the mean pole positions are imprecise because of rock magnetic recording problems, such as those caused by sedimentary inclination shallowing [e.g., *Kodama*, 1997; *Rochette and Vandamme*, 2001; *Torsvik and Van der Voo*, 2002; *Kent and Tauxe*, 2005]. A fourth solution is to hypothesize significant *octupole* field contributions, in which case the Pangea misfit is caused by inferring a too far northerly position of Gondwana from the geocentric axial dipole hypothesis, as well as a too far south position for Laurussia [*Van der Voo and Torsvik*, 2001, 2004; *Torsvik and Van der Voo*, 2002]. Latitudinal errors caused by 5–10% octupole field contributions are comparable to inclination shallowing effects in sediments. All four of these explanations have been presented in previous publications [see *Van der Voo*, 1993; *Muttoni et al.*, 2003; *Irving*, 2004; *Van der Voo and Torsvik*, 2004, and references therein]. The largest misfit is seen at 250 Ma (Figure 6b), likely because the data are indeed not very reliable for this interval, as argued by *Muttoni et al.* [2003].

[21] In general, the number of poles from Laurussia is larger (and, on average, of higher data quality) than similarly aged poles from Gondwana, and they will therefore bias the global path. Since the incorporation of nondipole contributions is controversial, we opted in this paper to only analyze geocentric axial dipole–based APW paths. However, we should mention that the debate about the various Pangea reconstructions has not subsided [see *Irving*, 2004] and that different Pangea fits labeled A2 and B (or less commonly C or D) remain favored even in recent literature. Since nondipole field contributions remain an open possibility, we refer to Table 4 (see column labeled SAFR**) for a comparison of our geocentric axial dipole–based APW path with one that incorporates time-dependent nondipole fields (0–17.5% octupole contributions) [*Torsvik and Van der Voo*, 2002]. On average, however, this alternative path differs by only 2.0° ± 1.3° (great circle distance between poles of same mean age).

3.5. Paleomagnetic Euler Pole Analysis

[22] Movements of continents, APW paths (in the absence of *true polar wander*), tracks of hot spots (if fixed to the mantle), and ocean fracture zones all should represent

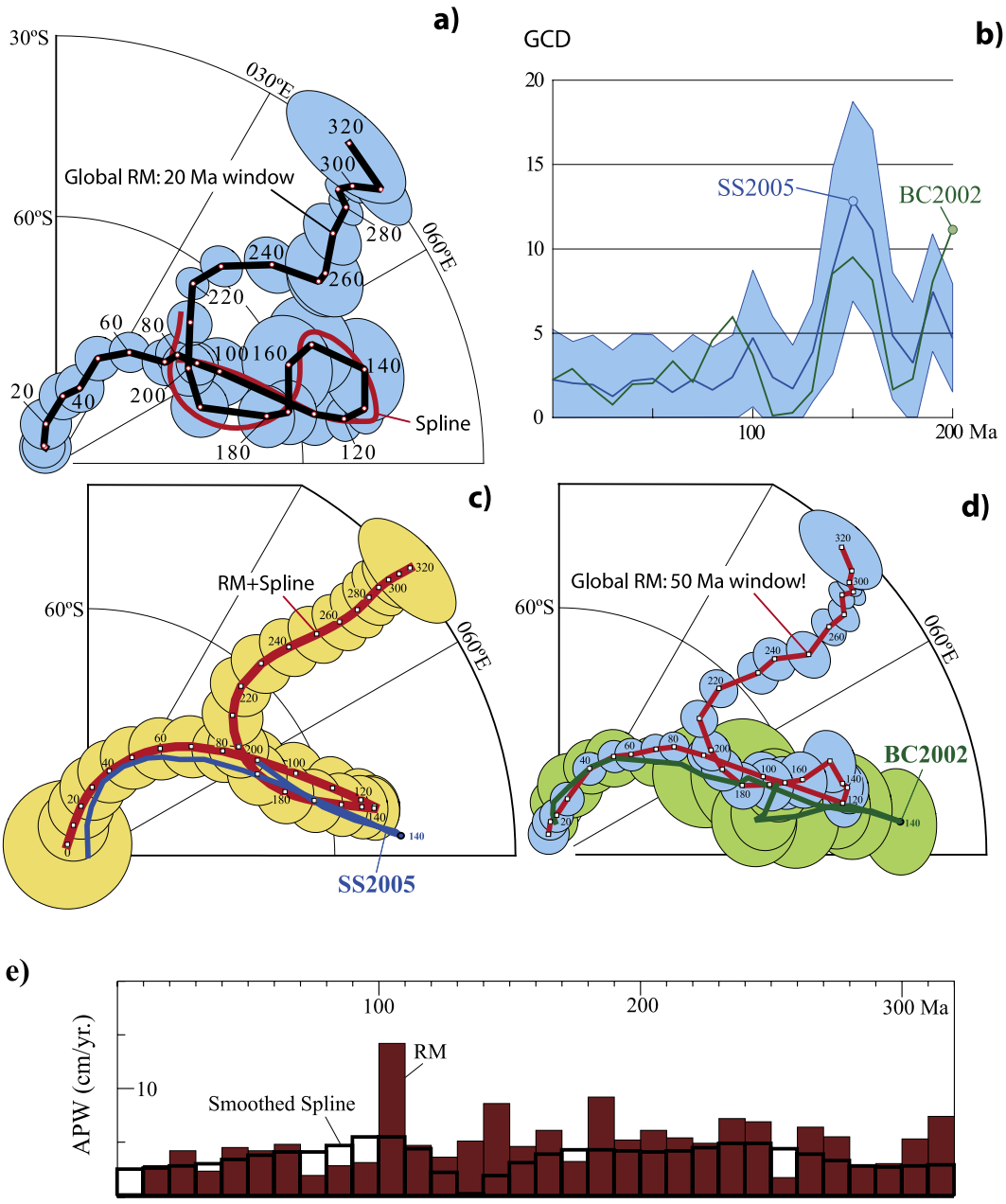

Figure 5. (a) Global running mean (RM) apparent polar wander (APW) path (thick black line with blue confidence circles, A_{95}) in South African coordinates, with ages in million years. This path is generated with a 20 Ma moving window, incremented at 10 Ma intervals. The red line is a spherical smoothed spline path (smoothing parameter is 1000) [see *Torsvik et al.*, 1996; *Jupp and Kent*, 1987]. The spline path uses raw data (70–210 Ma), which are weighted by their Q factor; see text for details. (b) Great circle distances (GCD) between the running mean path of Figure 5a and the APW paths of *Schettino and Scotese* [2005] (SS2005) and *Besse and Courtillot* [2002] (BC2002). The SS2005 path comparison is shown together with the errors in our RM path. (c) A spherical, smoothed spline path (smoothing parameter is 700) based on a running mean path (without data overlap, just binned) and with weighting of input poles according to A_{95}. The A_{95} values for the output spline path will increase with increased smoothing because the spline is farther and farther displaced from the real input poles. This heavily smoothed spline path (red) is compared with the SS2005 APW path (blue). No errors were provided in the SS2005 model. (d) A running mean APW path, which uses extreme smoothing (window length of 50 Ma), shown together with the BC2002 path with light green–shaded A_{95} ovals. (e) Calculated APW rates (for 10 Ma intervals) using our global RM path of Figure 5a and the smoothed spline path of Figure 5c.

TABLE 4. Global Apparent Polar Wander Path in South African, North American, European, South American Craton, Indian, and Australian Coordinates[a]

			Coordinates													
			SAFR		SAFR**		NAM		EUR		SAC		IND		AUS	
Age (Ma)	N	A_{95}	Lat	Long	Lat	Long	Lat	Long	Lat	Long	Lat	Long	Lat	Long	Lat	Long
0	18	3.0	−87.8	326.0	−89.2	297.9	−87.6	322.4	−87.6	313.6	−87.7	307.3	−89.1	22.3	−89.2	120.0
10	30	2.5	−87.6	323.9	−88.8	86.3	−87.2	318.4	−87.2	305.0	−87.3	292.8	−88.7	71.9	−87.5	134.0
20	23	3.0	−85.3	345.5	−85.3	49.3	−84.6	331.2	−85.0	317.4	−84.9	292.3	−84.8	86.1	−82.3	123.0
30	18	2.8	−82.1	5.8	−83.2	26.4	−81.6	343.6	−82.7	332.5	−83.2	302.8	−79.4	91.0	−76.5	115.6
40	19	2.8	−80.8	17.5	−81.6	38.4	−80.9	345.2	−82.3	330.5	−82.8	299.6	−74.2	100.0	−72.2	118.4
50	27	2.6	−76.8	21.6	−78.8	41.1	−77.1	349.8	−79.1	334.2	−80.4	311.7	−63.9	95.3	−70.2	113.9
60	30	2.4	−74.3	33.5	−74.2	46.3	−75.1	4.1	−79.0	346.8	−80.9	331.7	−51.6	96.4	−66.3	112.3
70	20	2.7	−72.5	47.2	−69.5	51.8	−74.3	17.1	−80.3	1.8	−82.0	354.0	−39.0	99.6	−61.9	114.5
80	23	2.6	−70.8	48.1	−69.4	49.2	−75.4	5.7	−79.6	350.0	−82.5	330.3	−28.5	104.7	−64.0	121.0
90	27	2.6	−69.5	54.7	−68.4	55.1	−76.4	5.8	−80.3	349.1	−84.0	323.3	−23.5	108.9	−62.8	127.4
100	11	4.1	−67.7	60.8	−67.2	61.9	−77.3	6.2	−81.0	346.2	−85.5	312.7	−19.7	112.2	−60.9	133.3
110	16	3.6	−57.9	79.2	−57.1	81.2	−75.0	19.4	−80.7	11.4	−87.1	74.0	−11.5	116.3	−52.6	143.4
120	24	2.6	−53.8	81.3	−53.4	82.2	−72.6	18.6	−78.4	16.5	−85.0	67.6	−7.7	116.8	−50.1	144.7
130	18	2.9	−50.6	80.0	−50.6	81.0	−70.0	12.7	−75.2	13.6	−83.8	47.9	−3.4	116.1	−49.1	145.3
140	10	6.1	−49.2	73.1	−49.0	74.9	−67.4	355.1	−70.4	356.7	−82.7	2.0	−0.3	114.8	−50.9	149.5
150	16	5.9	−55.2	65.0	−56.8	68.3	−68.7	327.2	−67.7	328.2	−81.9	301.3	−10.5	118.5	−54.6	166.9
160	14	6.0	−59.3	67.0	−61.6	69.4	−70.9	315.6	−68.2	316.2	−82.4	270.5	−14.6	124.0	−52.0	177.4
170	23	3.8	−61.2	77.6	−60.5	75.3	−73.9	306.8	−69.9	306.1	−84.2	223.8	−14.1	130.3	−46.3	180.8
180	26	3.6	−64.1	77.4	−63.5	76.0	−74.2	294.2	−68.8	296.7	−81.3	221.2	−16.7	131.7	−46.1	185.0
190	31	3.5	−71.8	68.8	−71.8	71.0	−70.9	265.5	−63.4	278.4	−73.0	227.0	−24.8	133.6	−47.0	197.0
200	35	3.2	−70.8	54.4	−71.5	58.8	−65.9	266.8	−59.2	282.3	−71.3	241.2	−27.4	129.2	−51.4	199.5
210	32	2.7	−66.9	43.6	−67.8	47.5	−60.8	271.6	−55.7	290.7	−69.8	257.2	−28.3	123.1	−56.9	199.6
220	29	2.0	−62.8	37.2	−64.6	40.9	−56.1	275.1	−53.6	300.5	−67.6	269.5	−28.7	117.5	−61.9	199.0
230	28	2.6	−58.6	40.0	−61.0	43.8	−54.7	282.4	−54.3	313.2	−68.7	281.0	−25.3	114.2	−64.2	190.8
240	35	3.6	−53.5	47.4	−55.2	49.9	−54.6	293.7	−55.6	330.5	−71.6	298.4	−19.0	112.4	−63.9	175.8
250	38	4.4	−49.6	55.4	−48.8	54.2	−55.5	304.5	−56.7	343.4	−74.4	317.6	−12.8	112.9	−60.4	164.7
260	26	5.4	−48.1	54.8	−47.1	52.8	−54.2	305.9	−55.3	344.8	−73.3	321.4	−11.9	111.6	−61.0	161.8
270	28	4.1	−43.2	50.3	−44.4	49.0	−48.4	307.4	−49.6	346.1	−67.8	326.9	−10.8	105.7	−64.5	151.7
280	57	2.4	−38.4	48.6	−39.0	48.0	−43.8	310.2	−44.9	348.9	−63.3	332.6	−8.4	101.2	−65.7	140.0
290	70	1.8	−37.2	45.8	−37.8	45.8	−41.6	308.7	−42.7	347.3	−61.0	330.6	−9.3	98.9	−67.7	136.4
300	39	2.3	−34.6	46.9	−34.9	46.1	−40.0	311.7	−41.1	350.3	−59.6	335.3	−6.9	97.6	−66.2	130.4
310	20	4.9	−30.5	49.9	−29.4	46.0	−38.0	317.3	−39.0	355.9	−57.6	343.7	−2.2	96.3	−62.6	123.3
320	10	8.6	−28.5	42.5	−25.9	38.7	−32.8	311.7	−34.7	1.1	−50.9	353.4	−9.3	82.0	−64.2	88.3

[a]Running mean path has a 20 Ma window length, with 10 Ma increments. N is number of input poles; A_{95} is 95% confidence circle. Abbreviations are APW, apparent polar wander; SAFR, South African; SAFR**, global APW path recalculated with time-dependent nondipole field (octupole) contributions [*Torsvik and Van der Voo*, 2002]; NAM, North American; EUR, European; SAC, South American Craton; IND, Indian; AUS, Australian; Lat, pole latitude; and Long, pole longitude.

segments of small circles if the Euler pole is kept constant at the same location. This is portrayed for a sphere with only two plates in Figure 7: Plate F is fixed, while Plate M moves and rotates around a low-latitude Euler pole in the Southern Hemisphere. Paleomagnetic poles determined from young rocks on Plate M should plot near the Earth's spin axis, whereas paleopoles derived from older rocks are situated on an APW path that represents a small circle around the Euler pole. If the moving plate (Plate M) is underlain by a hot spot, a chain of volcanic seamounts should also describe a small circle centered on the same Euler pole [cf. *Gordon et al.*, 1984; *Butler*, 1992].

[23] It is reasonable to assume that continents may drift around the pivotal axes of such unchanging Euler poles for, say, some tens of millions of years, and one can therefore attempt to construct APW paths by fitting small circles to paleomagnetic pole sequences; abrupt changes in the balance of forces driving and resisting plate motions should then be reflected in the APW paths as hairpins or cusps [*Irving and Park*, 1972; *Gordon et al.*, 1984]. Such analyses, however, must be undertaken in the reference frame of the plate in question, i.e., the plate (continent) on which the changing forces are acting. The analysis, referred to as the *paleomagnetic Euler pole method*, has commonly been performed on individual paleopoles from a single plate; however, below we test global running mean poles for small circle segments.

[24] In southern African coordinates (Figure 5a) we find seven small circle segments (300–250, 250–220, 220–190, 190–170, 170–130, 120–50, and 50–0 Ma) with root mean square (RMS) differences less than 1° (0.68° > RMS > 0.28°) for the last 300 Ma. Segment length varies between 30 and 70 Ma in duration, and small circle intersections coincide with segment boundaries except for those at 120–130 Ma and 50 Ma.

[25] *Gordon et al.* [1984] originally applied the concept of Euler pole rotations [*McKenzie and Parker*, 1967] to the Mesozoic APW path of Laurentia, and we therefore show a

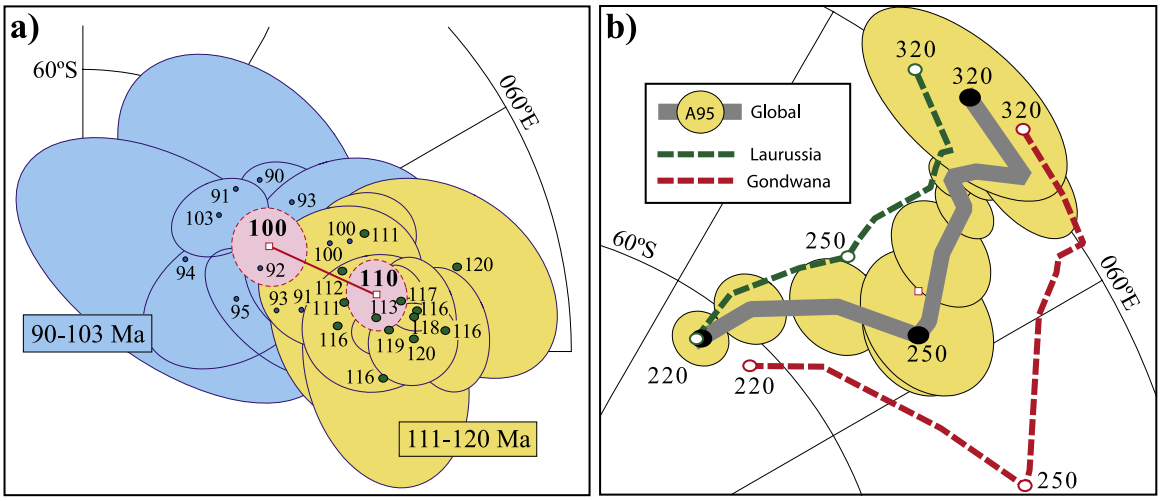

Figure 6. (a) Individual paleopoles with 95% confidence ovals, which were used to calculate the running mean path in Figure 5a for the segment with ages between 90 and 120 Ma. Two mean poles, at 100 and 110 Ma, were calculated with the running-mean approach and are shown with their A_{95} confidence circles in pink. (b) Comparison of the mean global path (gray) (the same as the global RM path in Figure 5a) and APW paths (in South African coordinates) derived from only Laurussian poles and only Gondwana poles between 220 and 320 Ma (see text and also Figure 4b).

detailed example of this method applied to North America. Figure 8a shows our global paleomagnetic running mean path in North American coordinates (Table 4). The three segments from 300 to 190 Ma are found to be similar to those of southern Africa and all other plates we have analyzed. This is to be expected because the continents moved together as parts of Pangea, with only minor predrift extension invoked prior to 190 Ma (Figure 3b). The Jurassic

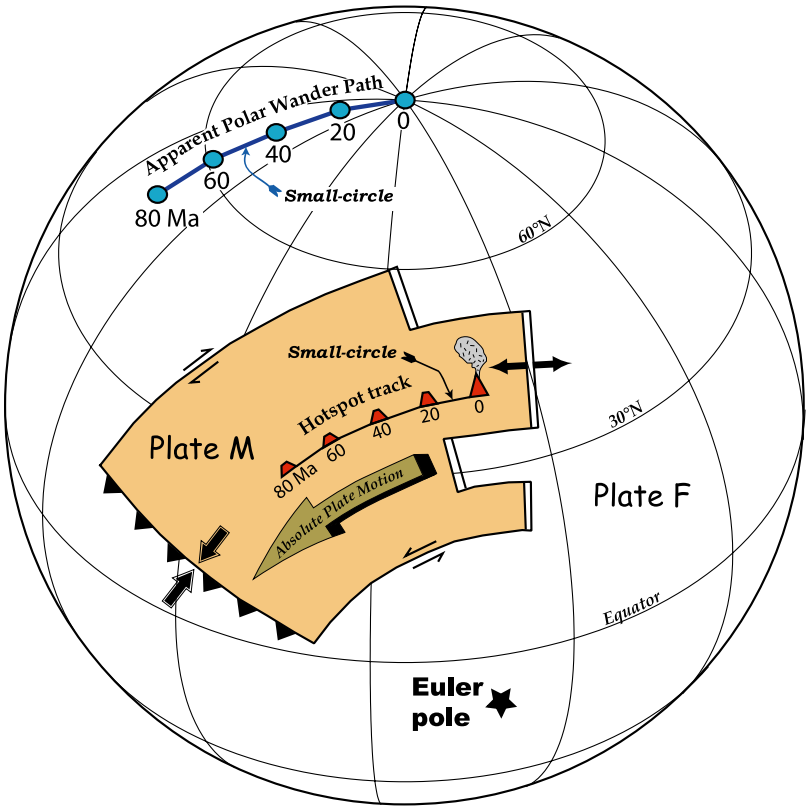

Figure 7. Apparent polar wander paths (in the absence of true polar wander) and hot spot tracks (if fixed to the mantle) represent small circle segments if the Euler pole is kept at the same location. In this example, Plate F is held fixed, and Plate M is moving around a constant Euler pole for 80 Ma. Compare text and *Gordon et al.* [1984].

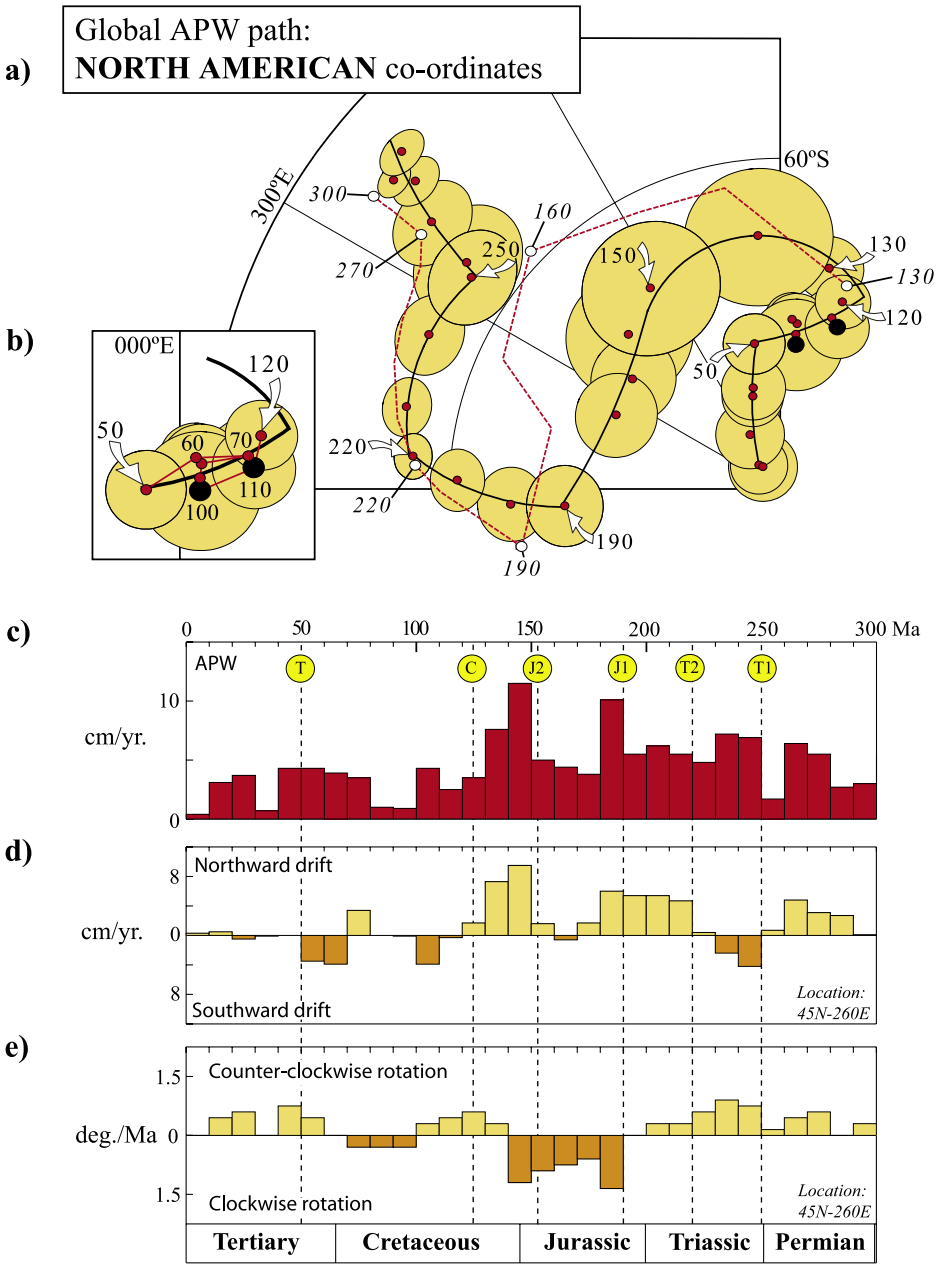

Figure 8. (a) Global apparent polar wander (APW) path, the same as in Figure 5a for the last 300 Ma, but shown in North American coordinates and fitted by seven small circle segments (black solid lines) discussed in the text. The red dashed line represents a running mean path exclusively based on North American poles. (b) Zoomed-in segment of the 50–120 Ma mean poles in order to examine poles during the North American Cretaceous stillstand. (c) Global APW rate in North American coordinates. Notice that the 110–100 Ma peak seen in southern African coordinates is not seen in North American coordinates, as in the latter it represents what has been called the "Cretaceous stillstand." Encircled letters, T1, T2, J1, J2, C, and T, are kinks or cusp intersections seen in Figure 8a, where they are marked by white arrows. Calculated (d) north–south drift and (e) angular rotation of North America based on the global running mean path for a specific location (45°N, 260°E).

section, however, differs substantially; the abrupt 170 Ma cusp seen for southern Africa (Figure 5a) is not present. Instead, there is a change in trajectory at 150 Ma where an intersection occurs between the 190–150 and the 150–130 Ma segments, but there is no trace of a distinct cusp. Similarly for southern Africa, we can fit small circles to the segments of 120–50 Ma (RMS = 0.81°) and 50–0 Ma (RMS = 0.23°), but the magnitude of Laurentian APW between 120 and 50 Ma (0.13°/Ma) is much less than that of southern Africa (0.45°/Ma). Our analysis is very different from any earlier paleomagnetic Euler pole analysis because we use global running mean poles and not just North American poles [see *Beck and Housen*, 2003], which show lower pole latitudes during the Middle-Late Jurassic than those predicted from a global model. We illustrate this in Figure 8a where the red dashed line represents a running

mean APW path, calculated exclusively from North American poles (Table 3). In this purely North American running mean path the global 250 Ma cusp has vanished (no longer influenced by Gondwana poles, see Figure 6b); the 220 Ma knickpoint is deteriorating (the segments being replaced by a single small circle from 270 to 190 Ma, RMS = 0.58°), whereas the 190, 120, and 50 Ma cusps are recognized, just as they were in the global running mean path. However, the Middle-Late Jurassic section differs markedly, with a knickpoint near 160 Ma, located at lower latitude. This is relevant to the debate about the reliability of the Laurentian Jurassic APW segment [e.g., *Ekstrand and Butler*, 1989; *Witte and Kent*, 1990; *Van Fossen and Kent*, 1990; *Van der Voo*, 1992; *Courtillot et al.*, 1994].

[26] On the basis of North American data alone and different pole selection criteria, *Beck and Housen* [2003] identified three small circle tracks (245–200, 200–160, and 160–125 Ma) and their two intersections (or cusps, both are pronounced), named J1 and J2 (following *Gordon et al.* [1984]). Using this nomenclature but on the basis of our global running mean path data, J1 (~190 Ma in our global analysis) occurs shortly before seafloor spreading began in the central Atlantic (rift to drift and the first real breakup phase of Pangea) and ~10 Ma after eruption of the Central Atlantic Magmatic Province. This J1 cusp at 190 Ma is associated with the second biggest burst in APW (Figure 8c), linked to a peak in angular rotation that initiated a prolonged period of clockwise rotation of ~50 Ma duration. Conversely, J2 (~150 Ma) coincides with local high seafloor spreading rates in the central Atlantic (Figure 3b) and occurs shortly before a northward velocity increase that coincides with the highest amount of APW for North America during the entire Mesozoic (Figures 8c and 8d). The Cretaceous is marked by decreasing APW, and the Cretaceous cusp at ~125 Ma (labeled C in Figures 8c–8e and Figure 3b) marks the beginning of the so-called North American Cretaceous stillstand that lasted until ~70 Ma as judged from our global running mean path (Figures 8b and 8c). This apparent stillstand ended when seafloor spreading (rift to drift) occurred in the Labrador Sea between North America and Greenland at ~67 Ma (see Table 1 and Figure 3b). The C cusp is associated with the onset of the highest seafloor spreading peak in the central Atlantic (Figure 3b). In an "absolute" sense we argue that the North American Cretaceous stillstand is only apparent and that it was caused by a dominating component of paleo-east-to-west drift (section 7). Finally, a Tertiary cusp (labeled T at 50 Ma in Figures 3b and 8c–8e) at around 50 Ma is linked to seafloor spreading in the North Atlantic and the accompanying *westward drift* of the North American plate. The older cusps (denoted T1 and T2 in Figures 8c–8e and 3b) will be discussed in section 8.2.

4. AFRICAN FIXED HOT SPOT FRAME

[27] *Wilson* [1963] first suggested that linear chains of seamounts and volcanoes, which display age progression, are caused by focused spots of melting in the mantle, termed "hot spots." *Morgan* [1971] proposed that hot spots may be caused by *mantle plumes* upwelling from the lower mantle, which in his model remain fixed relative to each other over geologically long periods of time ("fixed hot spot hypothesis"). During the past 40 years a multitude of marine geophysical data and isotope ages of seamounts from volcanic hot spot tracks have been collected, allowing reconstructions of plate motions relative to hot spots since the Cretaceous.

[28] Early attempts to reconstruct all major tectonic plates with respect to one collective set of hot spots (presumed fixed relative to each other) led to the realization that models constructed for Pacific plate motions over hot spots could not be reconciled with the motions over the hot spots in the African–Indian Ocean domain for the last 80 Ma [*Duncan*, 1981; *Morgan*, 1981]. Subsequently, evidence has accumulated that hot spots underlying the Pacific cannot have remained fixed relative to the Atlantic-Indian hot spots [*Molnar and Stock*, 1987; *Tarduno and Gee*, 1995; *Tarduno and Cottrell*, 1997; *DiVenere and Kent*, 1999; *Torsvik et al.*, 2002; *Tarduno et al.*, 2003]. However, hot spots within the Atlantic-Indian domain appear to have moved much less dramatically relative to each other. On the basis of this inference, *Müller et al.* [1993] used an interactive technique to derive a "best fit" model in a qualitative sense for motions of the major plates in the Atlantic-Indian domain relative to hot spot tracks with a clear age progression.

[29] Even though this model is widely used, it has some well-recognized shortcomings: the Late Tertiary portion of this model was not well constrained by radiometric ages because of the lack of published age dates for the post–30 Ma portion of most hot spot tracks. For reconstruction times predating 80 Ma, the only available hot spot tracks with a reasonably well known age progression in the Atlantic-Indian oceans are those of the New England seamount chain (linked to the Great Meteor hot spot) and the Walvis Ridge/Rio Grande Rise (linked to the Tristan hot spot, Figure 9), both in the Atlantic Ocean. Therefore, the absolute motion of the Indian, Australian, and Antarctic plates relative to the mantle has to be computed solely based on plate motion chains for these times. However, when the *Müller et al.* [1993] model was constructed, pre–80 Ma relative plate motions in the Indian Ocean were poorly known because of a lack of data in crucial areas, in particular offshore Antarctica in the Enderby Basin and south of the Kerguelen Plateau. This has recently improved as a sequence of Mesozoic magnetic anomalies was mapped and modeled in the Enderby Basin, starting at about 130 Ma [*Gaina et al.*, 2003, 2007]. The *Müller et al.* [1993] model was based on the assumption of post–120 Ma breakup between India and Madagascar, placing India too far north from 130 to about 90 Ma. Disagreements between the hot spot and paleomagnetic reference frames have been documented for India [*Müller et al.*, 1994; *Torsvik et al.*, 1998] and for Australia [*Idnurm*, 1985], suggesting either an incorrect relative plate motion model, relative motion between hot spots through time, or true polar wander or any combination of these three issues. As an example, paleopoles for India

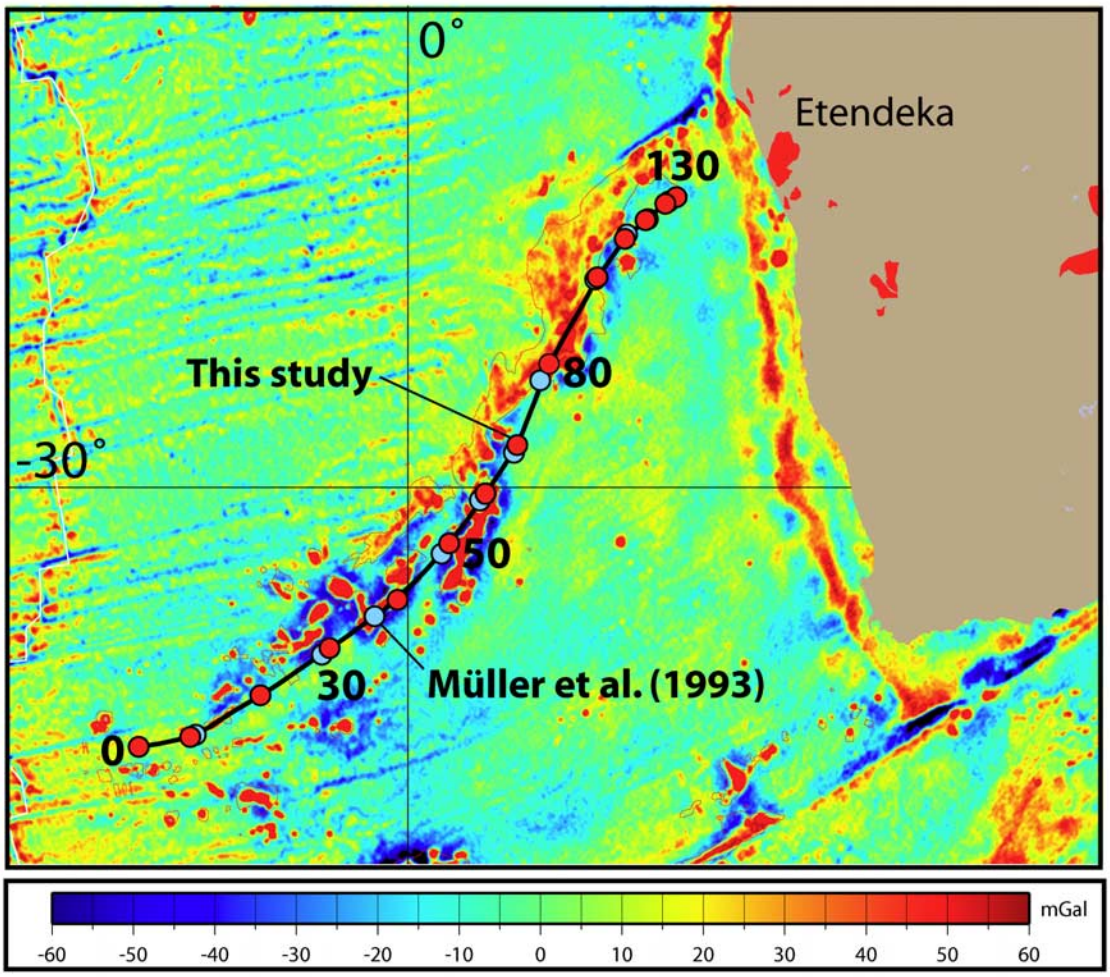

Figure 9. Walvis Ridge (linked to the Tristan hot spot at 38°S, 11°W) analyzed in a comparison of the African fixed hot spot model of *Müller et al.* [1993] (light blue circles) and the revised fixed hot spot model of this study (red circles), at 10 Ma interpolated intervals, showing that the differences are relatively small. The marine gravity data have been taken from *Sandwell and Smith* [1997].

from the Rajmahal Traps (Table 3) result in a *paleolatitude* of the traps at their time of formation (~116 Ma) at 47°S, whereas the *Müller et al.* [1993] model places them at about 40°S.

[30] A comparison of mid-Cretaceous (122–80 Ma) paleolatitudes of North America and Africa from paleomagnetic data with those from hot spot tracks [*Van Fossen and Kent*, 1992] provided evidence for an 11°–13° discrepancy, suggesting that Atlantic hot spots likely did not remain fixed relative to the Earth's spin axis before 80 Ma. With our more recent analyses using a different time interval and compared to the *Müller et al.* [1993] model, we find that the hot spots moved southward as much as 18° between 100 and 130 Ma [*Torsvik et al.*, 2002]. Others argue that this apparent southward movement was caused by true polar wander (TPW) [see *Prévot et al.*, 2000; *Camps et al.*, 2002; *Tarduno and Smirnov*, 2002].

[31] The *Müller et al.* [1993] plate motion model results in a relatively sharp turn in plate motion directions (e.g., of Australia and Antarctica) relative to the mantle at about 80 Ma, which originates from the bend between the New England seamount chain and the Corner seamounts at roughly 80 Ma in the central Atlantic. An equivalent bend in fracture zones is not found in either the Pacific or Indian oceans. Bends in hot spot tracks, which are not seen in relative motions of the plates involved, are likely because of time-varying velocities of local mantle (hot spot) motion relative to the mean mantle, as has been suggested as having caused the bend in the Hawaiian-Emperor chain [*Norton*, 1995; *Tarduno and Cottrell*, 1997]. It follows that the central Atlantic bend may be due to a slowdown in southward motion of the mantle underlying at least the Atlantic Ocean and its bordering continents at around 80 Ma and that fixed hot spot models therefore need to be replaced by models that take into account the motion of hot spots in a convecting mantle.

[32] The plate motion model used by *Müller et al.* [1993] was based on the timescales of *Berggren et al.* [1985] and *Kent and Gradstein* [1985]. In order to compare *Müller et al.* [1993] with more recent models for the purpose of this paper, we first need to translate it to more recent timescales [*Cande and Kent*, 1995; *Gradstein et al.*, 1994]. This

TABLE 5. Euler Rotations for South Africa in the Revised African Fixed Hot Spot Reference Frame Based on *Müller et al.* [1993] But Recalculated With New Timescales[a]

Age (Ma)	Euler Latitude	Euler Longitude	Euler Angle (deg)
10.9	59.3	328.4	−1.89
20.1	50.9	315.5	−4.36
33.1	40.3	317	−7.91
40.1	37.7	318.8	−9.65
47.9	32.8	319.2	−12.09
55.9	30.1	318.3	−13.89
67.7	26.4	319.1	−16.23
73.0	22.3	320.4	−17.8
79.1	18	321.1	−19.99
83.5	19	319.1	−21.53
89.9	19.4	318.1	−23.31
100.5	18.9	318.6	−25.35
111.1	17.7	320.5	−26.71
120.4	18.7	320.3	−27.37
130.7	16.7	322.5	−28.52

[a]See text. Note that the listed rotations here and in Tables 6–8 move the plate (here Africa) back from its present position to the past position at the given age not the other way round.

presents some difficulty, as *Müller et al.*'s [1993] model is based on a combination of relative and radiometric age dates, because samples from hot spot tracks are radiometrically dated, whereas the ages of plate reconstructions used in the model depended upon the ages of magnetic anomalies in the ocean basins, which, in turn, were dated with an older magnetic reversal timescale. For this paper we adjusted the ages given by *Müller et al.* [1993] to the *Cande and Kent* [1995] timescale for times back to chron 34 (83 Ma according to *Cande and Kent* [1995] and 83.5 Ma according to *Gradstein et al.* [1994]). Earlier ages were translated to the *Gradstein et al.* [1994] timescale. We assigned the age of 83.5 Ma to chron 34 because the *Gradstein et al.* [1994] timescale takes both Mesozoic and *Cenozoic* ages into account, thereby providing better constraints on chron 34 compared to the *Cande and Kent* [1995] timescale, which does not take into account ages older than chron 34. The difference between *Müller et al.* [1993] and our revised model, however, is small, and the largest differences (at ~40 and ~80 Ma) are less than 1° of arc when modeling the Tristan track (Figure 9). Exact input ages and Euler poles for the revised model are listed in Table 5, while interpolated Euler poles are shown in Figure 10 (African fixed hot spot) and listed in Table 6 (in the *African fixed hot spot* column). The pre–80 Ma portion of the fixed hot spot model, however, is notably weak, and our revised model still places India too far north at ~116 Ma. Therefore, we will argue in section 5 that the African *fixed hot spot frame* should be replaced by a *moving hot spot* frame.

5. MOVING HOT SPOT FRAMES

5.1. Introduction

[33] Testing models for motions between individual hot spots, or between regional groups of them, requires mantle convection models constrained by surface boundary conditions based on known plate motions. *Steinberger and O'Connell* [1997, 1998] pioneered the modeling of hot spot motions and TPW based on mantle flow models. Their technique to take differential motion of individual hot spots into account essentially uses a two-step approach: In the first step, large-scale mantle flow is computed based on mantle density heterogeneities derived from seismic tomography and viscosity structure as well as known plate motions. These flow computations yield certain predictions, e.g., geoid, and matching these with observations serves the goal of making the flow models as realistic as possible. Since the geoid is sensitive to relative viscosity variations with depth and not absolute viscosity values, flow is better constrained in direction than magnitude. The flow models are also used to advect density heterogeneities and in this manner extended backward in time. Since the rotation axis will remain aligned with the axis of maximum nonhydrostatic moment of inertia, which, in turn, is inferred from the predicted geoid, a prediction of TPW is a by-product of this first step. In a second step the motion of plume conduits embedded in large-scale flow, and thus the motion of hot spots, the points where the plume conduits reach the lithosphere, is computed. The conduit is assumed to be initially vertical, and motion of each conduit element is a superposition of advection and buoyant rising. Predicted hot spot motion is often similar to mantle flow at some depth, typically the upper part of the lower mantle. As for the flow models, directions of hot spot motion can be inferred with greater confidence than the amount of hot spot motion. In fact, observational limits on the speed of relative hot spot motion can help to constrain the speed of mantle flow. *Steinberger* [2000] extended this type of modeling to a larger number of hot spots and mantle flow schemes. This approach is most reliable for the Tertiary and has provided estimates for TPW and the motion of individual hot spots relative to each other for the last 68 Ma.

[34] When these models are extended back to the Cretaceous, however, pure backward advection of mantle density anomalies becomes increasingly unreliable [*Conrad and Gurnis*, 2003], as more of the past mantle temperature anomalies may have diffused away and therefore cannot be reconstructed by extrapolation. Other methods, such as variational data assimilation and adjoint methods [e.g., *Bunge et al.*, 2003; *Ismail-Zadeh et al.*, 2006], will be needed to reconstruct mantle density and flow further back in time. Nevertheless, hot spot motion can still be computed prior to 68 Ma but with additional uncertainty. Test runs for models from 120 Ma to the present, either including or excluding the advection of mantle density anomalies, have shown that there are many similarities between the two types of models. This indicates that meaningful predictions for relative hot spot motion can be made based on a simple mantle convection model, constrained by time-dependent plate motions and mantle density heterogeneities. This strategy was used by *O'Neill et al.* [2005] to model the motion of plumes relative to each other in a convecting mantle in the context of an "interactive inversion" strategy. *O'Neill et al.* [2005] explored the large parameter space inherent in these models to search for those mantle convec-

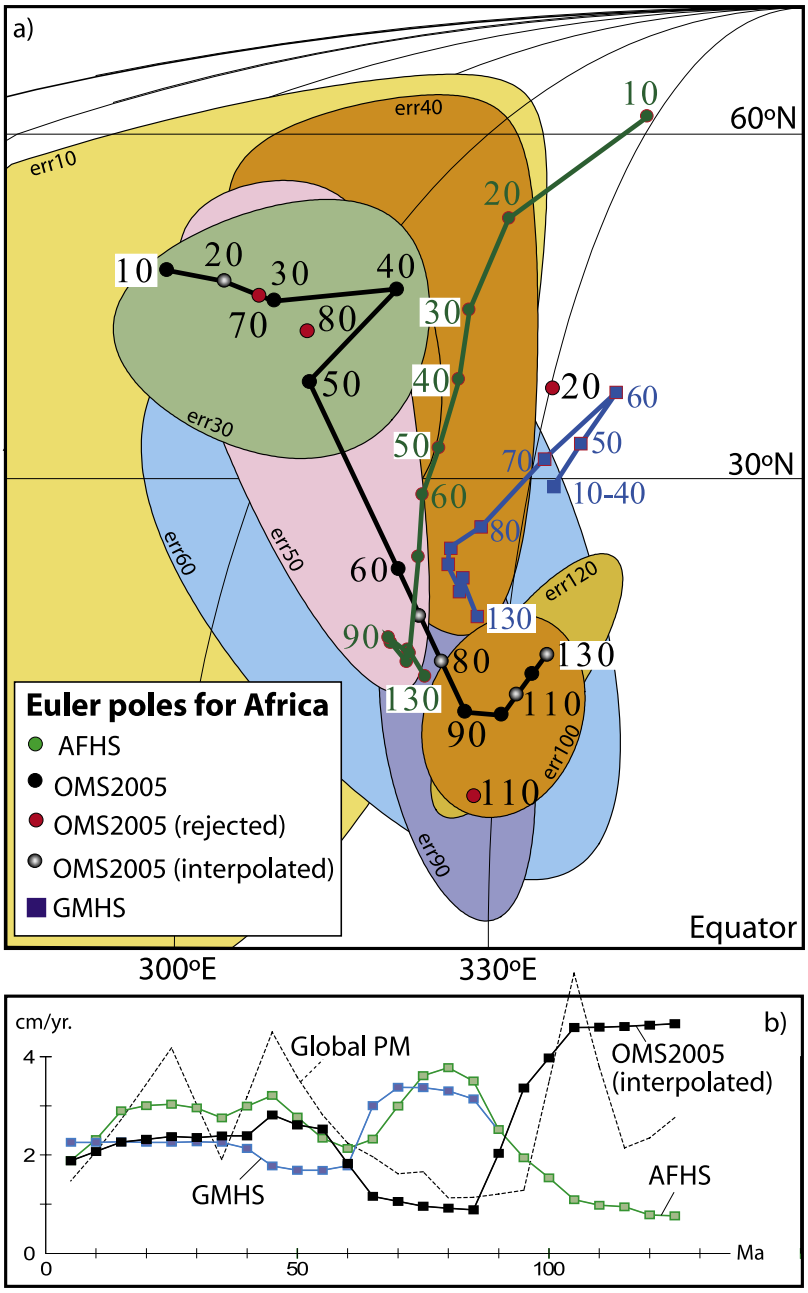

Figure 10. (a) Comparison of Euler poles for Africa (at 10 Ma intervals) (see Table 6) as derived for the African fixed hot spot (AFHS), African moving hot spot (OMS2005), and the global moving hot spot (GMHS) reference frames. The error ovals are derived using the OMS2005 approach [*O'Neill et al.*, 2005]. Considering errors in the other frames (not quantified here), most Euler poles do not statistically differ at the 95% confidence level. (b) Mean plate velocity for southern Africa as computed for each of the three different reference frames in Figure 10a as well as the global paleomagnetic running mean path of Figure 5a. Notice that the GMHS model becomes identical to AFHS prior to 83.5 Ma.

tion models that provide the best fit to observed hot spot tracks and their age progression, while minimizing the disagreements between model-based hot spot paleolatitudes and paleolatitudes from paleomagnetic data. Furthermore, *O'Neill et al.* [2005] adopted the *Hellinger* [1981] criteria of fit for deriving best fit absolute plate rotations based on track geometries, radiometric ages, and the moving locations of plumes in a convecting mantle to derive covariance matrices for absolute rotations of plates in the Indo-Atlantic domain for the last 120 Ma. While the original *Hellinger* [1981] method uses fracture zones and isochrons as two orthogonal data sets to determine relative plate motions, in the *O'Neill et al.* [2005] method, fracture zones are replaced by hot spot tracks, and "isochrons" are constructed based on age data along hot spot tracks. While fracture zones are the flow lines of relative plate motion, the geometry of hot spot tracks, corrected for computed hot spot motion, marks the flow lines of *absolute plate motion*. And while in the

TABLE 6. Euler Rotation Parameters for South Africa for Different Frames[a]

	African Fixed Hot Spot			African Moving Hot Spot			Global Moving Hot Spot			Paleomagnetic Frame[a]		Global Hybrid		
Age (Ma)	Lat	Long	Angle (deg)	Lat	Long	Angle (deg)	Lat	Long	Angle (deg)	Long	Angle (deg)	Lat	Long	Angle (deg)
0	90.0	0.0	0.0	90	0	0.0	90	0.0	0.0	56.0	2.2	90	0	0.0
5	76.2	328.4	−0.9	30.3	326.0	−1.0	29.4	332.5	−1.1	57.6	2.5	30.3	326.0	−1.0
10	62.1	328.4	−1.7	46.2	272.1	−1.9	29.4	332.5	−2.3	53.9	2.5	46.2	272.1	−1.9
15	55.6	321.8	−3.0	45.8	276.8	−3.0	29.4	332.5	−3.4	66.5	3.0	45.8	276.8	−3.0
20	50.9	315.5	−4.4	45.2	281.5	−4.0	29.4	332.5	−4.5	75.5	4.7	45.2	281.5	−4.0
25	46.8	316.2	−5.7	44.4	286.0	−5.1	29.4	332.5	−5.6	84.1	6.8	44.4	286.0	−5.1
30	42.8	316.7	−7.1	43.5	290.3	−6.1	29.4	332.5	−6.8	95.8	7.9	43.5	290.3	−6.1
35	39.6	317.5	−8.4	44.3	297.9	−7.1	29.4	332.5	−7.9	98.8	8.7	44.3	297.9	−7.1
40	37.2	318.8	−9.9	44.6	305.7	−8.1	29.4	332.5	−9.0	107.5	9.2	44.6	305.7	−8.1
45	34.7	319.1	−11.2	40.8	303.3	−9.2	30.0	332.9	−10.0	110.9	10.3	40.8	303.3	−9.2
50	32.1	319.0	−12.5	37.0	301.1	−10.3	32.4	334.7	−10.6	111.6	13.2	37.0	301.1	−10.3
55	30.4	318.4	−13.7	30.6	310.1	−11.4	34.5	336.4	−11.3	115.7	13.9	30.6	310.1	−11.4
60	28.9	318.6	−14.6	23.7	317.9	−12.5	36.4	337.9	−11.9	123.5	15.7	23.7	317.9	−12.5
65	27.3	318.9	−15.6	22.2	319.4	−13.2	34.3	334.7	−12.9	127.8	17.5	22.2	319.4	−13.2
70	24.6	319.7	−16.9	20.7	320.9	−13.8	31.4	330.9	−14.1	137.2	17.5	20.7	320.9	−13.8
75	20.8	320.7	−18.6	19.2	322.4	−14.4	28.9	328.0	−15.4	140.3	19.2	19.2	322.4	−14.4
80	18.3	320.5	−20.5	17.7	323.9	−15.0	26.7	325.6	−16.7	138.1	19.3	17.7	323.9	−15.0
85	19.1	318.9	−21.9	16.2	325.3	−15.6	25.4	323.7	−18.1	142.9	19.6	16.2	325.3	−15.6
90	19.4	318.1	−23.4	14.6	326.7	−16.2	25.3	322.5	−19.4	144.7	20.5	14.6	326.7	−16.2
95	19.1	318.4	−24.4	14.5	328.6	−18.2	24.7	322.7	−20.4	144.3	20.8	14.5	328.6	−18.2
100	19.0	318.6	−25.2	14.4	330.4	−20.1	24.1	322.8	−21.3	150.8	22.3	14.4	330.4	−20.1
105	18.4	319.4	−25.9	15.1	331.1	−22.5	23.2	323.7	−22.0	160.2	26.9	10.3	337.7	−27.3
110	17.8	320.3	−26.6	15.7	331.7	−24.9	22.4	324.6	−22.6	169.2	32.1	8.6	346.7	−32.5
115	18.2	320.4	−27.0	16.4	332.4	−27.3	22.6	324.7	−23.1	170.3	35.6	7.7	347.8	−35.9
120	18.6	320.3	−27.3	17.0	333.0	−29.7	23.2	324.5	−23.4	171.3	36.2	7.6	348.8	−36.5
125	17.8	321.3	−27.9	17.5	333.5	−32.1	22.0	325.6	−24.0	172.1	37.5	7.3	349.6	−37.8
130	16.9	322.3	−28.4	18.0	334.0	−34.6	20.7	326.7	−24.5	170.0	39.4	6.9	347.5	−39.7
135										172.6	42.1	6.5	350.1	−42.4
140										163.1	40.8	6.7	340.6	−41.1
145										155.2	38.1	7.2	332.7	−38.5
150										155.0	34.8	7.9	332.5	−35.1
155										155.0	33.2	8.3	332.5	−33.6
160										157.0	30.7	9.0	334.5	−31.1
165										159.5	32.5	8.5	337.0	−32.8
170										167.6	28.8	9.6	345.1	−29.3
175										167.8	27.7	10.0	345.3	−28.1
180										167.4	25.9	10.7	344.9	−26.4
185										168.4	21.6	12.9	345.9	−22.2
190										158.8	18.2	15.2	336.3	−18.9
195										147.9	17.8	15.6	325.4	−18.5
200										144.4	19.2	14.4	321.9	−19.9
205										137.4	20.7	13.4	314.9	−21.3
210										133.6	23.1	12.0	311.1	−23.7
215										129.9	26.4	10.5	307.4	−26.9
220										127.2	27.2	10.2	304.7	−27.7
225										128.0	29.4	9.4	305.5	−29.8
230										130.0	31.4	8.8	307.5	−31.8
235										133.6	35.3	7.8	311.1	−35.6
240										137.4	36.5	7.5	314.9	−36.8
245										143.1	39.6	6.9	320.6	−39.9
250										145.4	40.4	6.8	322.9	−40.7
255										145.6	41.8	6.5	323.1	−42.1
260										144.8	41.9	6.5	322.3	−42.2
265										141.6	47.1	5.7	319.1	−47.4
270										140.3	46.8	5.8	317.8	−47.1
275										138.2	51.1	5.2	315.7	−51.4
280										138.6	51.6	5.2	316.1	−51.9
285										136.5	51.8	5.1	314.0	−52.0
290										135.8	52.8	5.0	313.3	−53.0
295										136.8	53.5	4.9	314.3	−53.7
300										136.9	55.4	4.8	314.4	−55.6
305										138.9	56.3	4.7	316.4	−56.5
310										139.9	59.5	4.4	317.4	−59.7
315										138.9	60.8	4.3	316.4	−61.0
320										132.5	61.6	4.2	310.0	−61.7

[a]Latitude is zero for all ages.

Hellinger [1981] method isochrons on two plates are matched, *O'Neill et al.* [2005] match instead their constructed isochrons with the modeled hot spot location at the respective times. In practical terms, application of the method is not straightforward; for example, age data along hot spot tracks are often sparse and may not always represent passing of the plate over the hot spot. Posterosional volcanism may still occur millions of years afterward; furthermore, both age data and track geometry may be influenced by plume-ridge interaction, i.e., flow of material from a plume to a nearby spreading ridge. These and other limitations and difficulties are discussed further by *O'Neill et al.* [2005].

[35] While the two-step approach was motivated by computational limitations, a fully dynamic computation of hot spot motion in large-scale flow is now feasible where not only the influence of the mantle on the plume is taken into account but also the effect of the plume on its surrounding medium [*Tan et al.*, 2006]. Also, large-scale mantle flow models are becoming more realistic because of inclusion of temperature-dependent and strain rate–dependent viscosities [e.g., *Becker*, 2006; *Čadek and Fleitout*, 2003] and further constraints, in particular related to seismic anisotropy [e.g., *Becker et al.*, 2006; *Behn et al.*, 2004].

5.2. African Moving Hot Spot Frame

[36] In the method of *O'Neill et al.* [2005] each reconstruction is statistically independent from reconstructions at younger or older ages. This implies that smoothness is not imposed on the set of absolute rotations derived for a given plate. Therefore, a bias in the data used for a given reconstruction may result in a best fit rotation that is implausible in terms of plate kinematics. For instance, a consecutive set of rotation poles may lie approximately on a small circle, with one rotation being situated far off this small circle path, indicating that it is an outlier if there are no independent data supporting a plate kinematic event, such as a change in plate motion direction, or rate, at this time. The set of 12 Euler poles initially derived by *O'Neill et al.* [2005] (OMS2005), from 10 to 120 Ma in 10 Ma intervals (black circles in Figure 10a), includes four rotations that are geologically or kinematically implausible, i.e., for 20, 70, 80, and 110 Ma (red circles in Figure 10a, OMS2005 rejected). These rotations are removed from this model and have been replaced by interpolated rotations (gray open circles in Figure 10a, OMS2005 interpolated, see Table 6), whereas the 130 Ma rotation pole has been extrapolated. The resulting Euler pole path can be approximated by three small circle segments from 0 to 40, 40–90, and 90–120 Ma; however, considering how large the errors are, none of these bends in the Euler pole path are significant. The largest difference between the *O'Neill et al.* [2005] and our revised African fixed hot spot Euler pole paths is in the 0–60 Ma portions of the paths (Figure 10a, green versus black symbols). However, different age progressions in the Euler angles (Table 6) lead to very different mean plate velocities for southern Africa during the Cretaceous. The African fixed hot spot Euler rotations result in increasing plate velocities in the Late Cretaceous (peaking at ~80 Ma), whereas *O'Neill et al.* [2005] predicts decreasing velocities and shows a minimum where the African fixed hot spot frame predicts the highest velocities. The running mean paleomagnetic frame (thin dashed line in Figure 10b) shows gross similarities with *O'Neill et al.* [2005] (solid black line) for the interval ~110–50 Ma, but the two Tertiary peaks in the running mean path are not seen in any of the other reference frames (Figure 10b).

5.3. Global Moving Hot Spot Frame

[37] The construction of the global reference frame of *Steinberger et al.* [2004] was motivated by the long known fact that when a plate motion chain through West Antarctica is used (Figure 3a, model 1), the fixed hot spot African reference frame does not agree with a fixed hot spot Pacific reference frame. If African absolute plate motions are chosen such that hot spot tracks in the African hemisphere are fitted to observations, while hot spot tracks in the Pacific hemisphere are predicted through the plate motion chain, then the Pacific track predictions do not agree with the observations there: in particular, the predicted Hawaiian track is somewhat south of the observed track between Hawaii and the Hawaiian-Emperor bend at ~50 Ma [*Sharp and Clague*, 2006]. Not only does the predicted track not have as pronounced a bend, it is also substantially farther southwest than the Emperor Chain for times prior to the bend. *Wessel et al.* [2006] and *Whittaker et al.* [2007] recognized that the recent redating of bend initiation to ~50 Ma correlates the bend with major tectonic events from around the Pacific, such as South Pacific triple-junction reorganization at chrons 22–21 (49.7–47.9 Ma), Farallon-Pacific fracture zone bends at chrons 24–21 (53.3–47.9 Ma), and the direction change and proposed halt of Pacific-Kula plate spreading at chrons 24–20/19 (53.3–43.8/41.5 Ma) as well as a major reorganization of relative plate motions between Australia and Antarctica. Nevertheless, some regard the bend to be partly or fully caused by hot spot motion [e.g., *Molnar and Stock*, 1987; *Norton*, 1995], whereas *Whittaker et al.* [2007] argued subduction of the Pacific-Izanagi spreading ridge and subsequent Marianas/Tonga-Kermadec subduction initiation may have been the ultimate causes of these events. If a Pacific absolute plate motion model is chosen such that hot spot tracks in the Pacific hemisphere are fitted and hot spot tracks in the African hemisphere are predicted through the plate motion chain, the predicted tracks do not agree with the observed tracks either.

[38] *Steinberger et al.* [2004] found that their geodynamical model typically predicts a southward motion of the Hawaiian hot spot with velocities up to a few centimeters per year, contrasting with slower motion for other hot spots. Thus, their model of hot spot motion, in combination with the plate motion chain that connects Africa and the Pacific via East Antarctica and Marie Byrd Land (West Antarctica), allowed a fit of hot spot tracks globally for times after the age of the Hawaiian-Emperor bend. In this model, no motion occurs between East and West Antarctica prior to 43.8 Ma (model 1, Figure 3a). For times prior to 43.8 Ma an

east-west misfit between predicted and observed Hawaiian hot spot track remains. Consequently, *Steinberger et al.* [2004] explored the use of an alternative plate motion chain that connects Africa and the Pacific via East Antarctica, Australia, and the Lord Howe Rise for times 46.3 Ma and older (model 2, Figure 3a). Between the Lord Howe Rise and the Pacific the 46.3 Ma rotation was adopted from *Sutherland* [1995], and no motion was assumed prior to 46.3 Ma. For times 43.8 Ma and younger the plate motion chain through East Antarctica and Marie Byrd Land is maintained, and rotations are interpolated between 43.8 and 46.3 Ma. The two plate motion chains differ: for the southwest Pacific plate motion chain, model 2 predicts intra-Antarctic motion prior to 43.8 Ma, with extension in the Ross Sea area, whereas model 1 does not involve movements between East and West Antarctica before 43.8 Ma. With the plate motion chain of model 2, *Steinberger et al.* [2004] were able to achieve an acceptable fit to hot spot tracks globally back to about 65 Ma. Prior to that a misfit between predicted and observed Hawaiian track remains, which can only be eliminated if further motions between the Lord Howe Rise and the Pacific are introduced.

[39] With this plate motion chain an ''absolute'' African plate motion is determined such that the fit to the Hawaiian, Louisville, Reunion, and Tristan hot spot tracks is optimized in a least squares sense: locations and ages of dated samples, as compiled from various sources, are included in this optimization. For the Reunion track, samples from both the Indian and African plates were used, with sample locations of the Reunion track on the Indian plate rotated using India-Africa finite (Euler) rotations for their respective ages. For the Tristan track (Figure 11), only samples from the African plate were used. For the Hawaiian and Louisville tracks (Figures 11 and 12), sample locations were rotated using Pacific-Africa finite (Euler) rotation parameters for their respective ages. This means that, in essence, the tracks are computed as if all four hot spots remained located underneath the African plate all the time. For these four tracks rotated onto the African plate, the best fitting African plate motion is determined with a least squares method as described by *Steinberger* [2000]. Parameters used in the optimization include African plate rotation rates and latitude-longitude pairs of stage rotation poles for three time intervals (0–43.8, 43.8–61.2, and 61.2–83.5 Ma). For each time interval a constant rotation rate is assumed. This method requires that appropriate uncertainties in both space and time are assigned to each data point. Uniform spatial uncertainties of 50 km have been assigned to each data point, whereas in terms of temporal uncertainty, published age errors have been used for the Hawaii and Louisville tracks. For the Tristan and Reunion tracks a uniform temporal uncertainty of 0.5 Ma is assigned. Present hot spot locations are entered assuming a 50 km spatial uncertainty but zero time uncertainty. Each track is given equal weight in the optimization. With these choices for the uncertainties the resulting best fitting African plate motion gives a better visual agreement between predicted and observed tracks than when using published age errors.

[40] The African plate motion in the ''global moving hot spot'' framework (Table 7), as determined here, differs from that of *Steinberger et al.* [2004] because relative plate motions are slightly different. Furthermore, optimized African plate rotations are determined here for the three time intervals mentioned above. These interval boundaries are chosen to occur at those times when relative plate rotations also change. The direction change at ~60–62 Ma corresponds to a change in the age progression along the Louisville chain [*Koppers et al.*, 2004]. The ''fixed hot spot'' tracks in Figure 12 show that without further smoothing the inferred Pacific plate motions exhibit short-term fluctuations that bear no apparent relation to actual plate motions, because they do not correspond to features in the observed hot spot tracks and would, at any rate, be difficult to explain dynamically. We therefore introduce a few ''ad hoc'' changes in order to obtain a smoother, and hence likely more realistic, Pacific plate motion history. First, we assign the total rotation between Lord Howe Rise and Pacific plate from *Sutherland* [1995] (latitude of 49.8°, longitude of −1.6°, and angle of 49.0°) to 51.7 Ma instead of 46.3 Ma. At 43.8 Ma the rotation (latitude of 50.1°, longitude of −2.7°, and angle of 47.7°) is inferred through the South Pacific plate motion chain, and for the interval between 43.8 and 51.7 Ma it is interpolated. We note that there is no evidence for deformation between Lord Howe Rise and the Pacific as early as 51.7 Ma; however, the required deformation is quite small and presumably within error bounds (R. Sutherland, personal communication, 2005) because the two rotations above are quite similar. This change simplifies Pacific plate motion around the time of the Hawaiian-Emperor bend and removes a kink (shown in green in Figure 12) in the Hawaiian track. Inferred Pacific plate motion around the time of the bend (43.8–51.7 Ma) is quite slow (~2.5–3 cm/a). (See Figure 11 (bottom); note that this diagram shows mean plate speeds; the actual point speed

Figure 11. (top) Optimum match between predicted (blue, tic-marked lines) and observed hot spot tracks (seen as gravity anomalies) allowing the establishment of a global moving hot spot reference frame. Tristan and Hawaii hot spot motion are the same as given by *Steinberger et al.* [2004]. Tracks are computed with the ''global hot spot'' SAFR plate motions (Table 1) and with smoothed PAC-SAFR relative plate motions as described in the text. Dated samples with ages (in Ma) are also shown; data sources are given by *Steinberger et al.* [2004]. (bottom) Mean plate velocity for PAC (10 Ma bin histogram and actual data, shown as a red curve, from Table 8) in the global moving hot spot frame after 83.5 Ma and the fixed hot spot frame of *Duncan and Clague* [1985] before that. Plate speeds plotted upward/downward indicate northward/southward plate motion, but total plate speed, not just north-south component, is shown. The actual plate kinematic model (APKIM) of *Drewes* [1999] predicts a mean plate velocity of 6.9 ± 0.9 cm/a and compares well with estimated velocities for the Pacific plate over the last 40 Ma.

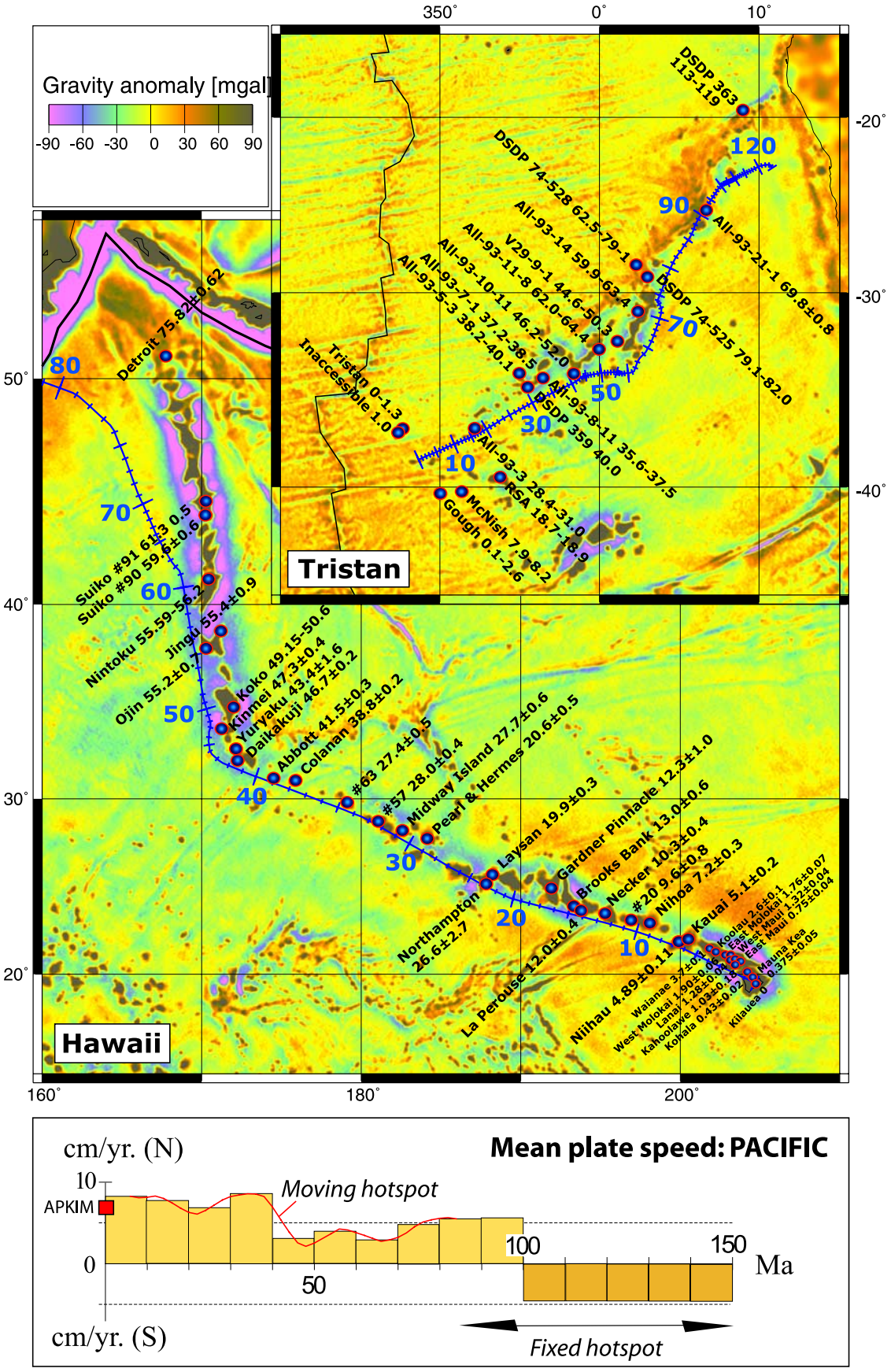
Gravity anomaly [mgal]
-90 -60 -30 0 30 60 90
350˚
0˚
10˚
-20˚
-30˚
-40˚
50˚
40˚
30˚
20˚
160˚
180˚
200˚
Tristan
Hawaii
DSDP 363 113-119
DSDP 74-528 62.5-79-1
All-93-14 59.9-63.4
V29-9-1 44.6-50.3
All-93-11-8 62.0-64.4
All-93-10-11 46.2-52.0
All-93-7-1 37.2-38.5
All-93-5-3 38.2-40.1
DSDP 74-525 79.1-82.0
All-93-21-1 69.8±0.8
All-93-8-11 35.6-37.5
DSDP 359 40.0
All-93-3 28.4-31.0
RSA 18.7-18.9
McNish 7.9-8.2
Gough 0.1-2.6
Tristan 0-1.3
Inaccessible 1.0
Detroit 75.8±0.62
Suiko #91 61-63 0.5
Suiko #90 59.5±0.6
Nintoku 55.59-56.2
Jingu 55.4±0.9
Ojin 55.2±0.7
Koko 49.15-50.6
Kinmei 47.3±0.4
Yuryaku 43.4±1.6
Daikakuji 46.7±0.2
Abbott 41.5±0.3
Colahan 38.8±0.2
#63 27.4±0.5
#57 28.0±0.4
Midway Island 27.7±0.6
Pearl & Hermes 20.6±0.5
Laysan 19.9±0.3
Gardner Pinnacle 12.3±1.0
Brooks Bank 13.0±0.6
Necker 10.3±0.4
#20 9.6±0.8
Nihoa 7.2±0.3
Kauai 5.1±0.2
Koolau 2.6±0.1
East Molokai 1.76±0.07
West Molokai 1.32±0.04
East Maui 0.75±0.04
Mauna Kea 0.375±0.05
Kilauea 0
Niihau 4.89±0.11
Waianae 3.7±0.1
Lanai 1.28±0.04
Kahoolawe 1.03±0.13
Kohala 0.43±0.02
La Perouse 12.0±0.4
Northampton 26.6±2.7
120
90
70
50
30
10
80
70
60
50
40
30
20
10
cm/yr. (N)
Mean plate speed: PACIFIC
10
APKIM
0
Moving hotspot
50
100
150
Ma
cm/yr. (S)
Fixed hotspot

Figure 11

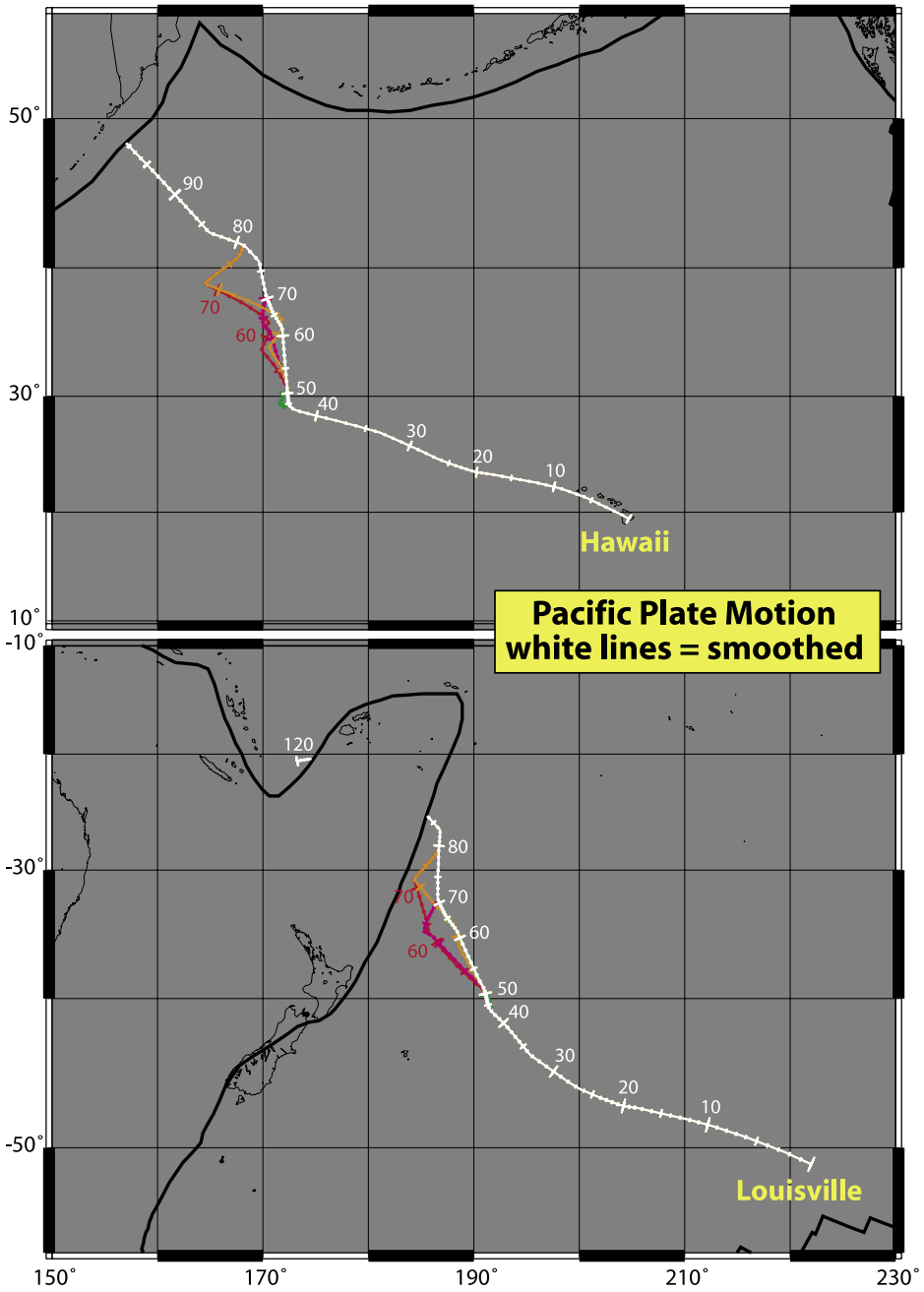

Figure 12. Predicted tracks for the Hawaii and Louisville hot spots. In contrast to Figure 11, hot spots are held fixed here in order to separate the effect of Pacific plate motion over time on computed tracks. South Africa plate motions are the same as in Figure 11. Tic marks are placed every 1 Ma. White lines are computed with the smoothed relative plate rotations as in Figure 11. For the green lines the transition between two plate motion chains has not been smoothed. For the red lines the East Antarctica versus South Africa and Australia versus Lord Howe Rise rotations have not been smoothed. For the orange line, only the East Antarctica versus South Africa rotation has been smoothed. For the violet line, only the Australia versus Lord Howe Rise rotation has been smoothed.

around the bend is as low as 1.7 cm/a between 50 and 45 Ma.) Second, from among the Lord Howe Rise versus Australian rotations for magnetic anomalies 24o (o indicates older end of the anomaly, 53.3 Ma) through 33y (y indicates younger end of the anomaly, 73.6 Ma) we only use anomaly 27o (61.2 Ma) and 30y (65.5 Ma). These rotation poles are at intermediate locations and for times when the spreading direction appears to have changed from rotating clockwise to counterclockwise and back to clockwise. This change leads to a considerably smoother and more realistic Hawaiian track in Figure 12 (violet versus red or white versus orange). Short-term changes in Tasman Sea spreading may hence be related to deformation within continental crust bounding the Tasman Sea (especially in New Zealand) and not to short-term changes of Australian or Pacific plate motion. Third, we exclude the southern Africa versus East

TABLE 7. Euler Rotations for South Africa in the Global Moving Hot Spot Frame Using Plate Chain Model 2[a]

Age (Ma)	Euler Latitude	Euler Longitude	Euler Angle (deg)
43.8	29.42	332.50	−9.87
61.2	36.80	338.26	−12.08
83.5	25.37	324.12	−17.66
89.9	25.28	322.53	−19.42
100.5	24.04	322.77	−21.43
111.1	22.18	324.78	−22.77
120.4	23.20	324.52	−23.47
130.7	20.51	326.82	−24.58

[a]See Figure 2. Euler poles older than 83.5 Ma are simple added poles using the African fixed hot spot frame (Table 5). Note that this global frame is smoothed (see relative poles not used from Table 1).

Antarctica rotation at the time of anomaly 28 (63.1 Ma), which was published by *Bernard et al.* [2005]. This rotation is quite different from the rotations before and after and also differs from that of *Royer et al.* [1988]. At the location of Hawaii the omission of this 63.1 Ma rotation does not change Pacific plate motion by much, but it removes a kink (white versus violet track in Figure 12) in the Louisville track. Figure 11 shows the ''moving hot spot'' Tristan and Hawaiian tracks for the smoothed model (white tracks in Figure 12). Back to about 75 Ma, the difference between predicted and observed Hawaii-Emperor hot spot tracks is now less than about 300 km (Figure 11) and thus is probably less than uncertainties arising from the oceanic part of the plate motion chain [e.g., *Cande et al.*, 1995]. In the model without smoothing, larger misfits occur before ~65 Ma. We also note that with southward motion of the Hawaiian hot spot between about 75 and 50 Ma of a few degrees more than modeled here, the entire Emperor chain could be fit in terms of geometry, ages, and paleolatitudes [*Tarduno et al.*, 2003]. However, a more detailed analysis and justification of the plate motion chain modifications will be required before fully endorsing this smoothed model.

[41] *Steinberger et al.* [2004] were concerned with the past 83.5 Ma, and they made no attempt to determine a reference frame that considered hot spot motion before chron 34, primarily because the Hawaii-Emperor track does not extend further back in time but also because the uncertainties are much larger for older times. Here, we extend the reference frame to times before 83.5 Ma, using rotation rates relative to hot spots that are assumed fixed. The extension is done separately for the Pacific [*Duncan and Clague*, 1985] and Africa (section 4). The predicted plate velocity for southern Africa in this frame is quite similar to that in the African moving hot spot framework [*O'Neill et al.*, 2005] until ~40 Ma; for 60–83.5 Ma it is similar to the velocity in the African fixed hot spot frame, and prior to 83.5 Ma it is by construction identical (Figure 10b).

6. COMPARISON OF RECONSTRUCTION FRAMES

[42] The largest differences between the revised African fixed hot spot, the African moving hot spot, and the global moving hot spot reference frames are seen in the Tertiary portions of the Euler pole ''paths'' (Figure 10). However, error ellipses calculated from the *O'Neill et al.* [2005] model demonstrate that the majority of the computed Euler poles are not statistically different at the 95% confidence level.

[43] In order to compare hot spot and paleomagnetic frames the most common approach is to rotate the mean paleomagnetic poles using the hot spot reconstruction parameters. This is commonly referred to as plotting paleomagnetic poles in a hot spot frame [see *Torsvik et al.*, 2002]. In the absence of errors in the rotation parameters, TPW, or other complexities all paleomagnetic poles should plot at 90°N in the hot spot frame. Here, we use a novel approach and compare uncertainty ellipses computed by Hellinger's method (centered at 90°N, with blue ovals in Figure 13) for the African moving hot spot frame, with errors of the mean paleomagnetic poles (A_{95}, pink circles in Figure 13). Although there are marked differences between the rotated global mean paleomagnetic poles and the rotation axis for the Early Cretaceous (>100 Ma), it is evident that for Tertiary times (with only one exception at ~50 Ma) one cannot argue for systematic and statistically significant differences; the average great circle distance is only 3.7° ± 1.6° (Figure 13b). At 100 Ma, great circle distance is still only 3°, whereas the two data sets are significantly different at 120 Ma (there are no Hellinger error ellipses for 110 and 130 Ma).

[44] Compared with the African fixed hot spot frame, the African moving hot spot frame is an important improvement because it significantly reduces the difference between the global mean paleomagnetic poles and the rotation axis for the Early Cretaceous (compare red and black lines in Figure 13b, showing a reduction of the great circle distance at 120 Ma from ~17° to ~10.5°), although this remains a statistically significant difference at the 95% confidence level. We note, though, that there are substantial uncertainties in modeled mantle flow and hot spot motion this far back in time, and these uncertainties are not included in the assessment of significance. This is important and has implications for some recent and passionate debates concerning Cretaceous TPW [*Prévot et al.*, 2000; *Tarduno and Smirnov*, 2001, 2002; *Camps et al.*, 2002; *Torsvik et al.*, 2002].

[45] Given plate rotations and boundaries, it is also possible to compute mean lithospheric rotations in different reference frames. For example, combining our global moving hot spot reference frame with NUVEL [*DeMets et al.*, 1990] plate boundaries, we find for the past 5 Ma an average of 0.165°/Ma around an axis 40°S, 38°E. Such a net rotation of the lithosphere relative to the deeper mantle can result from lateral viscosity variations [*Ricard et al.*, 1991; *O'Connell et al.*, 1991]. We regard this net rotation mainly to be a consequence of the large size of the Pacific plate. The Pacific plate is subducting in the west and north and has ridges in the east and, as an entirely oceanic plate, is presumably underlain by a low-viscosity asthenosphere. This qualitatively explains its direction and relatively fast speed of motion (Figure 12). Because of its large size the Pacific plate dominates the mean lithospheric rotation. Hence the axis of mean lithospheric rotation that we find

is similar to the axis of Pacific plate rotation (Table 8). More quantitatively, *Becker* [2006] finds predicted mean lithospheric rotation for a number of geodynamic models to be similar to our result both in direction and magnitude. Since its rotation pole is in the Southern Hemisphere, this net rotation contains a "westward drift" component. As this westward drift is mainly caused by motion of the Pacific plate, it does not imply westward motion of other plates, such as the African plate. Other authors [e.g., *Doglioni et al.*, 2005] have proposed different reference frames and obtain much higher values of westward drift.

7. TOWARD A HYBRID REFERENCE FRAME

[46] Hot spot frames are arguably not very robust prior to 100 Ma, but at 100 Ma the African moving hot spot frame accommodates the global mean paleomagnetic pole location

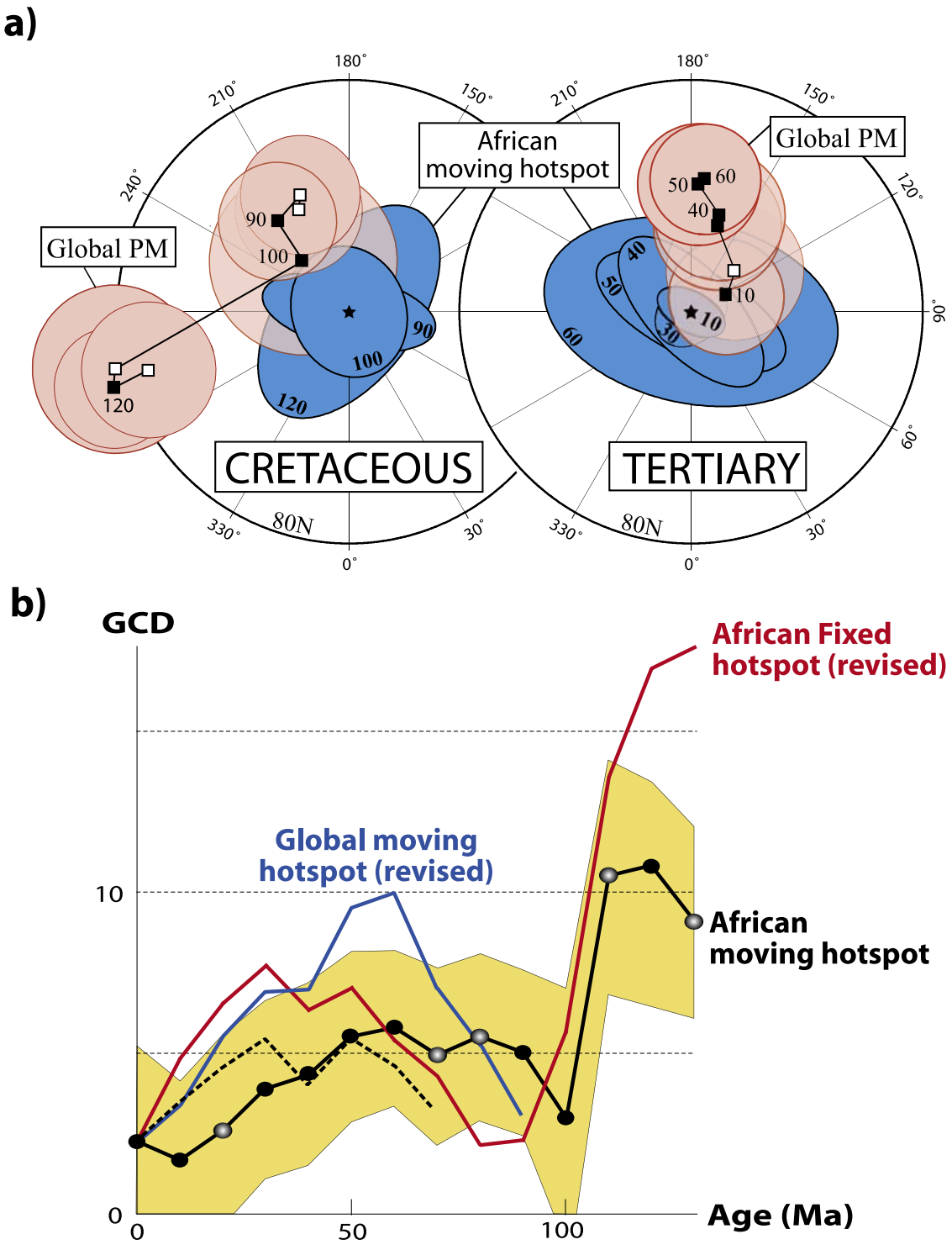

Figure 13

TABLE 8. Euler Rotations for the Pacific in the Global Moving Hot Spot Frame[a]

Age (Ma)	Euler Latitude	Euler Longitude	Euler Angle (deg)
0.8	63.99	278.79	0.62
2.6	67.06	284.52	2.24
5.9	68.07	279.70	5.03
8.9	67.57	270.79	7.30
9.9	67.57	268.72	8.07
12.3	69.54	269.06	9.95
17.4	72.94	269.96	14.33
20.2	73.75	268.91	15.69
24.1	73.80	269.60	17.69
26.6	73.53	270.12	19.61
28.3	73.11	271.68	20.89
33.2	72.28	277.44	24.77
33.5	72.23	278.04	25.02
40.1	71.85	294.31	30.14
42.5	71.55	297.19	31.77
43.8	71.17	297.46	32.38
51.7	68.98	295.61	32.88
53.3	67.79	293.53	33.28
61.2	62.23	287.34	35.39
65.6	61.17	286.45	36.64
71.1	59.74	285.78	37.77
73.6	58.19	286.27	38.39
75.5	57.04	286.60	38.88
76.3	56.46	286.76	39.07
79.0	55.13	288.92	40.33
83.5	54.29	293.73	42.39
100.0	51.65	289.54	51.46
150.0	64.18	299.96	71.13

[a]We use plate chain model 2; see text and Figure 3a. Euler poles older than 83.5 Ma use pre–83.5 Ma stage rotations from the fixed hot spot frame of *Duncan and Clague* [1985]. This frame is also smoothed (see relative poles not used from Table 1). Note that Tables 7 and 8 are only global up to 83.5 Ma; before that, Africa and the Pacific are treated separately and not related through any of the relative rotations listed in Tables 1 and 2.

pretty well, so that the position of Africa in Figure 14 is very similar in the moving hot spot frames and in the global paleomagnetic frame; only the fixed hot spot frame produces a different position of Africa. Since it is permissible in paleomagnetic reconstructions to adjust the longitude, we correct for a 5° longitude offset observed at 100 Ma between the African moving hot spot (blue in Figure 14a) and the global paleomagnetic reference frames. In this way we produce the first global *hybrid reference frame* where we combine the paleomagnetic frame for 320–110 Ma with the moving hot spot frame for ≤100 Ma (Table 6).

[47] Predicted mean plate speeds for southern Africa based on this hybrid model average to 3.5 ± 1.5 cm/a (Figure 15b), compatible with "normal" plate tectonic speeds, but there is a velocity spike when the two reference frames are merged (6.7 cm/a at 105 ± 5 Ma). This mid-Cretaceous velocity peak is not an artifact of frame change since the peak is seen independently in the paleomagnetic frame (Figure 10b) and predicted by maximum APW at this time (section 3 and Figure 5e). A change in velocity but with different magnitude (~6–13 cm/a) is found for all continental plates at this time. For Africa this event is related to a strong counterclockwise rotation (Figure 15c) with a rotation pole near the equator (Figure 16) that could be interpreted as TPW at 100–110 Ma. This issue has been addressed by *Steinberger and Torsvik* [2008] who further developed the reference frames of this paper by considering TPW.

[48] One other significant issue emerges from our consideration of the paleomagnetic data rotated into the hybrid moving hot spot framework: the well-known Cretaceous stillstand in Laurentia's APW path (Figure 8b). We argue that this pattern represents pure east-to-west drift of the continent. Note that the North American plate motion history is very different in the hybrid model from the fixed hot spot model. The latter predicts northward drift during the Cretaceous, with a major bend at 80 Ma [see also *Torsvik et al.*, 2001a]. In contrast, the hybrid moving hot spot model predicts a strong component of westward drift. The sharp change in "absolute" motion at ~50 Ma for both North America and Europe (Figure 17) is linked to the opening of the NE Atlantic.

8. HYBRID FRAME: EXAMPLES

8.1. Linking Plate Motions to the Deep Earth

[49] An "absolute" plate motion reference frame is essential in order to explore potential links between plate tectonics and processes operating in the deep Earth. Volcanism unrelated to plate boundaries or rifts has been widely attributed to mantle plumes from the deep mantle. *Torsvik et al.* [2006] explored the spatial relation between *large igneous provinces* and the deep mantle by comparing large igneous provinces (LIPs) at eruption time with shear wave

Figure 13. (a) Comparison of the African moving hot spot (with blue error ovals, centered on the rotation axis) and mean paleomagnetic north poles ("global PM" with pink A_{95}) rotated using the Euler poles from the African moving hot spot frame. Thus, deviation from +90° latitude (i.e., the rotation axis) can reflect errors in the hot spot frame and its rotation parameters, erroneous paleomagnetic poles, or true polar wander. For the Tertiary and Late Cretaceous (≤100 Ma), only the 50 Ma pole is significantly different from the moving hot spot frame at 95% confidence; for all other times the blue ovals and pink error circles (A_{95}) overlap. For the Early Cretaceous the 120 Ma pole and probably also the 110 and 130 Ma poles (which have no error ovals in the moving hot spot frame) are significantly different. Black squares denote times where there are corresponding errors in the hot spot frame; open squares denote where they are absent. (b) Differences (expressed as the great circle distance (GCD) in degrees) between the rotated paleomagnetic poles (as in Figure 13a) and the different fixed or moving hot spot frames. Shaded yellow outline represents the uncertainty in the paleomagnetic mean poles (A_{95}) when compared with the African moving hot spot framework. Grey circles are for interpolated or extrapolated Euler poles. The global moving hotpot frame is only shown for times after 83.5 Ma because the older part is based on the African fixed hot spot frame. For comparison we also show a previous African moving hot spot frame of *Steinberger* [2000] (mantle model 2, dashed black line). The latter frame is applicable only after 68 Ma.

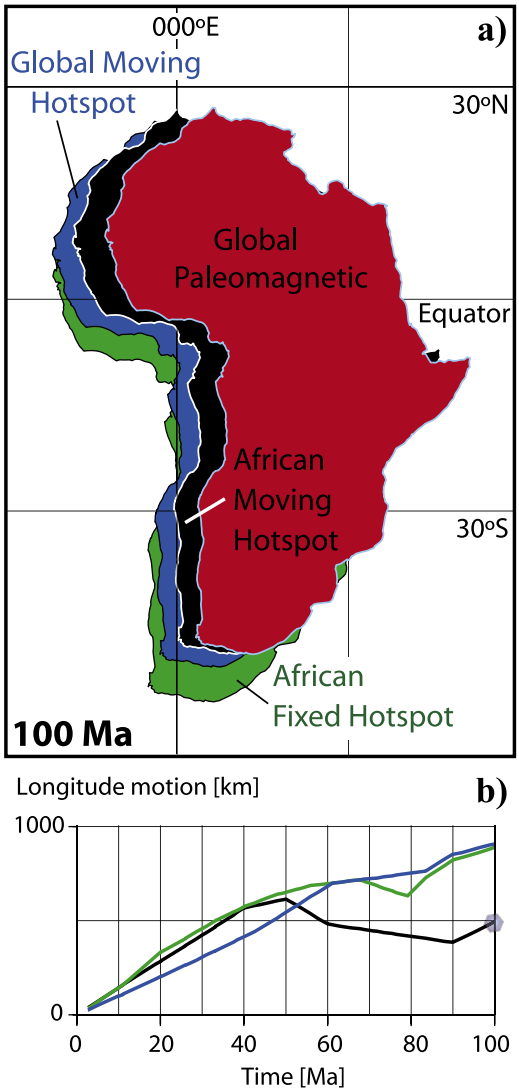

Figure 14. (a) Reconstruction of Africa at 100 Ma using all four reference frames discussed in the text. The continent's positions show longitude offsets from the global paleomagnetic framework, varying from 5° (African moving hot spot) to 9° (African fixed hot spot). African fixed hot spot predicts significantly more southerly latitudes for Africa than all other frames. (b) Cumulative eastward component of motion for Africa since 100 Ma as predicted from the African moving hot spot (black line), African fixed hot spot (green line), and global moving hot spot (blue line) reference frames. Mean motion is computed from a 1° × 1° grid for the continental area of Africa.

anomalies near the *core-mantle boundary*. Testing all reference frames developed in this study, *Torsvik et al.* [2006] showed that practically all LIPs erupted at the Earth's surface for the past 200 Ma lay over the margins of the African or the Pacific *large low-shear-velocity provinces* [*Garnero et al.*, 2007] at the core-mantle boundary. In Figure 18 we reconstruct 17 LIPs in the Indo-Atlantic realm using our new hybrid frame and extending the analysis to the last 300 Ma. In situ locations of approximated LIP centers (small annotated circles with gray or light blue background colors) are scattered and show no obvious link to the African large low-velocity provinces (LLSVPs). Conversely, correcting for plate motion since eruption time (large annotated circles with white or blue background colors) demonstrates a strong spatial link between LIP surface eruption locations and the deep mantle; that is, all LIPs in the Indo-Atlantic realm (except the North Atlantic Igneous Province, GI in Figure 18) project radially downward onto or close to the margin of the African LLSVP.

[50] Eruption locations vertically above the edge of one or other of the Earth's two LLSVPs at the core-mantle boundary characterize nearly all the LIPs erupted since 300 Ma [*Burke and Torsvik*, 2004; *Torsvik et al.*, 2006, 2008], and for that reason it can be argued that LIPs are derived from deep mantle plumes. The hybrid plate reference frame used to reconstruct LIPs in Figure 18 is based on the African moving hot spot (0–100 Ma) and the paleomagnetic (>100 Ma) frame. The paleomagnetic frame is based on keeping the African plate fixed in longitude before 100 Ma but adjusted 5° in longitude. Despite the "zero" Africa assumption (sections 3.1 and 9), paleomagnetically reconstructed LIPs show a close correspondence with today's deep mantle shear wave tomography. However, longitude is strictly not known, and all LIPs older than 100 Ma can therefore theoretically be adjusted in an E–W sense and with different magnitudes since LIPs have different ages.

8.2. Pangea

[51] An important growth phase occurred for Pangea during the Late Carboniferous when Laurussia, Gondwana, and intervening terranes collided. Although some continental elements were probably still adjusting their positions along the Pangea perimeter, Pangea had essentially accomplished its "all-Earth" mission by Early Permian time. However, the China blocks were still only loosely connected with Pangea within the Paleo-Tethys Ocean [*Torsvik*, 2003; *Torsvik and Cocks*, 2004]. Our 250 Ma Pangea reconstruction is shown overlaying the present-day shear wave velocity anomalies near the core-mantle boundary in Figure 19, assuming that lower mantle heterogeneities have remained stationary for hundreds of millions of years [*Burke and Torsvik*, 2004; *Torsvik et al.*, 2006] (see section 8.1). Our global hybrid model predicts that the bulk of Pangea was centered above the present-day African low-velocity region and that the peri-Pangea subduction rim was essentially located above high-velocity zones, feeding the subduction graveyards in the deepest mantle [*Richards and Engebretson*, 1992].

[52] Africa was at the heart of Pangea, and two clear 90° kinks (near cusps at 220 and 190 Ma) in the southern African APW path (Figure 15a) may relate to changes in the balance of plate motion forces that are representative of Pangea breakup. A third cusp-like feature (at ~250 Ma, see Figure 15a (labeled T1 in Figure 15b)) should be considered with some care since there is a major discordance between Laurussian and Gondwana poles of this age (Figure 6b); moreover, increased smoothing treatments of the APW path diminish the impact of this feature (Figures 5c and 5d).

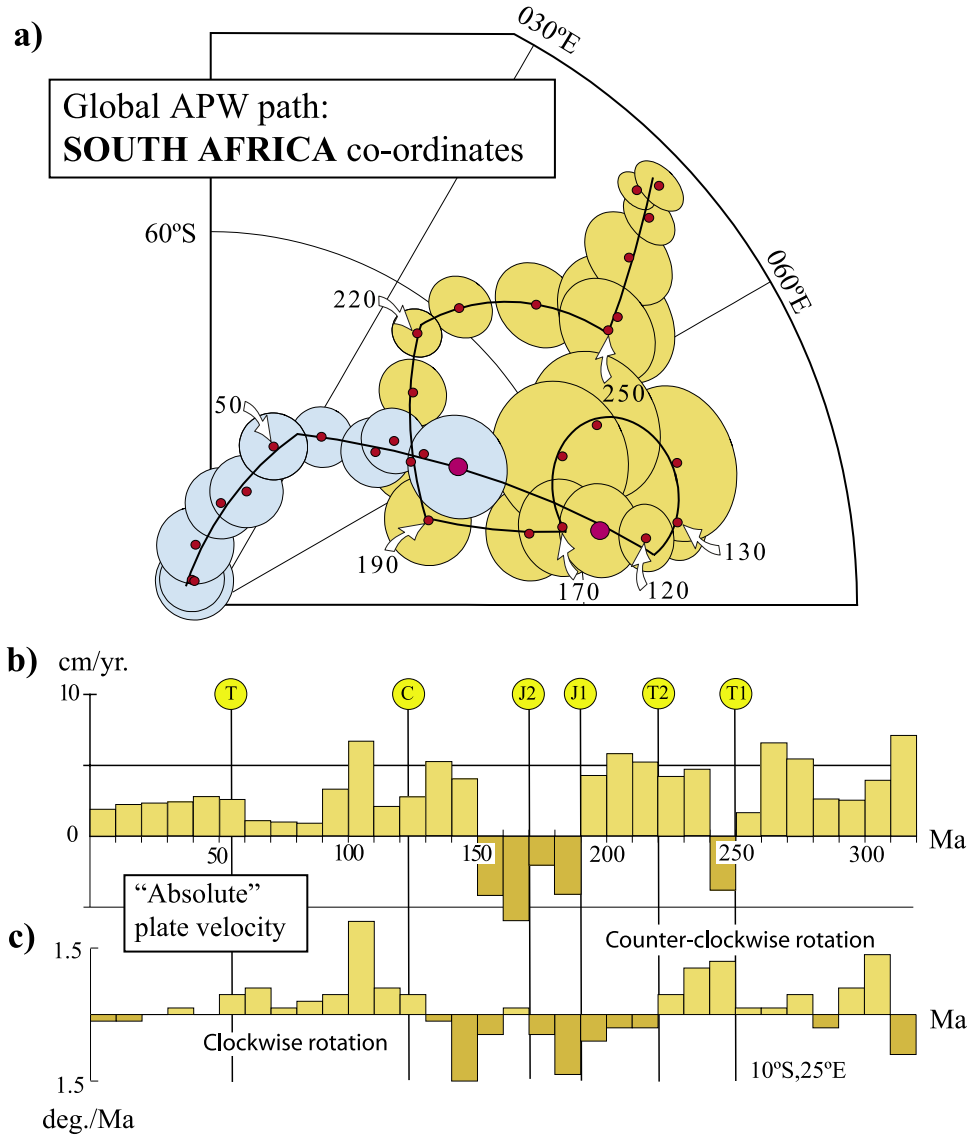

Figure 15. (a) Global paleomagnetic apparent polar wander path, calculated with the running mean method, for southern Africa as in Figure 5a (last 300 Ma) but with fitted small circle segments. Note that in our hybrid model the 100 Ma and younger segment of the running mean path (A_{95} shown in blue) has been replaced with the African moving hot spot frame. (b) Mean plate velocity for southern Africa (averaged over 10 Ma windows) separated into times of net northward and southward drift and based on the hybrid model. However, total plate speed, not just north-south component, is shown. (c) Angular rotation for a point location (10°S, 25°E) in southern Africa based on the hybrid frame. Note that the velocity peak between 100 and 110 Ma is caused by a peak in the rotation history of southern Africa. In Figures 15b and 15c, kink or cusp intersections are labeled T1, T2, J1, J2, C, and T, and these are shown as white arrows in Figure 15a.

[53] Considerable counterclockwise rotation of Pangea and terrane displacements in the *Tethys* occur during the Permo-Triassic. An additional, unresolved question is whether Siberia was fully joined to Pangea before the eruption of the Siberian Traps (~251 Ma). The Neo-Tethys probably began opening at ~265 Ma [*Stampfli and Borel*, 2002] and was well developed as a young oceanic basin by 250 Ma (black area in Figure 19), while Paleo-Tethyan oceanic crust was being subducted beneath Eurasia. All other subduction zones inferred for the Permo-Triassic have Panthalassa's oceanic lithosphere plunging down under Pangea's perimeter. In other words, no *subducting slabs* are known to have been attached to Pangea's continental lithosphere with outward directed plunges.

[54] It is possible and natural to link the 220 and 190 APW kinks (Figure 15a) to the destruction of much of the Paleo-Tethys and the transition from rift to drift in the central Atlantic (Pangea breakup). Paleo-Tethys had essentially vanished by the Early Norian (~220 Ma) [*Stampfli and Borel*, 2002] as a result of the collisions of many peri-Gondwana terranes, collectively called *Cimmeria* [*Şengör and Natal'in*, 1996], with Eurasia. The Early Jurassic

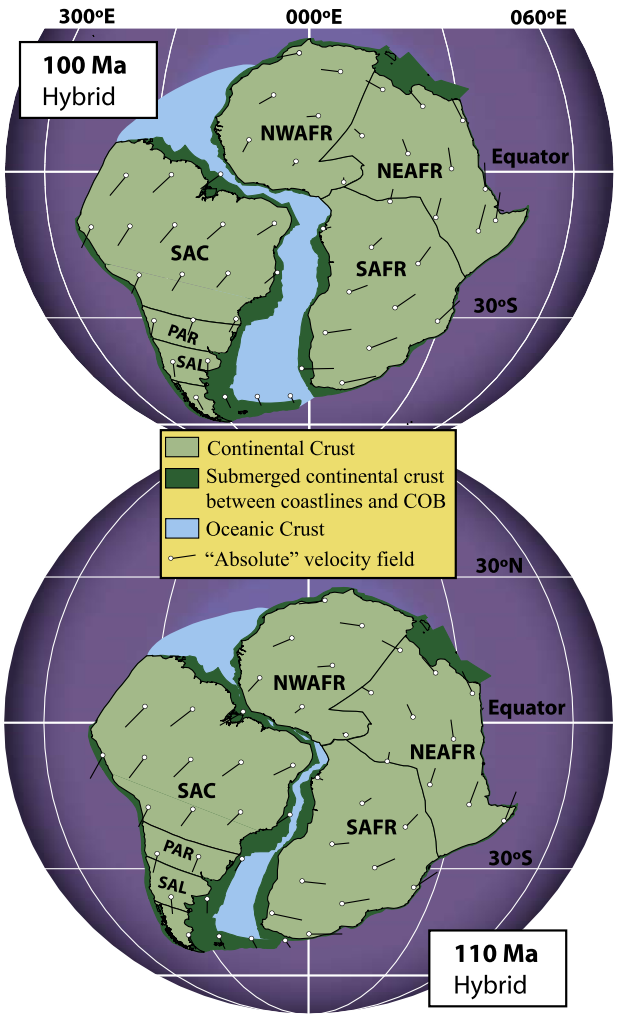

Figure 16. "Absolute" reconstructions of Africa and South America at 100 and 110 Ma with time-averaged velocity fields 95–105 and 105–115 Ma, respectively, as calculated from the hybrid model. Africa/South America are rotating counterclockwise around a pole located near the equator (at the intra-African triple junction), which could be linked to a short period of TPW. The rotation is associated with opening of the South Atlantic. Full oceanic separation between South America and Africa was achieved at 100 Ma. During this time interval (100–110 Ma), North America and Europe had a strong component of westward drift, whereas, for example, East Antarctica and Australia were dominated by eastward drift. Abbreviations are as in Figure 3. Revised South Atlantic continent-ocean boundaries (COBs) have been taken from *Torsvik et al.* [2004]. Other features are after *Müller et al.* [1997].

witnessed the assembly of the Asian part of Pangea but simultaneously saw the breakup of Pangea in the central Atlantic; both of these events reflect changes in plate motion forces that are likely candidates to explain the 190 Ma cusp.

[55] Cause and effect can be enigmatic, and APW tracks, separated by cusps or kinks, can also be the result of TPW, best represented by a rotation around an equatorial axis close to a supercontinental center of mass [*Steinberger and Torsvik*, 2008]. For the late Paleozoic–early Mesozoic during which Pangea was a supercontinental entity drifting as a whole with respect to the rotation axis, TPW has been speculatively proposed by *Marcano et al.* [1999]. The white arrows in Figure 19 illustrate the generalized velocity field that remained in effect for much of the counterclockwise rotation episode of about 0.4°/Ma that lasted until the latest Triassic. In order to establish TPW with any certainty one needs the velocity field for oceans as well as continents, and in the Permo-Triassic this is obviously not possible because the plate configurations inside the *Panthalassa* ocean clearly remain unknown. However, *Marcano et al.* [1999] argued that if the Panthalassa hemisphere participated in the same rotation shown by the Pangea hemisphere, no evidence for significant convergence between Panthalassa and Pangea at the latter's leading edge should exist. Examining the regional geology along the Siberian-Baltic-Laurentian Arctic margins, they found that evidence for convergence in the 295–205 Ma interval was rather scant and therefore concluded that slow TPW (~ 4 cm/a) for this interval could not be ruled out.

9. CONCLUSIONS AND FUTURE CHALLENGES

[56] On the basis of revised plate motion chains we have recomputed and compared four different plate reference frames for Africa (paleomagnetic, African fixed hot spot, African moving hot spot, and global moving hot spot). We find that the African moving hot spot frame compares most favorably with the global paleomagnetic frame; considering the uncertainties in both reference frames, they are essentially identical for the last 100 Ma. For older times the moving hot spot frame is uncertain because simple backward advection is increasingly inappropriate for reconstructing past mantle density anomalies. Given the magnitude of the error limits in both mantle and paleomagnetic reference frames, it is premature to conclude true polar wander from their differences except for the Early Cretaceous (130–110 Ma). With respect to the African moving hot spot frame the mean paleomagnetic poles for 110–130 Ma show a discrepancy of approximately 10°. Mantle models are arguably not very robust before 100 Ma, but 10° is a considerable reduction when compared to the use of the African fixed hot spot frame where the discrepancy is ~18°. The fixed hot spot frame should no longer be used.

[57] The African moving hot spot frame is modeled back to 130 Ma. The "global" moving hot spot frame (incorporating the Pacific realm) is valid only back to 83.5 Ma; prior to this time it is extended by using rotation relative to assumed fixed hot spots. Our smoothed global moving hot spot frame produces a more realistic Pacific plate motion history, in which the difference between predicted and observed Hawaiian hot spot tracks is probably less than uncertainties arising from the plate motion chain for the last 75 Ma. Since the African moving hot spot and global paleomagnetic frames are exclusively based on data from the Indo-Atlantic realm, we decided to merge these two frames in our hybrid model.

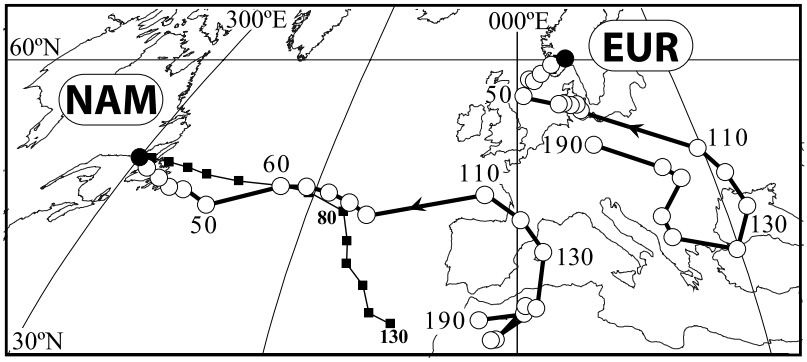

Figure 17. Examples of the drift history for selected locations in North America (NAM) (50°N, 300°E) and Europe (EUR) (60°N, 10°E) for the last 190 Ma. Our hybrid model (thick black lines with circles) is in one case compared with the revised African fixed hot spot model for NAM (thin lines with squares).

[58] We have constructed the first hybrid "absolute" reference frame model for the last 320 Ma: we use the African moving hot spot frame for the last 100 Ma and then the global paleomagnetic frame adjusted 5° in longitude to smooth the frame transition. All hot spot–based "absolute" plate motion models (Figure 14) result in minimal longitudinal motion of Africa (compared to most other plates), thus confirming the lack of significant longitudinal motion inferred from consideration of plate driving forces (section 3.1). It is less certain whether the "zero-longitudinal motion" approximation for Africa, corrected for the longitudinal motion of Africa during the past 100 Ma (Figure 14), holds before Pangea broke up. On the one hand, *Forsyth and Uyeda* [1975] showed that plates move faster when there are *subducted slabs* attached and that the larger the continental area on a plate is, the slower it tends to move. With little or no subducting slabs attached (section 8.2) and a very large continental area, Pangea is expected to have moved slowly. On the other hand, average N–S velocities derived from our *global paleomagnetic path* are as high as 3.6 ± 2.1 cm/a (320–180 Ma) for a central Pangea location in NW Africa. Nevertheless, in the absence of arguments for better reference points, we regard zero longitudinal average motion of Pangea as the best possible assumption.

[59] The hybrid model is a step forward to quantifying plate kinematics and the time-dependent plate velocity field and is essential for providing surface boundary constraints for mantle convection models and testing the relationship between surface magmatism and deep Earth processes, with the caveat that motions based on the paleomagnetic frame may also contain contributions due to TPW [*Steinberger and Torsvik*, 2008]. Both the fact that plumes only seem to arise from the edges of the large low-shear-velocity provinces (LLSVPs) and that these LLSVPs appear not to have moved by much over the past 300 Ma (section 8.1) provide a challenge to be explained in future mantle dynamic models. At face value the mantle flow models used to compute advection of plumes would also predict changes of LLSVPs with time. Just as the observational limits of relative hot spot motion provide a constraint on the speed of mantle flow and hence on mantle viscosity, the observational limits on LLSVP motion and deformation will also allow us to gain information regarding their rheology.

[60] Our hybrid reference system is yet to be tested using forward mantle convection models, which "stir" the mantle

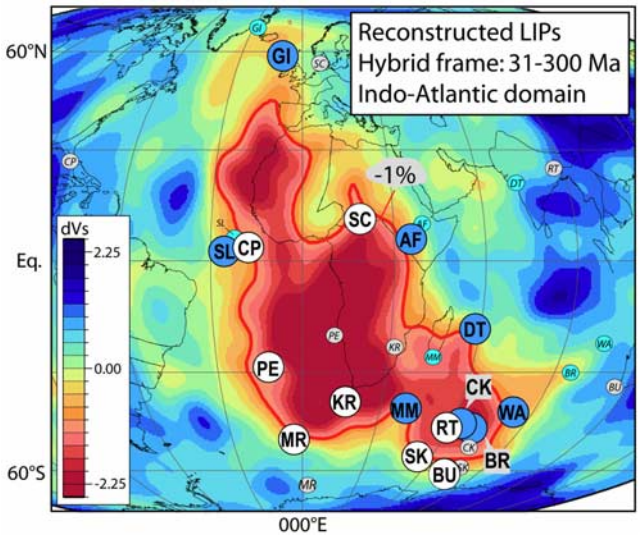

Figure 18. In situ (small annotated circles with gray and light blue background) and reconstructed Indo-Atlantic LIP eruption sites (large annotated circles) draped on the SMEAN shear wave velocity anomaly model for 2800 km (red is slow; blue is fast) [*Becker and Boschi*, 2002]. Reconstructions are based on the hybrid reference frame that is based on the African moving hot spot (large blue circles) and the paleomagnetic reference frame adjusted 5° in longitude (large white circles). LIP abbreviations (with mean eruption ages in Ma) are AF, Afar flood basalt (31); GI, Greenland/Iceland (54); DT, Deccan Traps (65); SL, Sierra Leone Rise (73); MM, Madagascar/Marion (84); BR, Broken Ridge (95); WA, Wallaby Plateau (96); CK, central Kerguelen (100); SK, south Kerguelen (114); RT, Rajhmahal Traps (118); MR, Maud Rise (125); PE, Parana-Etendeka (132); BU, Bunbury Basalts (132); KR, Karroo Basalts (182); CP, Central Atlantic Magmatic Province (200); and SC, Skagerrak Centered LIP (297). See *Torsvik et al.* [2006, 2008] for details. There is a strong tendency for LIP eruption sites to overlie the margin of the Africa low-velocity region near the −1% slow contour (thick red line).

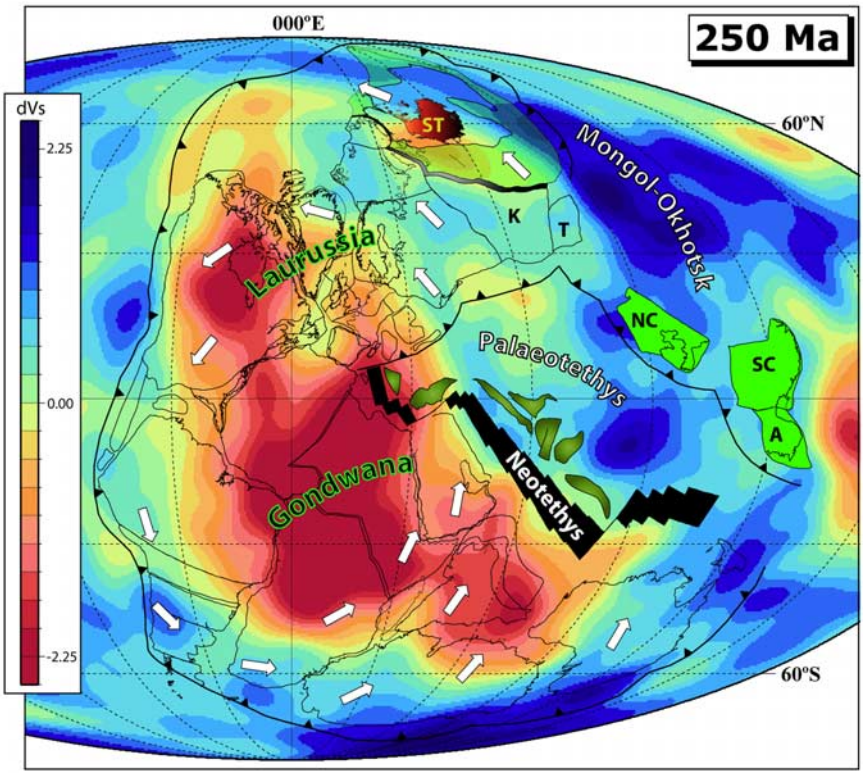

Figure 19. The 250 Ma reconstruction (hybrid model, Table 6) in which the continental outlines are superposed on shear wave velocity anomalies (as in Figure 18) near the core-mantle boundary, assuming that these heterogeneities have remained more or less in the same place for the last 300 Ma [*Burke and Torsvik*, 2004; *Torsvik et al.*, 2006, 2008]. Large white arrows show a generalized velocity vortex, averaged between 245 and 255 Ma, in which Pangea is seen rotating counterclockwise around a pole near the equator in NW Africa. At this time the Neo-Tethys had opened (black areas), and many former peri-Gondwana terranes had separated from the Gondwana margin (e.g., Apulia, the Taurides, the Middle Eastern Terranes, and the Tibetan Qiangtang Terrane). Paleo-Tethyan oceanic lithosphere is being subducted beneath Eurasia, whereas Mongol-Okhotsk oceanic lithosphere is subducting underneath Siberia. We show the Kazakh (K) and Tarim (T) terranes as part of Pangea, whereas Indochina (A), north China (NC) (mean pole 50.4°N, 358.1°E; N = 12 poles; and A_{95} = 5.4°), and south China (SC) (mean pole 50.3°N, 226.7°E; N = 28 poles; and A_{95} = 4.8°) (calculated from data referenced by *Torsvik and Cocks* [2004]) are located in subtropical to equatorial latitudes in the eastern Paleo-Tethys. The Siberian Traps are labeled ST in Siberia, but at 250 Ma Siberia was probably not yet fully attached to Baltica and Kazakhstan (see the gaps between Siberia and Kazakh).

by prescribing the global plate subduction history as a surface boundary condition. An accurate absolute plate motion model in a mantle reference system would result in an accumulation of subducted slab material in the mantle through geological time that is in agreement with global seismic tomography images. An absolute reference frame in agreement with subducted slabs may be termed a "subduction absolute reference frame." Such a reference system, based on using subducted slab locations from seismic tomography as an additional plate kinematic model constraint, could be the next step toward developing a unified plate motion/mantle convection model through time. A unified geodynamic/plate tectonic modeling approach would enable the mapping of mantle-driven surface topography (*dynamic topography*) in space and time and ultimately provide fundamental insights into the driving forces of plate tectonics.

GLOSSARY

Apparent polar wander (APW): Apparent motion of the Earth's spin axis (pole) relative to a plate. It represents a convenient way of summarizing paleomagnetic data for a continent instead of producing paleogeographic maps at each geological period. The three most common methods for generating APW paths are running mean, spherical splines, and the small circle method.

Avalonia: Paleozoic terrane that included the eastern North America seaboard from Newfoundland to as far south as Cape Cod, Massachusetts. In Europe it included southern Ireland, Wales, England, Belgium, the Netherlands, and parts of northern Germany. It rifted off the NW margin of

Gondwana in the Early Ordovician and collided with Baltica in Late Ordovician times.

Baltica: Old cratonic terrane that occupied much of northern Europe (including most of Scandinavia) eastward to the Urals. It was an independent terrane in the early Paleozoic and collided with Avalonia in the Late Ordovician and subsequently with Laurentia during Silurian times (i.e., the Caledonian orogeny).

Breakup: Final separation along a preexistent line of weakness between two (or three) tectonic plates due to horizontal extensional forces and/or mantle vertical impingement. If this process is successful, it will lead to sea floor spreading.

Cenozoic: Most recent of the three classic Phanerozoic geological eras (circa 65 Ma to recent) and divided into two periods (Paleogene and Neogene). Most of the Cenozoic (until ~1.8 Ma) is also known as Tertiary.

Cimmeria: Continental elements found today in Turkey, Iran, Afghanistan, Tibet, and Indochina, which drifted northward from Gondwana's northern margin toward Eurasia in the early Mesozoic.

Continent-ocean boundary (COB): Boundary between continental (often variably stretched) and oceanic crust and most commonly established from gravity gradients, magnetic anomaly patterns, and seismic studies. In reality, the boundary is better described as a continent-ocean transition zone between true continental and true oceanic crust, usually some tens of kilometers wide. Establishing the location of the COB is critical to plate reconstruction–derived estimates of predrift extension.

Core-mantle boundary: Boundary between the Earth's solid silicate mantle and liquid iron-nickel outer core at approximately 2900 km depth. The boundary is observed as a first-order discontinuity in seismic wave velocities.

Dynamic topography: Topography due to density anomalies in the Earth mantle and the slow solid-state convective flow driven by those density anomalies. On a large scale (wavelengths longer than about 1000 km) it is approximately equal to residual topography, defined as actual topography minus isostatic topography (derived from a model of crustal and lithospheric layer thicknesses and densities) minus thermal topography (based on a model of ocean floor ages and an age-depth relationship). Residual topography is considerably uncertain because of errors in both isostatic and thermal topography.

Euler pole: Point on a sphere (defined by geographical coordinates, latitude, and longitude) that is associated (as "pivot") with the relative motion between two tectonic plates or the absolute motion of a plate in a specified reference frame. If an angle is also defined, then the Euler pole is called Euler rotation and uniquely describes the relative motion between two tectonic plates or the absolute motion of a plate for a certain time period. If only one time is specified, it means the rotation of the plate back from its present position to the position at that time. For an interval between two times (usually both in the past) the Euler pole/rotation is also referred to as stage pole/rotation.

Eurasia: One of the Earth's largest tectonic plates. It includes Europe and most of Asia and was established as a separate plate after the opening of the North Atlantic in the early Cenozoic.

Fixed hot spot frame: Reference frame for absolute plate motions. These are calculated based on geometry and ages of hot spot tracks assuming hot spots are fixed.

Geocentric axial dipole (GAD): Magnetic (dipole) axis, today inclined from the geographic (rotation) axis by approximately 11.5°. The magnetic axis, however, is slowly gyrating/wobbling around the geographic axis (known as secular variation), and over a period of a few thousand years it is hypothesized that the averaged magnetic poles correspond reasonably with the geographic poles. This is known as the GAD hypothesis, and we can therefore imagine that a magnetic dipole is placed at the center of the Earth and aligned with the Earth's rotation axis. Nondipole (quadrupole, octupole, etc.) fields may exist at a given time as short-lived higher-order complexities of the field but are assumed to average to zero over the long term in the GAD hypothesis.

Global paleomagnetic path: Apparent polar wander paths from many continents rotated through plate motion chains to one common reference plate and combined into a global paleomagnetic path.

Gondwana: Early Paleozoic vast superterrane that formed at circa 550 Ma stretching from the South Pole to the equator and beyond and including most of South America, Africa, Madagascar, India, Arabia, East Antarctica, and Australia. It collided with Laurussia to form Pangea near the end of the Carboniferous (circa 320 Ma).

Hot spots: Volcanic provinces other than those of plate boundary zones and those formed by pressure relief melting in intracontinental rifts. They are widely believed to be caused by mantle plumes.

Hot spot tracks: Chains of (largely extinct) volcanoes related to hot spots, believed to be caused as a plate moves over a mantle plume. Characteristic features include (1) age of volcanic rocks increasing from one end to the other, (2) active volcanism at a hot spot on the young end, (3) the manifestation of a large igneous province at the old end, and (4) topographic elevation. Not all these features may be present or recognizable.

Hybrid reference frame: Reference frame for absolute plate motions that is a combination of different reference frames for different time periods. In particular, the hybrid reference frame developed here is based on a moving hot spot reference frame for the past 100 Ma, for which hot spot tracks exist, and before that, a reference frame derived from the African apparent polar wander path, making the assumptions that the pole is fixed, and Africa has not moved in longitude.

Isochrons: Lines of constant age on the ocean floor. They are usually determined from oceanic magnetic anomalies and fracture zones, which form from transform faults connecting spreading segments on mid-oceanic ridges.

Large igneous provinces (LIPs): Surface expressions of catastrophically rapid dissipation of large quantities of

internal heat. They are overwhelmingly of basaltic affinity representing partial melting of the mantle at shallow depths, but whether any of the heat or material involved in the generation of LIP rocks comes from the deep mantle via mantle plumes has remained controversial.

Large low-shear-velocity provinces (LLSVP): Two large regions at the base of the deep mantle (approximately 2800 km) with shear wave velocities approximately 1% to several percent lower than average. They are recognized as the most prominent features of all global shear wave tomographic models. The well-defined African and Pacific LLSVPs are almost antipodal (180° apart) and are isolated within the faster parts of the deep mantle (subduction graveyards).

Laurentia: Terrane that included most of North America and, in Europe, Greenland, Bear Island, parts of Svalbard, northwestern Ireland, and Scotland. It was an independent entity in the early Paleozoic and collided with Avalonia-Baltica during the Caledonian orogeny to form the much larger terrane of Laurussia.

Laurussia: Superterrane that formed by the Caledonian (Silurian) collision of Laurentia, Baltica, Avalonia, and intervening terranes. It subsequently collided with Gondwana to form Pangea at the end of the Carboniferous and with Siberia and Kazakhstan blocks in the Permian.

Mantle plumes: Narrow upwellings that originate at the core-mantle boundary. Many hot spots, e.g., Hawaii in the Pacific, have long been suggested to overlie mantle plumes. Some lie at the ends of hot spot tracks that are linked to large igneous provinces.

Mesozoic: Geological time interval (era) from 250 to 65 Ma between the Paleozoic and Cenozoic. It is divided into three periods (Triassic, Jurassic, and Cretaceous).

Moving hot spot or mantle reference frame: Another reference frame for absolute plate motions. They are calculated on the basis of geometry and ages of hot spot tracks, but instead of assuming fixed hot spots, motion of hot spots in the mantle, e.g., computed with a geodynamic model, is taken into account.

Octupole: One of several possible contributions to the total magnetic field. Other contributions may be quadrupolar (i.e., having four poles) or dipolar (with two poles), which is the presumed dominant contribution and the only one considered in the geocentric axial dipole hypothesis. Magnetic monopoles do not exist. If a zonal octupole field is present throughout the acquisition of a rock's magnetization, the inclination of that rock's magnetic record deviates from that acquired in a pure dipole field and may lead to erroneous paleolatitude calculations.

Paleolatitude: Latitude where a rock formed, computed from the inclination of its magnetization. According to the geocentric axial dipole hypothesis it corresponds to the geographic latitude of the site at the time the rock formed.

Paleomagnetic Euler pole method: Movements of continents, APW paths, and hot spot tracks describing small circle paths if the Euler pole is kept constant. It is a reasonable assumption that continents may drift around constant Euler poles for some tens of millions of years, and one can therefore fit segments along an APW path with small circles.

Paleomagnetic pole: Pole calculated from declination, inclination, and the geographic site location of the rock sample. A time average will correspond with the geographic North or South poles according to the geocentric axial dipole hypothesis.

Paleomagnetism: Study of the Earth's magnetic field preserved in rocks.

Paleozoic: First of the three classic Phanerozoic geological eras (circa 545–250 Ma), which is divided into six periods (Cambrian, Ordovician, Silurian, Devonian, Carboniferous, and Permian).

Pangea: Supercontinent (''all land'') formed near the end of the Paleozoic, from Late Carboniferous (320 Ma) times onward, by merging of Laurussia and Gondwana, joined subsequently by Kazakhstania and Siberia in turn.

Panthalassa: Ocean surrounding Pangea.

Plate motion chains: Global connection between relative plate motions. Since each tectonic plate is moving relative to its neighboring plates, vectors of motion can be combined with and transferred to the adjacent plate along a plate motion chain; the chain can be closed to become a ''circuit.'' Plate circuit closure is the requirement that the combined relative motion around a circuit is zero.

Predrift extension: Extension of the continents prior to the onset of sea floor spreading, i.e., the formation of ocean floor, between them as they move apart.

***Q* factor:** An (imperfect) measure of the reliability of a paleomagnetic result, determined by the number (out of a total of seven) of criteria that are met.

Relative and absolute plate motions: Movement of tectonic plates on a sphere relative to each other and to the mantle underneath. If a rotation is defined relative to another tectonic plate (i.e., ''keeping'' one plate fixed), then this motion/rotation is called relative to plate X. If the rotation is calculated relative to the mantle (or hot spot) or spin axis, then this is defined as an ''absolute'' motion.

Ridge push forces: Forces acting on a plate because of its higher elevation along a spreading ridge, similar to the downhill force acting on a body on an inclined plane.

Siberia: Terrane that occupied a very substantial area in the center of today's political Siberia and also adjacent areas of Mongolia, eastern Kazakhstan, and northwestern China. For all of the Paleozoic, Siberia was inverted relative to its present-day orientation. Today's northwestern margin of Siberia collided with Kazakhstania and intervening island arcs during the Permo-Carboniferous, but the terrane was not finally accreted to Laurussia to become part of Pangea until the early Mesozoic.

Slab/subducted slab/subducting slab: Part of a plate that has sunk into the mantle beneath another plate because of convergence.

Stage pole: Euler pole for a rotation in the interval between two times A and B. If both A and B are in the past, it can be computed from the Euler rotations for times A and B.

Tethys: Concept composed of three different oceanic domains, called Paleo-, Meso-, and Neo-Tethys. Paleo-Tethys was located between East Gondwana to the south and northern Eurasia (Baltica, Siberia, the Kazakhstan block, and Tarim) to the north. Meso-Tethys opened up between northern Tibet (Qiangtang block) and southern Tibet (Lhasa block) in the middle Mesozoic, although the need for this name is not recognized by everyone. Neo-Tethys opened between the Cimmerian blocks (elements in Turkey, Iran, Afghanistan, Tibet, and Indochina) and East Gondwana, as an early Mesozoic ocean that widened at the expense of the shrinking Paleo-Tethys Ocean.

True polar wander (TPW): Rotation of the entire Earth with respect to the spin axis.

Westward drift: Average motion of all lithospheric plates in a westward direction. The amount of westward drift varies strongly, depending on which reference frame for absolute plate motions is chosen, between about 1 cm/a and several centimeters per year.

[61] **ACKNOWLEDGMENTS.** Analysis and diagrams were created with GMAP [*Torsvik and Smethurst*, 1999], GMT [*Wessel and Smith*, 1998], and a prototype of GPlates specifically developed for our industrial sponsor (StatoilHydro). We thank the Norwegian Research Council and NGU for financial support (176531 GPlates, A Novel Exploration Tool). We thank R. Sutherland for discussions, M. Beck for paleomagnetic Euler pole algorithms, M. A. Smethurst for valuable statistical discussions, and S. Buiter, M. Manga, and three anonymous referees for detailed comments and suggestions to improve the manuscript.

[62] The Editor responsible for this paper was Michael Manga. He thanks Norm H. Sleep, two anonymous technical reviewers, and one cross-disciplinary reviewer.

REFERENCES

Beck, M. E., Jr., and B. A. Housen (2003), Absolute velocity of North America during the Mesozoic from paleomagnetic data, *Tectonophysics*, *377*, 33–54, doi:10.1016/j.tecto.2003.08.018.

Becker, T. W. (2006), On the effect of temperature and strain-rate dependent viscosity on global mantle flow, net rotation, and plate-driving forces, *Geophys. J. Int.*, *167*, 943–957, doi:10.1111/j.1365-246X.2006.03172.x.

Becker, T. W., and L. Boschi (2002), A comparison of tomographic and geodynamic mantle models, *Geochem. Geophys. Geosyst.*, *3*(1), 1003, doi:10.1029/2001GC000168.

Becker, T. W., V. Schulte-Pelkum, D. K. Blackman, J. B. Kellogg, and R. J. O'Connell (2006), Mantle flow under the western United States from shear wave splitting, *Earth Planet. Sci. Lett.*, *247*, 235–251, doi:10.1016/j.epsl.2006.05.010.

Behn, M. D., C. P. Conrad, and P. G. Silver (2004), Detection of upper mantle flow associated with the African superplume, *Earth Planet. Sci. Lett.*, *224*, 259–274, doi:10.1016/j.epsl.2004.05.026.

Berggren, W. A., D. V. Kent, J. J. Flynn, and J. A. van Couvering (1985), Cenozoic geochronology, *Geol. Soc. Am. Bull.*, *96*, 1407–1418, doi:10.1130/0016-7606(1985)96<1407:CG>2.0.CO;2.

Bernard, A., M. Munschy, Y. Rotstein, and D. Sauter (2005), Refined spreading history at the southwest Indian Ridge for the last 96 Ma, with the aid of satellite gravity data, *Geophys. J. Int.*, *162*, 765–778, doi:10.1111/j.1365-246X.2005.02672.x.

Besse, J., and V. Courtillot (2002), Apparent and true polar wander and the geometry of the geomagnetic field over the last 200 Myr, *J. Geophys. Res.*, *107*(B11), 2300, doi:10.1029/2000JB000050.

Bowring, S. A., D. H. Erwin, Y. G. Jin, M. W. Martin, K. Davidek, and W. Wang (1998), U/Pb zircon geochronology and tempo of the end-Permian mass extinction, *Science*, *280*, 1039–1045, doi:10.1126/science.280.5366.1039.

Bryan, P., and R. G. Gordon (1990), Rotation of the Colorado Plateau: An updated analysis of paleomagnetic data, *Geophys. Res. Lett.*, *17*, 1501–1504, doi:10.1029/GL017i010p01501.

Bullard, E. C., J. E. Everett, and A. G. Smith (1965), The fit of the continents around the Atlantic, *Philos. Trans. R. Soc. London, Ser. A*, *258*, 41–51, doi:10.1098/rsta.1965.0020.

Bunge, H.-P., C. R. Hagelberg, and B. J. Travis (2003), Mantle circulation models with variational data assimilation: Inferring past mantle flow and structure from plate motion histories and seismic tomography, *Geophys. J. Int.*, *152*, 280–301, doi:10.1046/j.1365-246X.2003.01823.x.

Burke, K., and T. H. Torsvik (2004), Derivation of large igneous provinces of the past 200 million years from long-term heterogeneities in the deep mantle, *Earth Planet. Sci. Lett.*, *227*, 531–538, doi:10.1016/j.epsl.2004.09.015.

Butler, R. F. (1992), *Paleomagnetism: Magnetic Domains to Geologic Terranes*, Blackwell Sci., Oxford, U. K.

Čadek, O., and L. Fleitout (2003), Effect of lateral viscosity variations in the top 300 km on the geoid and dynamic topography, *Geophys. J. Int.*, *152*, 566–580, doi:10.1046/j.1365-246X.2003.01859.x.

Camps, P., M. Prévot, M. Daignières, and P. Machetel (2002), Comment on "Stability of the Earth with respect to the spin axis for the last 130 million years" by J. A. Tarduno and A. V. Smirnov [*Earth Planet. Sci. Lett.*, *184*(2001) 549–553], *Earth Planet. Sci. Lett.*, *198*, 529–532, doi:10.1016/S0012-821X(02)00495-8.

Cande, S. C., and D. V. Kent (1995), Revised calibration of the geomagnetic polarity timescale for the Late Cretaceous and Cenozoic, *J. Geophys. Res.*, *100*, 6093–6095, doi:10.1029/94JB03098.

Cande, S. C., and J. M. Stock (2004), Pacific-Antarctic-Australia motion and the formation of the Macquarie plate, *Geophys. J. Int.*, *157*, 399–414, doi:10.1111/j.1365-246X.2004.02224.x.

Cande, S. C., C. A. Raymond, J. M. Stock, and W. F. Haxby (1995), Geophysics of the Pitman Fracture Zone and Pacific-Antarctic plate motions during the Cenozoic, *Science*, *270*, 947–953, doi:10.1126/science.270.5238.947.

Cande, S. C., J. M. Stock, R. D. Müller, and T. Ishihara (2000), Cenozoic motion between East and West Antarctica, *Nature*, *404*, 145–150, doi:10.1038/35004501.

Chang, T. (1988), Estimating the relative rotation of two tectonic plates from boundary crossings, *J. Am. Stat. Assoc.*, *83*, 1178–1183, doi:10.2307/2290152.

Chang, T., J. M. Stock, and P. Molnar (1992), The rotation group in plate tectonics and the representation of uncertainties of plate reconstructions, *Geophys. J. Int.*, *102*, 649–661.

Cocks, L. R. M., and T. H. Torsvik (2007), Siberia, the wandering northern terrane and its changing geography through the Palaeozoic, *Earth Sci. Rev.*, *82*, 29–74, doi:10.1016/j.earscirev.2007.02.001.

Conrad, C. P., and M. Gurnis (2003), Seismic tomography, surface uplift, and the breakup of Gondwanaland: Integrating mantle convection backwards in time, *Geochem. Geophys. Geosyst.*, *4*(3), 1031, doi:10.1029/2001GC000299.

Courtillot, C., J. Besse, and H. Théveniaut (1994), North American Jurassic apparent polar wander: The answer from other continents?, *Phys. Earth Planet. Inter.*, *82*(2), 87–104, doi:10.1016/0031-9201(94)90082-5.

DeMets, C., R. Gordon, D. Argus, and S. Stein (1990), Current plate motions, *Geophys. J. Int.*, *101*, 425–478, doi:10.1111/j.1365-246X.1990.tb06579.x.

DiVenere, V., and D. V. Kent (1999), Are the Pacific and Indo-Atlantic hotspots fixed? Testing the plate circuit through Antarctica, *Earth Planet. Sci. Lett.*, *170*, 105–117, doi:10.1016/S0012-821X(99)00096-5.

Doglioni, C., D. Green, and F. Mongelli (2005), On the shallow origin of hotspots and the westward drift of the lithosphere, in *Plates, Plumes, and Paradigms*, edited by G. R. Foulger et al., *Spec. Pap. Geol. Soc. Am.*, *388*, 735–749.

Drewes, H. (1999), Geodetic datum constraints on plate tectonic and crustal deformation models (APKIM9.0), paper presented at General Assembly, Int. Union of Geod. and Geophys., Birmingham, U. K.

Duncan, R. A. (1981), Hotspots in the southern oceans—An absolute frame of reference for motion of the Gondwana continents, *Tectonophysics*, *74*, 29–42, doi:10.1016/0040-1951(81)90126-8.

Duncan, R. A., and D. A. Clague (1985), Pacific plate motion recorded by linear volcanic chains, in *The Ocean Basins and Margins*, vol.7a, *The Pacific Ocean*, edited by A. E. M. Nairn, F. G. Stehli, and S. Uyeda, pp. 89–121, Plenum, New York.

Ekstrand, E. J., and R. F. Butler (1989), Paleomagnetism of the Moenave Formation: Implications for the Mesozoic of the North American apparent polar wander path, *Geology*, *17*, 245–248, doi:10.1130/0091-7613(1989)017<0245:POTMFI>2.3.CO;2.

Fisher, R. A. (1953), Dispersion on a sphere, *Proc. R. Soc. London, Ser. A*, *217*, 295–305.

Forsyth, D., and S. Uyeda (1975), On the relative importance of the driving forces of plate motion, *Geophys. J. R. Astron. Soc.*, *43*, 163–200.

Gaina, C., D. R. Müller, J.-Y. Royer, J. M. Stock, J. L. Hardebeck, and P. Symonds (1998), The tectonic history of the Tasman Sea: A puzzle with 13 pieces, *J. Geophys. Res.*, *103*, 12,413–12,433, doi:10.1029/98JB00386.

Gaina, C., W. R. Roest, and R. D. Müller (2002), Late Cretaceous-Cenozoic deformation of northeast Asia, *Earth Planet. Sci. Lett.*, *197*, 273–286, doi:10.1016/S0012-821X(02)00499-5.

Gaina, C.. MüR. D. ller, B. Brown, and T. Ishihara (2003), Microcontinent formation around Australia, in *Evolution and Dynamics of the Australian Plate*, edited by R. R. Hills and R. D. Müller, *Spec. Pap. Geol. Soc. Am.*, *372*, 405–416.

Gaina, C., R. D. Muller, B. Brown, T. Ishihara, and S. Ivaniv (2007), Breakup and early seafloor spreading between India and Antarctica, *Geophys. J. Int.*, *170*, 151–170, doi:10.1111/j.1365-246X.2007.03450.x.

Garnero, E. J., T. Lay, and A. McNamara (2007), Implications of lower-mantle structural heterogeneity for the existence and nature of whole-mantle plumes, in *Plates, Plumes and Planetary Processes*, edited by G. R. Foulger and D. M. Jurdy, *Spec. Pap. Geol. Soc. Am.*, *430*, 79–101.

Gordon, R. G., A. Cox, and S. O'Hare (1984), Paleomagnetic Euler poles and the apparent polar wander and absolute motion of North America since the Carboniferous, *Tectonics*, *3*, 499–537, doi:10.1029/TC003i005p00499.

Gradstein, F. M., F. P. Agterberg, J. G. Ogg, J. S. Hardenbol, P. Van Veen, J. Thierry, and Z. H. Huang (1994), A Mesozoic time scale, *J. Geophys. Res.*, *99*, 24,051–24,074, doi:10.1029/94JB01889.

Hellinger, S. J. (1981), The uncertainties of finite rotations in plate tectonics, *J. Geophys. Res.*, *86*, 9312–9318, doi:10.1029/JB086iB10p09312.

Hopper, J. R., T. Dahl-Jensen, W. S. Holbrook, H. C. Larsen, D. Lizarralde, J. Korenaga, G. M. Kent, and P. B. Kelemen (2003), Structure of the SE Greenland margin from seismic reflection and refraction data: Implications for nascent spreading center subsidence and asymmetric crustal accretion during North Atlantic opening, *J. Geophys. Res.*, *108*(B5), 2269, doi:10.1029/2002JB001996.

Idnurm, M. (1985), Late Mesozoic and Cenozoic paleomagnetism of Australia-II. Implications for geomagnetism and true polar wander, *Geophys. J. R. Astron. Soc.*, *83*, 419–433, doi:10.1111/j.1365-246X.1985.tb06495.x.

Irving, E. (2004), The case for Pangea B, and the intra-Pangean megashear, in *Timescales of the Paleomagnetic Field*, *Geophys. Monogr. Ser.*, vol. 145, edited by J. E. T. Channell et al., pp. 13–27, AGU, Washington, D. C.

Irving, E., and J. K. Park (1972), Hairpins and superintervals, *Can. J. Earth Sci.*, *9*, 1318–1324.

Ismail-Zadeh, A., G. Schubert, I. Tsepelev, and A. Korotkii (2006), Three-dimensional forward and backward numerical modeling of mantle plume evolution: Effects of thermal diffusion, *J. Geophys. Res.*, *111*, B06401, doi:10.1029/2005JB003782.

Jones, D. L., R. A. Duncan, J. C. Briden, D. E. Randall, and C. MacNiocaill (2001), Age of the Batoka basalts, northern Zimbabwe, and the duration of Karoo large igneous province magmatism, *Geochem. Geophys. Geosyst.*, *2*(2), 1022, doi:10.1029/2000GC000110.

Jupp, P. E., and J. T. Kent (1987), Fitting smooth paths to spherical data, *Appl. Stat.*, *36*(1), 34–36, doi:10.2307/2347843.

Kent, D. V., and F. Gradstein (1985), A Cretaceous and Jurassic geochronology, *Geol. Soc. Am. Bull.*, *96*, 1419–1427, doi:10.1130/0016-7606(1985)96<1419:ACAJG>2.0.CO;2.

Kent, D. V., and L. Tauxe (2005), Corrected Late Triassic latitudes for continents adjacent to the North Atlantic, *Science*, *307*, 240–244, doi:10.1126/science.1105826.

Klitgord, K., and H. Schouten (1986), Plate kinematics of the central Atlantic, in *The Geology of North America*, vol. M, *The Western North Atlantic Region*, edited by P. R. Vogt and B. E. Tucholke, pp. 351–378, *Geol. Soc. of Am.*, Boulder, Colo.

Knight, K. B., S. Nomade, P. R. Renne, A. Marzoli, H. Bertrand, and N. Youbi (2004), The central Atlantic magmatic province at the Triassic-Jurassic boundary: Paleomagnetic and $^{40}Ar/^{39}Ar$ evidence from Morocco for brief, episodic volcanism, *Earth Planet. Sci. Lett.*, *228*, 143–160, doi:10.1016/j.epsl.2004.09.022.

Kodama, K. P. (1997), A successful rock magnetic technique for correcting paleomagnetic inclination shallowing: Case study of the Nacimiento Formation, New Mexico, USA, *J. Geophys. Res.*, *102*, 5193–5206, doi:10.1029/96JB03833.

Koppers, A. A. P., R. A. Duncan, and B. Steinberger (2004), Implications of a nonlinear $^{40}Ar/^{39}Ar$ age progression along the Louisville seamount trail for models of fixed and moving hot spots, *Geochem. Geophys. Geosyst.*, *5*, Q06L02, doi:10.1029/2003GC000671.

Larter, R. D., A. P. Cunningham, P. F. Barker, K. Gohl, and F. O. Nitsche (2002), Tectonic evolution of the Pacific margin of Antarctica: 1. Late Cretaceous tectonic reconstructions, *J. Geophys. Res.*, *107*(B12), 2345, doi:10.1029/2000JB000052.

Liss, D., W. H. Owens, and D. H. W. Hutton (2004), New palaeomagnetic results from the Whin Sill Complex: Evidence for a multiple intrusion event and revised virtual geomagnetic poles for the Late Carboniferous for the British Isles, *J. Geol. Soc.*, *161*, 927–938, doi:10.1144/0016-764903-156.

Marcano, M. C., R. Van der Voo, and C. Mac Niocaill (1999), True polar wander during the Permo-Triassic, *J. Geodyn.*, *28*, 75–95, doi:10.1016/S0264-3707(98)00026-X.

Marks, K. M., and A. A. Tikku (2001), Cretaceous reconstructions of East Antarctica, Africa and Madagascar, *Earth Planet. Sci. Lett.*, *186*, 479–495, doi:10.1016/S0012-821X(01)00262-X.

McElhinny, M. W., and J. Lock (1996), IAGA paleomagnetic databases with access, *Surv. Geophys.*, *17*(5), 575–591, doi:10.1007/BF01888979.

McKenzie, D. P., and R. L. Parker (1967), The North Pacific: An example of tectonics on a sphere, *Nature*, *216*, 1276–1280, doi:10.1038/2161276a0.

Meert, J. G., and E. Tamrat (2006), Paleomagnetic evidence for a stationary Marion hotspot: Additional paleomagnetic data from Madagascar, *Gondwana Res.*, *10*, 340–348, doi:10.1016/j.gr.2006.04.008.

Molnar, P., and J. M. Stock (1987), Relative motions of hotspots in the Pacific, Atlantic and Indian Oceans since Late Cretaceous time, *Nature*, *327*, 587–591, doi:10.1038/327587a0.

Morgan, W. J. (1971), Convection plumes in the lower mantle, *Nature*, *230*, 42–43, doi:10.1038/230042a0.

Morgan, W. J. (Ed.) (1981), Hotspot tracks and the opening of the Atlantic and Indian oceans, in *The Sea*, edited by C. Emiliani, pp. 443–487, Wiley-Interscience, New York.

Müller, R. D., and W. R. Roest (1992), Fracture zones in the North Atlantic from combined Geosat and Seasat data, *J. Geophys. Res.*, *97*, 3337–3350, doi:10.1029/91JB02605.

Müller, R. D., J.-Y. Royer, and L. A. Lawver (1993), Revised plate motions relative to the hotspots from combined Atlantic and Indian Ocean hotspot tracks, *Geology*, *21*, 275–278, doi:10.1130/0091-7613(1993)021<0275:RPMRTT>2.3.CO;2.

Müller, R. D., J.-Y. Royer, and L. A. Lawver (1994), Revised plate motions relative to the hotspots from combined Atlantic and Indian Ocean hotspot tracks, Reply, *Geology*, *22*, 277–278.

Müller, R. D., W. R. Roest, J.-Y. Royer, L. M. Gahagan, and J. G. Sclater (1997), Digital isochrons of the world's ocean floor, *J. Geophys. Res.*, *102*, 3211–3214, doi:10.1029/96JB01781.

Muttoni, G., D. V. Kent, E. Garzanti, P. Brack, N. Abrahamsen, and M. Gaertani (2003), Early Permian Pangea 'B' to Late Permian Pangea 'A', *Earth Planet. Sci. Lett.*, *215*, 379–394, doi:10.1016/S0012-821X(03)00452-7.

Norton, I. O. (1995), Plate motions in the North Pacific: The 43 Ma nonevent, *Tectonics*, *14*, 1080–1094, doi:10.1029/95TC01256.

Nürnberg, D., and R. D. Müller (1991), The tectonic evolution of the South Atlantic from Late Jurassic to present, *Tectonophysics*, *191*, 27–53, doi:10.1016/0040-1951(91)90231-G.

O'Connell, R. J., C. W. Gable, and B. H. Hager (1991), Toroidal-poloidal partitioning of lithospheric plate motions, in *Glacial Isostasy, Sea-Level and Mantle Rheology*, edited by R. Sabadini, pp. 535–551, Kluwer Acad., Dordrecht, Netherlands.

O'Neill, C., R. D. Müller, and B. Steinberger (2005), On the uncertainties in hot spot reconstructions and the significance of moving hot spot reference frames, *Geochem. Geophys. Geosyst.*, *6*, Q04003, doi:10.1029/2004GC000784.

Prévot, M., F. Mattern, P. Camps, and M. Daignières (2000), Evidence for a 20° tilting of the Earth's rotation axis 100 million years ago, *Earth Planet. Sci. Lett.*, *179*, 517–528, doi:10.1016/S0012-821X(00)00129-1.

Ricard, Y., C. Doglioni, and R. Sabadini (1991), Differential rotation between lithosphere and mantle: A consequence of lateral mantle viscosity variations, *J. Geophys. Res.*, *96*, 8407–8415, doi:10.1029/91JB00204.

Richards, M. A., and D. C. Engebretson (1992), Large-scale mantle convection and the history of subduction, *Nature*, *355*, 437–440, doi:10.1038/355437a0.

Riisager, J., P. Riisager, and A. K. Pedersen (2003), Paleomagnetism of large igneous provinces: Case-study from west Greenland, North Atlantic igneous province, *Earth Planet. Sci. Lett.*, *214*, 409–425, doi:10.1016/S0012-821X(03)00367-4.

Rochette, P., and D. Vandamme (2001), Pangea B: An artifact of incorrect paleomagnetic assumptions?, *Ann. Geofis.*, *44*, 649–658.

Roest, W. R., and S. P. Srivastava (1989), Sea-floor spreading in the Labrador Sea: A new reconstruction, *Geology*, *17*, 1000–1003, doi:10.1130/0091-7613(1989)017<1000:SFSITL>2.3.CO;2.

Roest, W. R., J. J. Danobeitia, J. Verhoef, and B. J. Collette (1992), Magnetic anomalies in the Canary Basin and the Mesozoic evolution of the central North Atlantic, *Mar. Geophys. Res.*, *14*, 1–24, doi:10.1007/BF01674063.

Royer, J.-Y., and T. Chang (1991), Evidence for relative motions between the Indian and Australian plates during the last 20 m.y. from plate tectonic reconstructions: Implications for the deformation of the Indo-Australian plate, *J. Geophys. Res.*, *96*, 11,779–11,802, doi:10.1029/91JB00897.

Royer, J.-Y., and N. Rollet (1997), Plate-tectonic setting of the Tasmanian region, *Aust. J. Earth Sci.*, *44*, 543–560, doi:10.1080/08120099708728336.

Royer, J.-Y., P. Patriat, H. W. Bergh, and C. R. Scotese (1988), Evolution of the Southwest Indian Ridge from the Late Cretaceous (anomaly 34) to the middle Eocene (anomaly 20), *Tectonophysics*, *155*, 235–260, doi:10.1016/0040-1951(88)90268-5.

Royer, J.-Y., R. D. Müller, L. M. Gahagan, L. A. Lawver, C. L. Mayes, D. Nürnberg, and J. G. Sclater (1992), A global isochron chart, *Tech. Rep. 117*, Univ. of Tex. Inst. for Geophys., Austin.

Sandwell, D. T., and W. H. F. Smith (1997), Marine gravity anomaly from Geosat and ERS 1 satellite altimetry, *J. Geophys. Res.*, *102*, 10,039–10,054, doi:10.1029/96JB03223.

Schettino, A., and C. R. Scotese (2005), Apparent polar wander paths for the major continents (200 Ma to the present day): A paleomagnetic reference frame for global plate tectonic reconstructions, *Geophys. J. Int.*, *163*, 727–759, doi:10.1111/j.1365-246X.2005.02638.x.

Schmidt, A. G., P. Riisager, N. Abrahamsen, J. Riisager, A. K. Pedersen, and R. Van der Voo (2005), Paleomagnetism of the Eocene Talerua Member lavas on Hareøen Island, west Greenland, *Bull. Geol. Soc. Den.*, *52*, 27–37.

Şengör, A. M. C., and B. A. Natal'in (1996), Paleotectonics of Asia: Fragments of a synthesis, in *The Tectonic Evolution of Asia*, edited by A. Yin and M. Harrison, pp. 486–640, Cambridge Univ. Press, Cambridge, U. K.

Sharp, W. D., and D. A. Clague (2006), 50-Ma initiation of Hawaiian-Emperor bend records major change in Pacific plate motion, *Science*, *313*, 1281–1284, doi:10.1126/science.1128489.

Si, J., and R. Van der Voo (2001), Too-low magnetic inclinations in central Asia: An indication of a long-term Tertiary non-dipole field?, *Terra Nova*, *13*, 471–478, doi:10.1046/j.1365-3121.2001.00383.x.

Silverman, B. W., and G. W. Waters (1984), BATH-SPLINE: An interactive spline smoothing package, report, Sch. of Math., Univ. of Bath, Bath, U. K.

Srivastava, S. P., and W. R. Roest (1989), Seafloor spreading history II–IV, in *East Coast Basin Atlas Series: Labrador Sea*, edited by J. S. Bell, map, sheets L17-2–L17-6, Atl. Geosci. Cent., Geol. Surv. Can., Dartmouth, N. S.

Stampfli, G. M., and G. D. Borel (2002), A plate tectonic model for the Paleozoic and Mesozoic constrained by dynamic plate boundaries and restored synthetic oceanic isochrons, *Earth Planet. Sci. Lett.*, *196*, 17–33, doi:10.1016/S0012-821X(01)00588-X.

Steinberger, B. (2000), Plumes in a convecting mantle: Models and observations for individual hotspots, *J. Geophys. Res.*, *105*, 11,127–11,152, doi:10.1029/1999JB900398.

Steinberger, B., and R. J. O'Connell (1997), Changes of the Earth's rotation axis owing to advection of mantle density heterogeneities, *Nature*, *387*, 169–173, doi:10.1038/387169a0.

Steinberger, B., and R. J. O'Connell (1998), Advection of plumes in mantle flow: Implications for hotspot motion, mantle viscosity and plume distribution, *Geophys. J. Int.*, *132*, 412–434, doi:10.1046/j.1365-246x.1998.00447.x.

Steinberger, B., and T. H. Torsvik (2008), Absolute plate motions and true polar wander in the absence of hotspot tracks, *Nature*, *452*, 620–623, doi:10.1038/nature06824.

Steinberger, B., R. Sutherland, and R. J. O'Connell (2004), Prediction of Emperor-Hawaii seamount locations from a revised model of global plate motion and mantle flow, *Nature*, *430*, 167–173, doi:10.1038/nature02660.

Stock, J. M., and P. Molnar (1983), Some geometrical aspects of uncertainties in combined plate reconstructions, *Geology*, *11*, 697–701, doi:10.1130/0091-7613(1983)11<697:SGAOUI>2.0.CO;2.

Sutherland, R. (1995), The Australia-Pacific boundary and Cenozoic plate motions in the SW Pacific: Some constraints from Geosat data, *Tectonics*, *14*, 819–831, doi:10.1029/95TC00930.

Szurlies, M. (2004), Magnetostratigraphy: The key to a global correlation of the classic Germanic Trias-case study Volpriehausen Formation (Middle Buntsandstein), central Germany, *Earth Planet. Sci. Lett.*, *227*, 395–410, doi:10.1016/j.epsl.2004.09.011.

Szurlies, M., G. H. Bachmann, M. Menning, N. R. Nowaczyk, and K. C. Kaeding (2003), Magnetostratigraphy and high-resolution lithostratigraphy of the Permian-Triassic boundary interval in central Germany, *Earth Planet. Sci. Lett.*, *212*, 263–278, doi:10.1016/S0012-821X(03)00288-7.

Tan, E., E. Choi, P. Thoutireddy, M. Gurnis, and M. Aivazis (2006), GeoFramework: Coupling multiple models of mantle

convection within a computational framework, *Geochem. Geophys. Geosyst.*, *7*, Q06001, doi:10.1029/2005GC001155.

Tarduno, J. A., and R. D. Cottrell (1997), Paleomagnetic evidence for motion of the Hawaiian hotspot during formation of the Emperor Seamounts, *Earth Planet. Sci. Lett.*, *153*, 171–180, doi:10.1016/S0012-821X(97)00169-6.

Tarduno, J. A., and J. Gee (1995), Large-scale motion between Pacific and Atlantic hotspots, *Nature*, *378*, 477–480, doi:10.1038/378477a0.

Tarduno, J. A., and A. V. Smirnov (2001), Stability of the Earth with respect to the spin axis for the last 130 million years, *Earth Planet. Sci. Lett.*, *184*, 549–553, doi:10.1016/S0012-821X(00)00348-4.

Tarduno, J. A., and A. V. Smirnov (2002), Response to comment on ''Stability of the Earth with respect to the spin axis for the last 130 million years'' by P. Camps, M. Prévot, M. Daignières, and P. Machetel, *Earth Planet. Sci. Lett.*, *198*, 533–539, doi:10.1016/S0012-821X(02)00496-X.

Tarduno, J. A., R. D. Cottrell, and A. V. Smirnov (2001), High geomagnetic intensity during the Mid-Cretaceous from Thellier analysis of single plagioclase crystals, *Science*, *291*, 1779–1783, doi:10.1126/science.1057519.

Tarduno, J. A., et al. (2003), The Emperor Seamounts: Southward motion of the Hawaiian hotspot plume in Earth's mantle, *Science*, *301*, 1064–1069, doi:10.1126/science.1086442.

Torsvik, T. H. (2003), The Rodinia jigsaw puzzle, *Science*, *300*, 1379–1381, doi:10.1126/science.1083469.

Torsvik, T. H., and T. B. Andersen (2002), The Taimyr fold belt, Arctic Siberia: Timing of prefold remagnetisation and regional tectonics, *Tectonophysics*, *352*, 335–348, doi:10.1016/S0040-1951(02)00274-3.

Torsvik, T. H., and L. R. M. Cocks (2004), Earth geography from 400 to 250 Ma: A palaeomagnetic, faunal and facies review, *J. Geol. Soc.*, *161*, 555–572, doi:10.1144/0016-764903-098.

Torsvik, T. H., and T. F. Redfield (2002), Relative hotspot motions versus true polar wander, *Earth Planet. Sci. Lett.*, *202*, 185–200, doi:10.1016/S0012-821X(02)00807-5.

Torsvik, T. H., and M. A. Smethurst (1999), Plate tectonic modelling: Virtual reality with GMAP, *Comput. Geosci.*, *25*, 395–402, doi:10.1016/S00983004(98)00143-5.

Torsvik, T. H., and R. Van der Voo (2002), Refining Gondwana and Pangea paleogeography: Estimates of Phanerozoic non-dipole (octupole) fields, *Geophys. J. Int.*, *151*, 771–794, doi:10.1046/j.1365-246X.2002.01799.x.

Torsvik, T. H., M. A. Smethurst, J. G. Meert, R. Van der Voo, W. S. McKerrow, B. A. Sturt, M. D. Brasier, and H. J. Walderhaug (1996), Continental break-up and collision in the Neoproterozoic and Palaeozoic—A tale of Baltica and Laurentia, *Earth Sci. Rev.*, *40*, 229–258, doi:10.1016/0012-8252(96)00008-6.

Torsvik, T. H., R. D. Tucker, L. D. Ashwal, E. A. Eide, N. A. Rakotosolofo, and M. J. de Wit (1998), Late Cretaceous magmatism in Madagascar: Palaeomagnetic evidence for a stationary Marion hotspot, *Earth Planet. Sci. Lett.*, *164*, 221–232, doi:10.1016/S0012-821X(98)00206-4.

Torsvik, T. H., J. Mosar, and E. A. Eide (2001a), Cretaceous-Tertiary geodynamics: A North Atlantic exercise, *Geophys. J. Int.*, *146*, 850–866, doi:10.1046/j.0956-540x.2001.01511.x.

Torsvik, T. H., R. Van der Voo, J. G. Meert, J. Mosar, and H. J. Walderhaug (2001b), Reconstructions of the continents around the North Atlantic at about the 60th parallel, *Earth Planet. Sci. Lett.*, *187*, 55–69, doi:10.1016/S0012-821X(01)00284-9.

Torsvik, T. H., E. A. Eide, T. F. Redfield, E. Lundin, M. A. Smethurst, and J. Ebbing (2004), South Atlantic reconstructions: A self-consistent model, *NGU Rep. 2004.024*, 100 pp., Norg. Geol. Unders., Trondheim, Norway.

Torsvik, T. H., M. A. Smethurst, K. Burke, and B. Steinberger (2006), Large igneous provinces generated from the margins of the large low-velocity provinces in the deep mantle, *Geophys. J. Int.*, *167*, 1447–1460, doi:10.1111/j.1365-246X.2006.03158.x.

Torsvik, T. H., M. A. Smethurst, K. Burke, and B. Steinberger (2008), Long-term stability in deep mantle structure: Evidence from the ca. 300 Ma Skagerrak-centered large igneous province (the SCLIP), *Earth Planet. Sci. Lett.*, *267*, 444–452.

Van der Voo, R. (1988), Paleozoic paleogeography of North America, Gondwana and intervening displaced terranes: Comparisons of paleomagnetism with paleoclimatology and biogeography, *Geol. Soc. Am. Bull.*, *100*, 311–324, doi:10.1130/0016-7606(1988)100<0311:PPONAG>2.3.CO;2.

Van der Voo, R. (1992), Jurassic paleopole controversy: Contributions from the Atlantic-bordering continents, *Geology*, *20*, 975–978, doi:10.1130/0091-7613(1992)020<0975:JPCCFT>2.3.CO;2.

Van der Voo, R. (1993), *Paleomagnetism of the Atlantic, Tethys and Iapetus Oceans*, 411 pp., Cambridge Univ. Press, Cambridge, U. K.

Van der Voo, R., and T. H. Torsvik (2001), Evidence for late Paleozoic and Mesozoic non-dipole fields provides an explanation for the Pangea reconstruction problems, *Earth Planet. Sci. Lett.*, *187*, 71–81, doi:10.1016/S0012-821X(01)00285-0.

Van der Voo, R., and T. H. Torsvik (2004), The quality of the European Permo-Triassic paleopoles and its impact on Pangaea reconstructions, in *Timescales of the Paleomagnetic Field*, *Geophys. Monogr. Ser.*, vol. 145, edited by J. E. T. Channell et al., pp. 29–42, AGU, Washington, D. C.

Van Fossen, M. C., and D. V. Kent (1990), High-latitude paleomagnetic poles from Middle Jurassic plutons and Moat volcanics in New England and the controversy regarding Jurassic apparent polar wander for North America, *J. Geophys. Res.*, *95*, 17,503–17,516, doi:10.1029/JB095iB11p17503.

Van Fossen, M. C., and D. V. Kent (1992), Paleomagnetism of 122 Ma plutons in New England and the Mid-Cretaceous paleomagnetic field in North America: True polar wander or large-scale differential mantle motion?, *J. Geophys. Res.*, *97*, 19,651–19,661, doi:10.1029/92JB01466.

Verhoef, J., W. R. Roest, R. Macnab, and J. Arkani-Hamed (1996), Magnetic anomalies of the Arctic and North Atlantic oceans and adjacent land areas, *Open File Rep. 3125A*, Geol. Surv. of Can., Calgary, Alta., Canada.

Wessel, P., and W. H. F. Smith (1998), New, improved version of generic mapping tools released, *Eos Trans. AGU*, *79*(47), 579, doi:10.1029/98EO00426.

Wessel, P., Y. Harada, and L. W. Kroenke (2006), Toward a self-consistent, high-resolution absolute plate motion model for the Pacific, *Geochem. Geophys. Geosyst.*, *7*, Q03L12, doi:10.1029/2005GC001000.

Whittaker, J., R. D. Müller, G. Leitchenkov, H. Stagg, M. Sdrolias, C. Gaina, and A. Goncharov (2007), Major Australian-Antarctic plate reorganization at Hawaiian-Emperor bend time, *Science*, *318*, 83–86, doi:10.1126/science.1143769.

Wilson, J. T. (1963), Evidence from islands on the spreading of ocean floors, *Nature*, *197*, 536–538, doi:10.1038/197536a0.

Witte, W. K., and D. V. Kent (1990), The paleomagnetism of redbeds and basalts of the Hettangian extrusive zone, Newark Basin, New Jersey, *J. Geophys. Res.*, *95*, 17,533–17,545, doi:10.1029/JB095iB11p17533.

C. Gaina, B. Steinberger, and T. H. Torsvik, Center for Geodynamics, NGU, Leiv Eirikssons vei 39, N-7491 Trondheim, Norway. (trond.torsvik@ngu.no)

R. D. Müller, School of Geosciences, University of Sydney, Building H11, Sydney, NSW 2006, Australia.

R. Van der Voo, Department of Geological Sciences, University of Michigan, Ann Arbor, MI 48109-1005, USA.